# Fully Distributed Multi-parameter Sensors Based on Acoustic Fiber Bragg Gratings

Di Hu

Dissertation submitted to the faculty of the Virginia Polytechnic Institute and State University in partial fulfillment of the requirements for the degree of

Doctor of Philosophy

in

Electrical Engineering

Anbo Wang, Chair

Qiang Li

Gary Pickrell

Ahmad Safaai-Jazi

Yizheng Zhu

March 23, 2017

Blacksburg, Virginia

Keywords: Acoustic Fiber Waveguide; Fiber Bragg Grating; Distributed Sensing; Multi-Parameter Sensing.

# Fully Distributed Multi-parameter Sensors Based on Acoustic Fiber Bragg Gratings

Di Hu

ABSTRACT

A fully distributed multi-parameter acoustic sensing technology is proposed. Current fully distributed sensing techniques are exclusively based on intrinsic scatterings in optical fibers. They demonstrate a long sensing span, but their limited applicable parameters (temperature and strain) and costly interrogation systems have imposed a limit on their application.

A novel concept of acoustic fiber Bragg grating (AFBG) is conceived with inspiration from optical fiber Bragg grating (FBG). This AFBG structure exploits periodic spatial perturbations on an elongated waveguide to sense variations in the spectrum of an acoustic wave. It offers ten times higher sensitivity than the traditional time-of-flight measurement system using acoustic pulses. A fast interrogation method is developed to avoid frequency scan, reducing both the system response time (from 3min to <1ms) and total cost.

Since acoustic wave propagates with low attenuation in a variety of solid materials (metal, silica, sapphire, etc.), AFBG can be fabricated on a number of waveguides and to sense multiple parameters. Sub-millimeter metal wire and optical fiber based AFBGs have been demonstrated experimentally for effective temperature ($25 \sim 700\,^{\circ}\mathrm{C}$) and corrosion sensing. Hollow borosilicate tube is demonstrated for simultaneous temperature ($25 \sim 200\,^{\circ}\mathrm{C}$) and pressure ($15 \sim 75$ psi) sensing using different types of acoustic modes. Furthermore, a continuous 0.6 m AFBG is employed for distributed temperature sensing up to $500\,^{\circ}\mathrm{C}$ and to accurately locate the 0.18 m long heated section.

Sensing parameters, sensitivity and range of an AFBG can be tuned to fit a specific application by selecting acoustic waveguides with different materials and/or geometries. Therefore, AFBG is a fully distributed sensing technology with tremendous potential.

# Fully Distributed Multi-parameter Sensors Based on Acoustic Fiber Bragg Gratings

Di Hu

## GENERAL AUDIENCE ABSTRACT

Fully distributed sensing techniques are part of the growing "Internet-of-Things" trend, as they improve on traditional point sensors by providing spatially distributed measurements. Current techniques for fully distributed sensing are based on fiber optics, and while these techniques are capable of measuring parameters along a lengthy sensing distance, their wider application is constrained by limited applicable parameters and costly interrogation systems.

In this research, an innovative, fully distributed, multi-parameter acoustic sensing technology based on acoustic fiber Bragg grating (AFBG) is proposed. AFBG takes advantage of the interaction between an acoustic wave and the periodic structure on the measured material, and uses the spectrum property of an acoustic wave to achieve ten times higher sensitivity than traditional time-of-flight methods. In addition, a fast interrogation method is developed to avoid frequency scan, reducing both the system response time (from 3 min. to <1 ms) and system cost (from $\$5,000$ to $< \$500$).

AFBG can be fabricated using different elongated materials (i.e. waveguides) as acoustic waves propagate along a variety of materials without extensive power loss. In this research, AFBG is deployed on a sub-millimeter metal wire and silica fiber to demonstrate effective corrosion and temperature sensing ($25 \sim 700\,^{\circ}\mathrm{C}$). In addition, hollow tubes are shown to be feasible waveguides for simultaneous temperature ($25 \sim 200\,^{\circ}\mathrm{C}$) and pressure ($15 \sim 75$ psi) sensing. Finally a long AFBG is employed for distributed temperature sensing up to $500\,^{\circ}\mathrm{C}$.

Wide applicability and low cost suggest that this sensing technology may be a viable approach for fully distributed sensing, contributing to the growing Internet-of-Things movement.

To my fiancée Miao

for your persistent and amazing support

# Acknowledgment

I am genuinely grateful to my advisor Dr. Anbo Wang for his guidance and encouragement along all my six years at Center for Photonics Technology (CPT). I've learned so much from him, not only comprehensive professional knowledge but also optimistic life attitude. I'm thankful for his offering of constant financial support and numerous interesting research topics to work on. I'm also grateful for his strong support for a life-changing internship opportunity.

I would also like to thank other committee members, Dr. Gary Pickrell, Dr. Ahmad Safaai-Jazi, Dr. Yizheng Zhu and Dr. Qiang Li for their advices and assistants improving my research. I acknowledge other professors, Dr. Yong Xu and Dr. T-C Poon for their instructions in classes which play an important role in developing my academic ability.

My sincere appreciation goes to my project managers, Dr. Cheng Ma, Dr. Bo Dong, Dr. Zhihao Yu and Dr. Haifeng Xuan. They demonstrated directly to me excellent ways to develop academic skills and conduct creative thinking, along with their tremendous help on all projects. I also would like to thank other friends at CPT for their precious help on both my research and life: Dr. Dorothy Wang, Dr. Michael Fraser, Dr. Chennan Hu, Dr. Amiya Behera, Dr. Bo Liu, Dr. Lingmei Ma, Dr. Daniel Homa, Dr. Aram Lee, Dr. Peng Lu, Dr. Yuanyuan Guo, Tyler Shillig, Li Yu, Zhipeng Tian, Scott Zhang, Alan Overby, Chengshuai Li, Shichao Chen, Shuo Yang and Jiaji He.

A special thanks goes to Dr. Marcus Aguilar and his wife Mary Katherine Aguilar, with whom I feel at home in Blacksburg even being thousands of miles away from my country.

Finally, I want to express my deepest love and gratitude to my fiancée, mom, dad and brother. Only with their constant company and support can I have so much enjoyment and overcome all the difficulties, during these school years and for the rest of my life.

# Contents

# List of Figures

# List of Tables

# Chapter 1

# Introduction

## 1.1 Motivation

Sensing technology has drawn more and more attention with the fast development of industry as all industrial processes need continuous monitoring for safe and efficient operation. The recent surge in demand for smart structures has further intensified the importance of reliable and accurate sensing techniques. Using the feedback signals from these sensors, a smart structure can be thoroughly diagnosed and corresponding executions can be confidently guided. Parameters like surrounding temperature, pressure, corrosion, etc., are of special interest due to their ubiquitous existence and influence on most physical, chemical and biological processes.

Point sensors that can measure the stimuli at a specific location have been developed and used in both industrial and academic world. They are based on various principles, depending on the type of stimuli. They have proved to be reliable in most cases, but insufficient to achieve thorough supervision for a large and complicated structure or system. Distributed

sensors are emerging as an substitute, because of their ability for full scale monitoring. For example, in applications like the maintenance of a bridge or a railroad, the temperature, strain, corrosion distribution over the entire structure is required to reliably guide the repair schedule.

In general, distributed sensing techniques can be divided into two categories: quasi-distributed and fully distributed sensing. For quasi-distributed sensing, a number of point sensors are multiplexed together to form a network at discrete locations. Because these point sensors share the same interrogation systems, they are much more cost effective compared to simply using multiple sets of point sensor systems. They also take advantage of using the same sensing principle as the point sensors which are well established. So quasi-distributed sensors have evolved from point sensors without extensive investigation on sensing principle. But the number of point sensors in a quasi-distributed network is normally limited due to the increase in complexity for multiplexing, sensor interrogation and deployment. On the other hand, a fully distributed sensor resolves the stimuli along the full length of the structure with a certain spatial resolution. Current fully distributed sensing technologies mostly utilize optical scattering phenomena including Rayleigh, Raman and Brillouin scatterings. Some of these techniques now can reach spatial resolution in the order of centimeters over 40 m sensing span [1] and some can sense up to 150 km with meter length spatial resolution [2]. Despite their excellent performance, optical distributed sensing systems suffer from two drawbacks: 1) optical scattering phenomena are only sensitive to temperature and strain. So other parameters like pressure or corrosion are hard to be resolved. 2) Their interrogation systems have high signal requirement on laser sources and demodulation electronics, which make such systems very expensive.

Unlike optical waves, acoustic waves have been overlooked for distributed sensing applications in the industry. However, compared to optical systems, components for an acoustic system

like piezoelectric elements are available almost at no cost, and megahertz bandwidth required by acoustic signals significantly reduces the requirement on demodulation electronics. More importantly, acoustic wave can easily propagate along varieties of solid materials like glass, metal, crystals, etc. with low attenuation. Such wide selection of applicable materials makes acoustic sensing suitable for a broad range of applications. By engineering the waveguide material and geometry, parameters like temperature, pressure and corrosion can be deduced from change in acoustic wave properties.

## 1.2 Scope of the research

The primary objective of this research is to develop an acoustic wave based fully distributed multi-parameter sensor. The optical fiber Bragg grating (FBG) has been confirmed to be an effective sensing structure [3] and this principle is transplanted to acoustic waves to form an acoustic fiber Bragg Grating (AFBG). By ensuring single mode operation for acoustic waves, high signal quality similar to optical FBGs can be achieved. In this research, the innovative concept of AFBG is theoretically analyzed and experimentally validated. A low cost interrogation system is constructed which can detect changes in acoustic wave velocity on both solid and hollow waveguide. Measurement of parameters such as temperature, pressure and corrosion are demonstrated. A continuous AFBG is also investigated for its distributed sensing capability.

The contents of this dissertation are organized into five chapters:

Chapter 2: This chapter provides introduction to optical FBG, distributed fiber optic sensors and current acoustic sensing techniques. The similarities between acoustic wave and optical wave are presented, laying the foundation for AFBG.

Chapter 3: This chapter theoretically analyzes the AFBG structure. Starting from acoustic waveguide theory, the AFBG concept is proposed to be an effective means for sensing. Two theoretical models are introduced to analyze AFBG properties as well as guide the experiment design. Also, fast interrogation is explained.

Chapter 4: This chapter experimentally demonstrates properties of AFBG structures. First, the fabrication method and interrogation systems are described in detail. AFBGs on different materials and with different length of lead-in waveguide are investigated. Furthermore, the feasibility of multiplex AFBGs and a long continuous AFBG are proved.

Chapter 5: This chapter applies AFBG for sensing different parameters. The measurement of temperature, pressure, corrosion are demonstrated. Temperature sensing is also demonstrated in a spatially distributed manner.

Chapter 6: This chapter concludes the current research and suggests directions for future research, leading to the completion of dissertation.

# Chapter 2

# Research background

## 2.1 Bragg Condition

Bragg diffraction was first discovered by W. H. Bragg for X-ray crystallography [4]. For two coherent waves, constructive interference happens when their effective path difference $\Delta L$ is an integer multiple of wavelength $\lambda$, i.e. $\Delta L = m\lambda$, where $m = 1, 2, ....$ With the well-known wave nature of X-ray and novel assumption that a crystal is constituted with organized layers of atoms, the condition for maximum intensity in interference is described by Bragg condition.

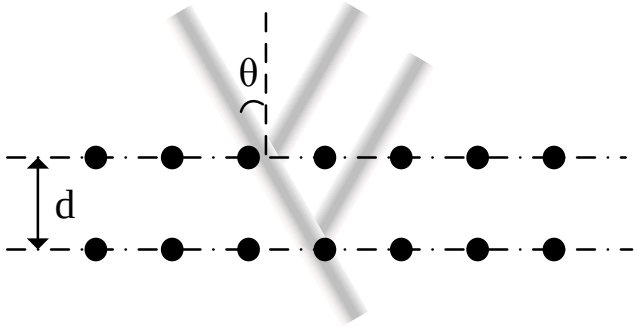


Figure 2.1: Diffraction of X-ray in a crystal

Figure 2.1 shows that the two reflected waves should interfere constructively at the Bragg condition, i.e.

$$2d\cos\theta = m\lambda \tag{2.1}$$

where $d$ is the distance between reflection planes, $\theta$ is the wave incident angle, $\lambda$ is the wavelength and $m = 1, 2, ....$ The resulting interference pattern is thus directly related to the distances between layers. So the crystal structure could be resolved from the diffraction pattern of a crystal. With this simple but very powerful relation, the existence of atomic level structure of crystals was proved.

Bragg condition has found varieties of applications since its discovery, not limited to X-ray crystallography. Its assumptions only include wave nature and periodic structure. According to De Broglie, all kinds of matter has this wave property. So Bragg condition is applicable to all types of waves, from conventional mechanical waves to more general matter waves including acoustic waves, electromagnetic waves, electrons, neutrons, etc. For acoustic waves, Bragg diffraction has been applied to managing the auditorium design [5] as well as to study human tissues [6]. Vibration isolation and enhanced acoustic transducer performances are achieved with acoustic periodic structures [7]. Surface acoustic waves are also commonly used as filters in telecommunication systems [8]. Besides x-ray crystallography, Bragg condition

are intensely applied to other electromagnetic waves like light. Optical fiber Bragg gratings and volume holography are two prime examples. Optical fiber Bragg grating is ubiquitous in optical sensing and telecommunication systems and would be thoroughly discussed in the next section. Volume holography employs periodic structure inside bulk materials to manipulate the incident light. Due to its large interaction volume, the efficiency is much higher than surface structure based holographic elements. It has been applied to data storage [9] and display [10] applications. Crystallography accuracy and resolution is significantly increased by using electrons [11] or even neutrons [12]. The smaller wavelength of electrons/neutrons compared to X-ray are feasible to interrogate much smaller size structure, with Bragg conditions as the fundamental principle..

## 2.2 Optical fiber Bragg gratings

With its fast development for four decades, optical fiber Bragg grating (FBG) has become one of the most important and ubiquitous components in optical communication and sensing systems [13]. The refractive index of the fiber core and/or cladding is periodically modulated so the incident light is reflected by these perturbations. Multiple reflections constructively interfere when Bragg condition is matched. With the periodicity of refractive index perturbation pre-determined, only incident light with specific wavelength is effectively reflected, causing a narrow bandwidth in reflection spectrum. This narrow bandwidth property brings wide application in optical communication, fiber laser and optical fiber sensing systems. For communication system and fiber laser applications, FBGs are used as bandpass filters [14] and high quality laser reflectors [15] for wavelength selection. In sensing fields, physical parameters like temperature, strain, pressure, etc, whichever could cause refractive index change of fiber core and/or cladding, would affect the reflection spectrum, especially causing

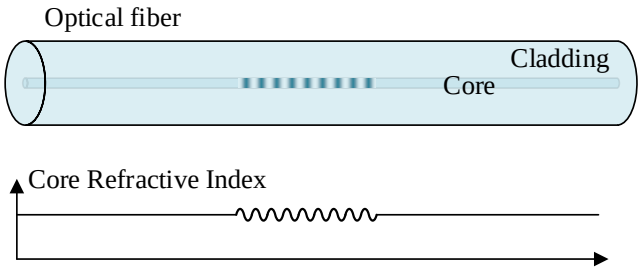


Figure 2.2: Optical fiber Bragg grating

peak wavelength shift. The narrow bandwidth of FBG therefore brings the benefit of high accuracy and resolution. Furthermore, FBG based sensing system is absolute measurement since it doesn't rely on previous data. With its rugged size and multiplexing capability, FBGs are widely used for structural health monitoring [16], inline flow measurement [17], seismology [18] and so on.

A standard FBG consists of sinusoidal perturbations in the refractive index on fiber core as shown in Figure 2.2. This perturbation is normally described as

$$\delta n_{\text{eff}}(z) = \overline{\delta n_{\text{eff}}} A(z) \left\{ 1 + \nu \cos \left[ \frac{2\pi}{\Lambda} z + \phi(z) \right] \right\} \tag{2.2}$$

where $\overline{\delta n_{\text{eff}}}$ is the DC component of the index change.$A(z)$ is the apodization function. $\nu$ is the visibility of the modulation. $\Lambda$ is the pitch length and $\phi(z)$ describes the chirp. The periodic perturbation causes the generation of a backward propagating wave. The interaction between the original forward wave $S(z)$ and the generated backward wave $R(z)$ is analyzed with coupled-mode theory to predict the spectrum of the reflected signal [19]. If we assume the self-coupling coefficient $\hat{\sigma}$ and cross-coupling coefficient $\kappa$, coupled-mode theory is stated

as

$$\begin{cases} \frac{dR(z)}{dz} = i\hat{\sigma}R(z) + i\kappa S(z) \\ \frac{dS(z)}{dz} = -i\hat{\sigma}S(z) - i\kappa^* R(z) \end{cases} \tag{2.3}$$

With the boundary conditions

$$\begin{cases} R(-\frac{L}{x}) = 1 \\ S(\frac{L}{2}) = 0 \end{cases} \tag{2.4}$$

And coupling efficiency

$$\begin{aligned} \hat{\sigma} &= 2\pi n_{\text{eff}} \left( \tfrac{1}{\lambda} - \tfrac{1}{\lambda_D} \right) + \tfrac{2\pi}{\lambda} \overline{\delta n_{\text{eff}}} - \tfrac{1}{2} \tfrac{d\phi}{dz} \\ \kappa &= \tfrac{\pi}{\lambda} \nu \overline{\delta n_{\text{eff}}} \end{aligned} \tag{2.5}$$

The power reflection coefficient is obtained

$$r = (\rho)^2 = \frac{\sinh^2 \left( \sqrt{(\kappa^2 - \hat{\sigma}^2)} L \right)}{\cosh^2 \left( \sqrt{(\kappa^2 - \hat{\sigma}^2)} L \right) - \frac{\hat{\sigma}^2}{\kappa^2}} \tag{2.6}$$

Therefore, the reflection spectrum shows a narrow peak and the peak wavelength is located at (corresponding to $\hat{\sigma} = 0$)

$$\lambda_{\max} = \left( 1 + \frac{\overline{\delta n_{\text{eff}}}}{n_{\text{eff}}} \right) \lambda_D \tag{2.7}$$

where

$$\lambda_D = 2 n_{\text{eff}} \Lambda \tag{2.8}$$

is the designed reflection peak wavelength and intuitive Bragg condition, $\Lambda$ is the pitch length of modulation, $n_{\text{eff}}$ is the effective index of optical fiber and $\overline{\delta n_{\text{eff}}}$ is the average effective refractive index change ('DC' part) of modulation. Normally, $\overline{\delta n_{\text{eff}}}/n_{\text{eff}} < 0.01$, so the intuitive Bragg condition could be applied as an approximation.

For a weak grating where the perturbation is small enough that the light interact with the whole grating without significant energy loss, the bandwidth (between two zero reflection wavelengths) is related to the number of periods $N$ by

$$\frac{\Delta\lambda}{\lambda} = \frac{v\overline{\delta n_{\text{eff}}}}{n_{\text{eff}}}\frac{2}{N} \tag{2.9}$$

with $v\overline{\delta n_{\text{eff}}}$ denotes the 'AC' part of the modulation of refractive index. It clearly demonstrates that the bandwidth is inversely proportional to the number of periods, i.e. more periods lead to narrower bandwidth. For a 1 mm long FBG, the bandwidth is typically around 1 nm [20].

There are two methods to fabricate FBGs. The conventional way is to take advantage of the interference pattern of two ultraviolet (UV) beams. These two beams are normally generated from the diffraction on phase masks [21]. Since the hydrogen-loaded germanium is sensitive to the intensity of UV light, the interference pattern of UV beams generates the corresponding refractive index modulation in fiber core. Furthermore, in Talbot scheme, the interference pattern from two UV beams can be controlled by using two mirrors to redirect the light and tuning the beam incidence angle [22]. This leads to refractive index modulation with controllable pitch lengths, so the resulting FBGs have different peak reflection wavelengths. With this improvement, wavelength multiplexing for FBG became possible, which largely broadens the applications of FBG.

In recent years, a new method was invented to fabricate FBGs in a point-by-point manner [23, 24]. In this method, an ultrafast pulse laser beam is focused by a high magnification objective. The laser peak power is so high that it directly damages the fiber material, causing refractive index change. The fiber is moved by an ultra-precise stage (precision $< 5nm$) and the pitch length between damaged points are controlled within 0.5% variance.

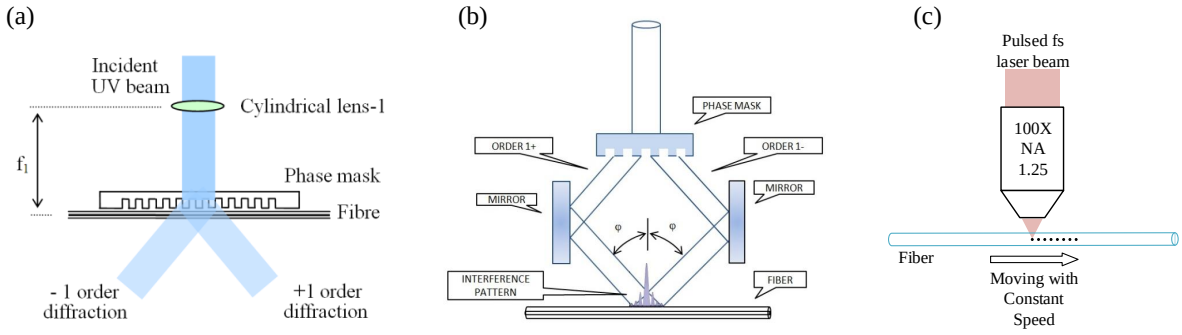


Figure 2.3: Optical fiber Bragg grating fabrication: (a) Directly from Phase mask. (b) Talbot Setup (c) Point-by-point method

This novel method has several advantages: 1) fully control of grating chirp property, which is determined by stage movement and can be tuned easily. Comparatively, the chirp property is prefixed on the phase mask in the two-beam interference method, so phase masks have to be switched to inscribe FBGs with different properties. 2) Easy through-coating fabrication. Since the fiber coating is opaque to UV light, it has to be removed during the conventional recording process. This section of bear fiber is extremely fragile and needs special care for field applications. For the point-by-point method, the laser beam is so highly focused that only within the small region ($< 10\mu m$) of focal point does the material damage. So the fiber core is damaged while the fiber coating stays untamed. 3) Working at high temperature. The refractive index modulation in hydrogen-loaded germanium would be bleached at high temperature [25]. But the physical damage via point-by-point method survives up to 1000 °C [26].

One of the advantages of FBG lies in its capability for multiplexing, which not only reduces cost per FBG unit, but also provides quasi-distributed spatial sensing capability. There are two typical multiplexing methods used for FBGs, wavelength division multiplexing (WDM) and time division multiplexing (TDM). Two methods separate signals from different FBGs and achieve low insertion loss in different ways. WDM method takes advantage of the

fact that each FBG has a very narrow reflection bandwidth. Multiple FBGs with different center wavelengths could be joined together and their reflection spectra are simultaneously measured with a interrogation system covering the whole spectrum range [27]. This method is direct and easy to implement. But there are two drawbacks: 1) all FBGs should have different reflection wavelengths so the fabrication process is complicated. 2) It is normally limted to tens of FBGs because the bandwidth for interrogation system is $< 100nm$ while the bandwidth of FBG is $\sim 1nm$. For the TDM method, identical FBGs are multiplexed with a certain distance between each other so that when a pulse is launched, the reflection signals from each FBG are delayed differently and could be separated in time with a fast switch. Up to one thousand of FBGs have been demonstrated by multiplexing this way [28]. There are also two drawbacks for TDM: 1) the spatial resolution is limited to meters due to the fast velocity of light and finite interrogation pulse duration. 2) Complex and expensive high speed devices are indispensable in the system. There are also other multiplexing methods, like combined WDM and spatial division multiplexing (SDM) [29], dense WDM with CDMA [30], etc. Even though they bring in some improvement on multiplexed FBGs performance as sensors, all of them also increase system complexity and expense.

Physical parameters like temperature and strain would affect wave propagation properties like the effective refrative index $n_{\text{eff}}$ in the optical fiber. Temperature and strain affect $n_{\text{eff}}$ through theomo-optic effect and photo-elastic effect respectively. With the relation in Eqn (2.7), these physical parameters are well monitored by the peak wavelength location of FBG reflection spectrum. The responsivity is around $1\,\text{pm}/\mu\varepsilon$ and $10\,\text{pm}/^{\circ}\text{C}$ [31]. With its miniature size, multiplexing capability and accurate response to physical parameters, FBG has been widely applied to fields like oil down-hole [32], aerospace [33], security [34], nuclear energy [35], civil structures [36], etc. However, there are a few limitations. Type I FBG works at the temperature lower than $450\,^{\circ}\text{C}$, above which the FBG is bleached and loses its

functionality. Even with the type II FBG, on which permanent damages exist, the standard telecommunication fiber cannot withstand temperature over 1000 °C for a long term due to the degradation of fiber material itself [3]. Hence, sapphire optical fiber shows up as the only choice for ultra-high temperature sensing (over 1000 °C). But the multimode nature of sapphire fiber limits its spectrum bandwidth and thus the sensing accuracy for practical applications.

## 2.3 Acoustic waves in solids and application as sensors

### 2.3.1 Introduction to acoustic waves in solids

Acoustic wave is the time-varying deformation of material media. The displacement $\mathbf{u}$ of particles about their equilibrium location is normally used to describe acoustic waves. Since particles can move in 3D space, $\mathbf{u}$ is a 3-by-1 vector. Material deformation is a measurement of relative displacement between neighboring particles and is represented by strain $\mathbf{S}$. Within linear elastic region,

$$\mathbf{S} = \nabla_s \cdot \mathbf{u} \tag{2.10}$$

where $\nabla_s$ means symmetric matrix of divergence operation. Strain causes restoration forces, i.e. stress $\mathbf{T}$, through the Hooke's Law.

$$\mathbf{T} = \mathbf{c} : \mathbf{S} \tag{2.11}$$

where $\mathbf{c}$ is the elastic stiffness matrix and double scaler (or double dot) means the product between two matrices. For solids, $\mathbf{c}$ is a 6-by-6 matrix and the symmetry of molecule structure determines the matrix structure. This relation is analogous to the constitutive relation

in electromagnetic waves $\mathbf{D} = \boldsymbol{\epsilon} \cdot \mathbf{E}$, where $\boldsymbol{\epsilon}$ is a 3-by-3 matrix. So it is obvious that the constitutive relation of acoustic waves is much more sophisticated compared to that of electromagnetic waves.

Unlike electromagnetic waves which are always transverse waves, acoustic wave can oscillate in both transverse and longitudinal directions. For a free standing plate, three different modes of acoustic waves are supported by the waveguide structure. Shear horizontal (SH) wave vibrates in the transverse direction which is parallel the plate. Lamb waves include shear vertical (SV) and longitudinal (P) wave, which are coupled together due to the fundamental reflection property of acoustic wave at stree-free boundaries. SV wave vibrates perpendicularly to both and propagation direction and to the plate. P wave vibrates along the wave propagation direction. There are some interesting scenarios under special conditions, resulting Lamé wave and Rayleigh waves. There is no coupling between SV wave and P wave for Lamé waves and the wave energy is tightly confined to the vicinity of boundaries for Rayleigh waves. For a free standing cylindrical waveguide, three types of waves are supported, torsional (T), longitudinal (L) and flexural (F). T modes only vibrate along the azimuthal direction. L modes are a combination of axial vibration and radial vibration. And in the low frequency region, radial vibration is negligible. F modes are the mixture of vibrations in all direction. The properties of these waves are of special interest to this research, so they will be explained in Chapter 3 in details.

For any isotropic solid material, its elastic properties is described by a symmetric stiffness matrix $\mathbf{c}$ with only two independent Lamé constants $\lambda(= c_{12})$ and $\mu(= c_{44})$, which relates directly to velocities of longitudinal and shear waves in the medium, respectively [37]. The wave function that governs the characteristics of propagating acoustic wave is Christoffel equation

$$\mu\nabla^2\mathbf{u} + (\lambda + \mu)\nabla(\nabla \cdot \mathbf{u}) = \rho\omega^2\mathbf{u} \tag{2.12}$$

where $\rho$ is the material density and $\omega$ is the wave angular frequency.

This equation is very similar to the governing equation derived from Maxwells equations for electromagnetic waves,

$$\nabla^2\vec{E} - \nabla(\nabla\cdot\vec{E}) = \mu\epsilon\omega^2\vec{E} \tag{2.13}$$

where $\mu$ is medium permeability and $\epsilon$ is medium permittivity. To find the solution, $\vec{E}$ is expressed by vector potential $\vec{A}$ and scaler potential $\varphi$ as

$$\vec{E} = -j\omega\vec{A} - \nabla\cdot\varphi \tag{2.14}$$

$\vec{A}$ and $\varphi$ for dielectric material without current source or free charges satisfy the Helmholtz equation

$$\begin{cases} \nabla^2\vec{A} + k^2\vec{A} = 0 \\ \nabla^2\varphi + k^2\varphi = 0 \end{cases} \tag{2.15}$$

where $k = \omega\sqrt{\mu\epsilon}$ is wave number.

With the similarities in form between Eqn. 2.12 and Eqn. 2.13, the solution of $\mathbf{u}$ is found with a similar technique. $\mathbf{u}$ is expressed in terms of a scaler potential and a vector potential,

$$\mathbf{u} = \nabla\Phi + \nabla\times\vec{\Psi} \tag{2.16}$$

These potential variables also satisfy the Helmholtz equations

$$\begin{cases} \nabla^2\vec{\Psi} + \frac{\omega^2}{V_s^2}\vec{\Psi} = 0 \\ \nabla^2\Phi + \frac{\omega^2}{V_l^2}\Phi = 0 \end{cases} \tag{2.17}$$

Where $V_s = \sqrt{\mu/\rho}$ and $V_l = \sqrt{(\lambda+2\mu)/\rho}$. Obviously, $\vec{\Psi}$ and $\Phi$ corresponds to propagation waves with velocity $V_s$ and $V_l$, respectively. According to the directional properties of gradient

and curl operation, $\Phi$ corresponds to longitudinal waves and $\vec{\Psi}$ corresponds to shear waves.

### 2.3.2 Various type of acoustic sensors

Acoustic waves devices have been investigated for over six decades [38]. Their surging demand with the development of telecommunication technologies has brought significant improvement to the field. For example, surface acoustic wave devices are widely used as high frequency filters (100 MHz$\sim$10 GHz) in tranceiver electronics [39]. Acoustic sensors are also widely applied to other situations, like biosensing in medical diagnoses [40] and temperature and pressure sensing in industrial process control [41]. Acoustic sensors are famous for their low price, integrated functionality and highly reliable characteristics. Passive and wireless acoustic sensors are also invented so that no power source is needed [42, 43].

The acoustic wave mode employed by most acoustic wave sensors falls into two categories: the bulk acoustic wave (BAW) and the surface acoustic wave (SAW). The former mode travels inside the material and the later mode travels in the region close to the surface of material. For the BAW devices, there are two sub-categories, plate waveguide based and cylinder waveguide based. The commonly used plate waveguide based BAW devices utilize thickness shear mode (TSM) or shear-horizontal (SH) acoustic plate mode (APM) while the cylinder waveguide based BAW devices employ the torsional, longitudinal and flexural modes. For SAW devices, the most commonly employed modes are shear-horizontal modes (SH-SAW). The comparison of different types of acoustic sensors is listed in Table 2.1 [38].

Table 2.1: Comparison of acoustic sensors.

| Sensor Type | Sensitivity | Factors Determining Sensitivity | Motion at Device Surface | Operation Frequency |
|---|---|---|---|---|
| TSM | Low | Plate Thickness | Transverse | Low (5-20MHz) |
| APM | Low-Med | Plate Thickness IDT Finger Space | Transverse | Med-High (25-200MHz) |
| SAW | High | IDT Finger Space | Normal transverse | High (30-500MHz) |
| SH-SAW | Med-High | IDT Finger Space | Transverse | High (30-500MHz) |

**BAW sensors**

BAW sensors employ the acoustic waves inside the material to sense the environmental parameters. The sensors based on TSM acoustic wave are best-known for its simplicity. As illustrated in Figure 2.4 [44, 45], a AT-cut quartz is sandwiched between two metal films used as electrodes. When the electrical voltage is applied to the electrodes, an shear acoustic wave is established with the frequency inversely proportional to the thickness of the quartz substrate. The equivalent circuit of the structure is also shown in the figure. The variation of structure characteristics, like the thickness of the coated film and the substrate,causes shift of resonance frequency of the equivalent circuit, which could be used to deduce the sensing stimulus.

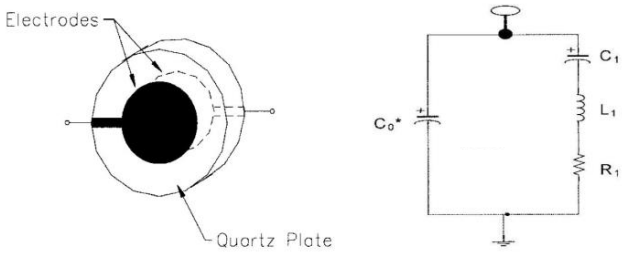


Figure 2.4: The illustrations of typical TSM based quartz resonator

The advantages of TSM based BAW sensors includes its simplicity for manufacturing, ability to withstand harsh environment and superior temperature stability due to the special cut angle of the quartz substrate. However, the relatively low sensitivity limits its application. Even though the sensitivity could be increased by reducing the substrate thickness, ultra thin substrate becomes too fragile for any field application.

Another type of plate waveguide BAW sensor bases on the SH-APM acoustic waves. A typical SH-APM sensor consists of a thin quartz substrate and two interdigital transducers (IDTs) on the same side, shown in Figure 2.5 [38]. The acoustic wave is generated by one of the IDTs and propagates through the substrate to the other IDT for detection. Even though the IDTs are on the surface of the substrate, the acoustic wave exists in the whole bulk substrate, including the other substrate surface. This brings the benefit that the IDTs can be isolated from matters for sensing. It is especially important for biomedical sensing since most of the sensing targets are in liquid which could prohibit the normal function of IDTs. Another advantage of this acoustic wave mode is the absence of wave displacement normal to the sensor surface, allowing the contacting with liquid without introducing significant loss. The SH-APM acoustic sensors have been proved to effectively detect the mercury with sensitivity 10ng/mL [46].

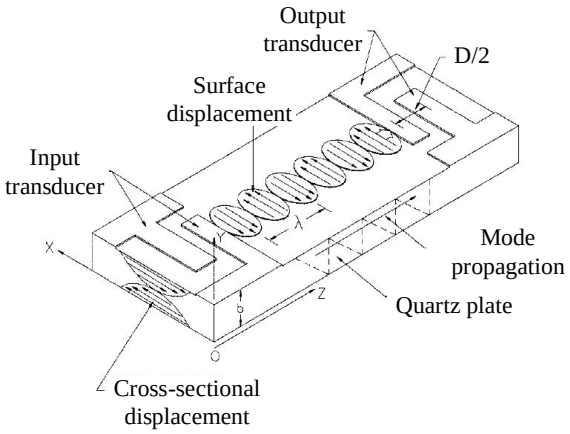


Figure 2.5: The illustrations of typical SH-APM based acoustic sensor

**SAW sensors**

SAW sensors utilize Rayleigh acoustic waves that most of their energy is confined within one wavelength depth from the surface. Rayleigh waves is composed with longitudinal vibration component and with vertical vibration component. The vertical vibration component is extremely sensitive to the mass loading and other disturbance to the surface, giving the SAW sensors highest sensitivity among all reviewed acoustic sensors [38]. A typical SAW sensor is shown in Figure 2.6 (a). With the appropriate rotation of cut angle for the substrate, the Rayleigh wave changes the vibration direction from vertical to horizontal, resulting the SH-SAW sensors, shown in Figure 2.6 (b). Because the normal vibration component of acoustic waves on a SAW sensor could lead to intensive energy dissipation if contacted with liquid, SAW are generally unsuitable for biosensing application. In contrast, the SH-SAW sensors have no normal component and are the most sensitive acoustic biosensors.

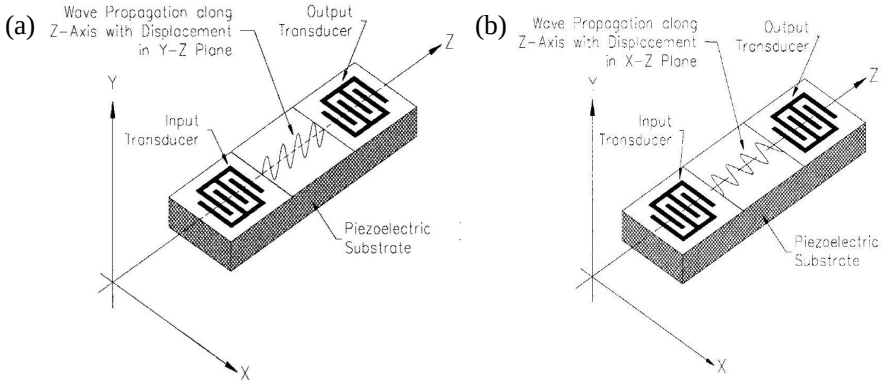


Figure 2.6: The illustrations of typical a SAW sensor (a) and a SH-SAW sensor (b)

**Elongated waveguide based sensors**

The cylindrical waveguide based BAW devices find equivalently important applications. As three types of modes, torsional, longitudinal and flexural, propagate along the waveguide, their attenuation and velocity are effected by the disturbance to the cylindrical waveguide. Therefore, the change of acoustic wave properties can be utilized to detect these disturbances, like temperature [47], strain [48], gravity [49], deposition thickness [50], density and viscosity of the fluid [51], etc. For example, a quasi-distributed temperature sensor is realized by measuring the time delay between several notches along the metal rod, as shown in Figure 2.7 [52]. The change of temperature results the local acoustic velocity variation. Thus the delay time between the notches near the temperature changed location would effectively indicate this change quantitatively.

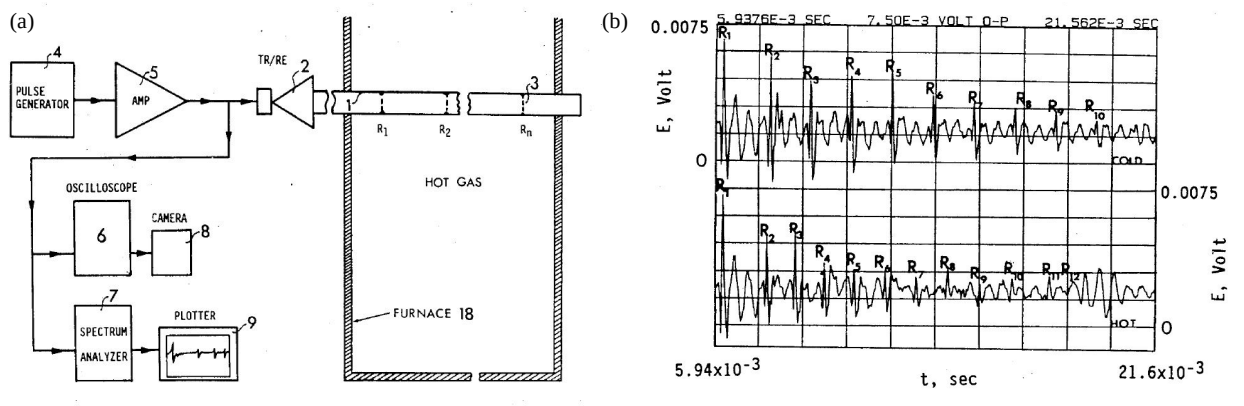


Figure 2.7: The illustrations of a quasi-distributed temperature sensor based on acoustic waves. (a) A multiple-zone sensor. (b) The comparison between the echo signals under cold and hot conditions

## 2.4 Fully distributed sensors

Distributed sensing is strongly desired by the application of structural health monitoring (SHM) for large infrastructures like a bridge, for critical vehicles like an airplane, and for energy production like oil down-hole drilling. The failure of these items could result serious damage to properties and even lives. Thanks to the intensive work conducted by the scientists and engineers in the past two decades, distributed sensors have been developed to be an reliable instrument for the measurement of temperature, strain, vibration, etc. [53].

Distributed sensors are almost exclusively optical fiber based. Optical scatterings, including Rayleigh, Raman and Brillouin scatterings are employed as the sensing mechanisms to deduce the environmental parameters. When light is launched into an optical fiber, it interacts with the traveling medium, resulting in scattering at the same frequency (Rayleigh scattering) and shifted frequencies (Raman and Brillouin scatterings), the spectrum of which are illustrated in Figure 2.8.

When a light pulse is transmitting along the fiber, the scatterings occur at each transient

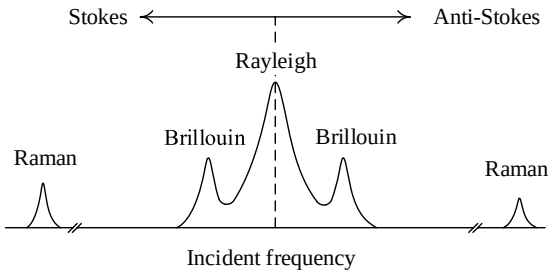


Figure 2.8: Typical scattering spectrum for Rayleigh, Brillouin and Raman scatterings

section of the optical fiber that is covered by the light pulse. As the incident light pulse travels, a continuous backscattering signal can be detected. The delay time of the backscattered signal indicates the distance between the detection point and the reflection location. In this way, fully distributed sensing could be achieved. The advantages and drawbacks of each sensor type would be addressed briefly in the following sections.

## Rayleigh scattering based distributed sensor

Rayleigh scattering is an elastic scattering phenomenon when light interacts with the material atoms. The strong electrical field of the incident light could induce a dipole structure in an atom, and then the dipole re-emit the electromagnetic wave at the same frequency as the incident light, generating elastic scattered light. The fluctuation of material density and composition causes scattering into all directions, including the backward direction. Optical time domain reflectrometry (OTDR) was the first distributed sensing technology based on Rayleigh scattering [54]. It detects the attenuation of the optical fiber and is generally employed to diagnose the compressional pressure [55, 56]. But it has very limited sensing ability. Optical frequency domain reflectometry (OFDR) is an alternative way with much higher sensitivity and spatial resolution [57, 58]. The typical OFDR sensing layout is illustrated by Figure 2.9 [1]. A laser light with sweeping frequency is launched into the

system and the Rayleigh scattering happens along the fiber under test (FUT). For each of the Rayleigh scattering point, it forms an interferometer with the reflection signal from the reference arm. The reflection spectrum of the interferometer is measured with a photo detector and a tunable laser. The reflected signal is divided into two beam by a polarizing beam splitter and detected by two photo detectors to mitigate the polarization fading effect. For each interferometer, the phase difference depends on the optical length difference between the optical length of the Rayleigh scattering point and that of the reference reflection point. Therefore, the period of the reflection spectrum for each interferometer relates to the location of the Rayleigh scattering point. By taking the Fast Fourier Transform (FFT) of the detected signal, the Rayleigh scattering reflection strength along the FUT is obtained. Any variation of the physical parameters that changes the local refractive index consequently changes the phase difference of the interferometer and can be detected with high accuracy. Due to limited laser frequency scanning range, the current spatial resolution limit is 1 cm with sensing range 40 m and temperature resolution $\sim$0.1 °C and strain resolution $\sim 1\mu\varepsilon$ [59]. It can be seen that OFDR is especially suitable for high spatial resolution (mm range) and moderate sensing distance (100 m range) applications.

## Raman scattering based distributed sensor

Raman scattering is an inelastic scattering process when the incident light or photon exchanges energy with the molecules. The energy levels between different vibration and rotation states of molecules determine the frequency shift of scattered photons. If the incident photons lose energy, the resulting scattered photons are called Stocks Raman scattering photons, otherwise, they are called anti-Stocks Raman scattering photons. Since temperature strongly influences the electron distribution in each of the molecular states, it can be measured from the Stokes and anti-Stokes Raman signals. More specifically, the ratio between

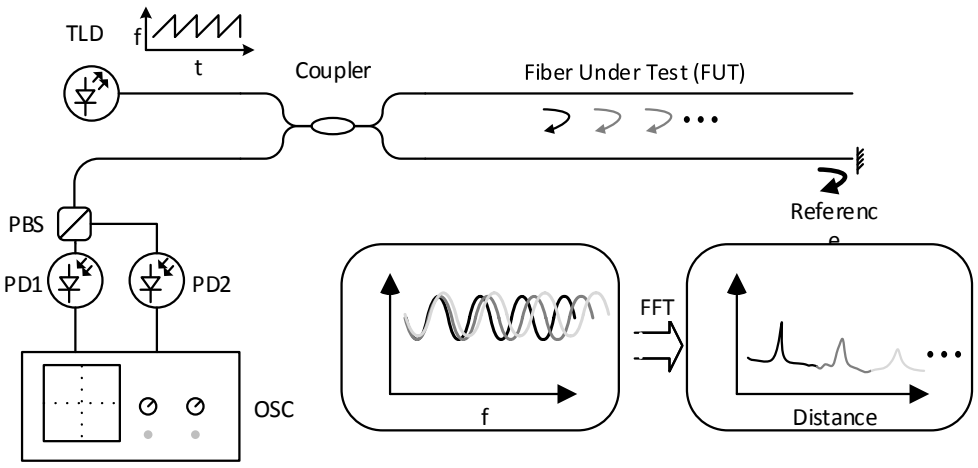


Figure 2.9: A typical OFDR sensing scheme. TLD: tunable laser diode, PBS: polarizing beamsplitter; PD1/PD2: photo detectors. OSC: oscilloscope

the two Raman scattering signals can be expressed as [60]

$$\frac{I_{AS}}{I_S} = \left(\frac{\lambda_S}{\lambda_{AS}}\right)^4 \exp\left(-\frac{\hbar\omega_M}{k_B T}\right) \tag{2.18}$$

Where $\lambda_S$ and $\lambda_{AS}$ are wavelengths for Stokes and anti-Stokes waves, respectively. $\hbar = \frac{h}{2\pi}$, $h$ is the Plank constant. $\omega_M$ is the frequency shift from the incident light. $k_B$ is the Boltzmann constant and $T$ is the temperature. An advantage of taking ratio is that the intensity fluctuation of the incident light is ruled out from the system, which significantly improves the SNR. Additionally, no other environmental parameters, like strain, pressure, humidity, etc. could introduce noises to the signal. Compared to the Rayleigh scattering based sensing principle, Raman scattering could be employed to measure the absolution temperature value rather than only the shift from a historical reference point.

A typical Raman scattering based distributed sensing system is illustrated in Figure 2.10 [60, 61]. Similar to the OTDR technology, a light pulse is launched into the system and the reflection signals along the sensing fiber is detected. The difference lies in the employment of two band pass filters (BPFs), which pass only the Stokes/anti-Stokes signals and block

all other noises, including Rayleigh scattering. The ratio between the Stokes/anti-Stokes signals is calculated and the temperature is demodulated according to Eqn(2.18).

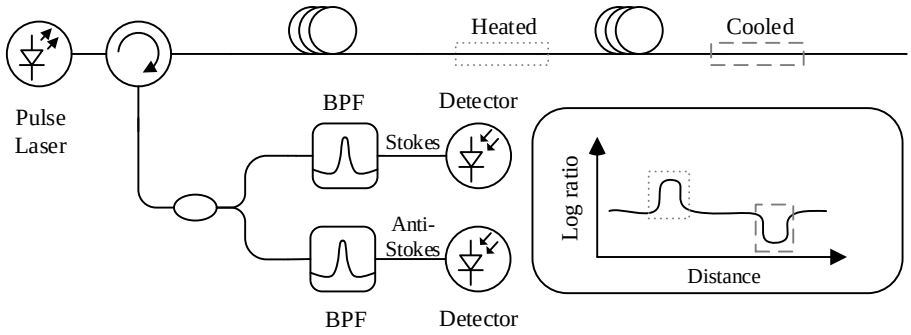


Figure 2.10: A typical optical time domain Raman scattering sensing scheme

This Raman based OTDR temperature sensing technique has been widely deployed in the oil drilling industry [62] and demonstrates a spatial resolution of $5m$ and temperature resolution of 2.5 °C with sensing span $30km$ [63]. The ultra weak anti-Stokes signal ($< 10^{-7}$) limits the system sensing span and requires significant time for signal averaging, typically several minutes. Recently, the spatial resolution has been largely improved to the order of $1cm$ with single photon-counting technique [64]. Another problem with the Raman based OTDR technique is the difference of fiber attenuation for Stokes and anti-Stokes signals. Several methods have been proposed to solve this problem, including dual end method [65], double light source method [66], and single line measurement method [67].

## Brillouin scattering based distributed sensor

The Brillouin scattering is an inelastic scattering process resulting from the interaction between the light and phonons (vibration) in the medium. The energy and momentum ex-

change follows the phase match condition and the corresponding frequency shift is called Brillouin frequency. Since the phonons normally associate with only small quantity of energy, the frequency shift of the Brillouin scattering light is in the 10GHz range, comparing to the 10THz range frequency shift for Raman scattering. The properties of the phonons are directly related to the macroscopic parameters of material like density, temperature, pressure and entropy. When any of these parameters changes, the energy and momentum of the phonon changes as well. So the energy of Brillouin scattering photons also changes accordingly. Therefore, the detection of frequency change of Brillouin scattering light can be used for the measurement of parameters like temperature and strain.

Brillouin optical time domain reflectometry (BOTDR) employs the spontaneous Brillouin scattering. But due to the weak signal intensity, the spatial resolution and sensing span are limited to 100m and 1km, respectively [68]. Brillouin optical time domain analysis (BOTDA) technology employs stimulated Brillouin scattering phenomenon [69] and much better sensing ability has been demonstrated. A typical sensing scheme is shown in Figure 2.11. A continuous laser light is launched into the system and is dividend into two arms. In the upper arm, the pump light is modulated by an EOM to generate a sideband frequency which is different from the incident light. The pump light then passes EDFAs for amplification and an optical filter so that only the frequency shifted light propagates into the FUT. In the lower arm, the probe light is modulated by another EOM to be a pulse. The probe pulse encounters the frequency-shifted pump light in FUT at the location controlled by the pulse timing. With the scanning of the frequency shift of the pump light, the depletion of the pump light reaches the maximum when the frequency shift is the same as the Brillouin frequency of the segment of fiber covered by the probe light pulse. Thus, distributed sensing along the FUT is achieved. The typical performance of a BOTDA system shows a spatial resolution of $10m$ with sensing span $22km$ and temperature resolution $1\,^{\circ}\mathrm{C}$ [70]. Brillouin optical frequency

domain analysis (BOFDA) was developed to significantly improve the spatial resolution [71], which was pushed to $3cm$ with sensing span of $9m$, showing temperature resolution of $1.8\,^{\circ}\mathrm{C}$ and strain resolution of $30\mu\varepsilon$ [72]. Additionally, Brillouin optical correlation-domain analysis (BOCDA) demonstrates a spatial resolution of $7cm$ with sensing span of $1km$ [2]. With the tremendous efforts on the Brillouin scattering in recent years, the longest sensing length is reported as $150km$ with spatial resolution of $2m$ and sensitivity of $1.5\,^{\circ}\mathrm{C}/30\mu\varepsilon$ [73].

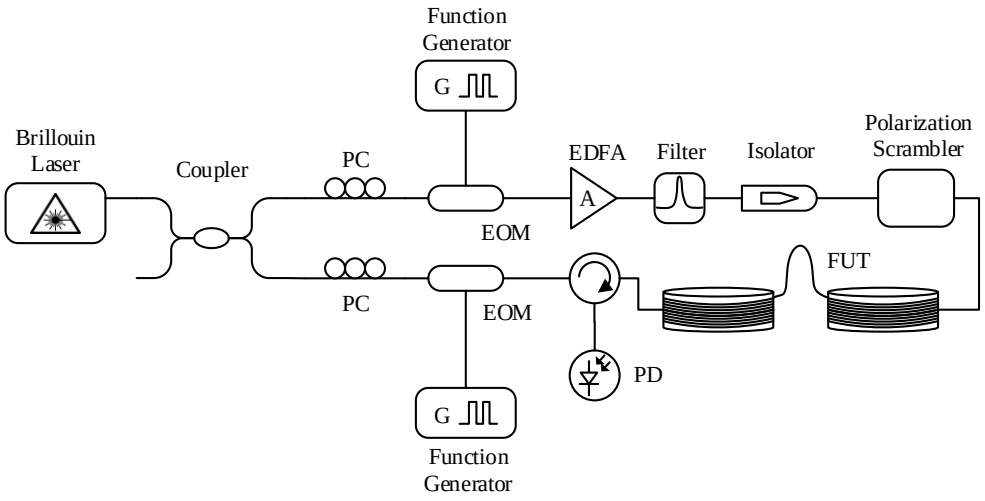


Figure 2.11: A typical optical time domain Brillouin scattering analysis (BOTDA) sensing scheme

# Chapter 3

# Acoustic fiber Bragg grating (AFBG) theories

## 3.1 Acoustic fiber waveguide

The previous chapter has demonstrated numerous applications with acoustic waveguides. These applications take advantage of the fact that guided acoustic waves has its energy highly confined along the direction of the guiding configuration, avoiding quick energy dissipation which is common for bulk acoustic waves. For cylindrical acoustic waveguide, metal wires are almost exclusively selected in all these applications due to their vast availability and their suitability for machining. Nonmetallic waveguides, like an fused silica optical fiber or even a sapphire fiber, show their advantages like highest standard of geometry and material uniformity for acoustic waves but has not been employed for really world applications. Fused silica optical fibers are low cost and free from oxidization which is a serious problem for metallic waveguides. Sapphire fibers outperform other materials with its ultra-high temperature stability and ultra-low acoustic attenuation [74]. Furthermore, waveguide with

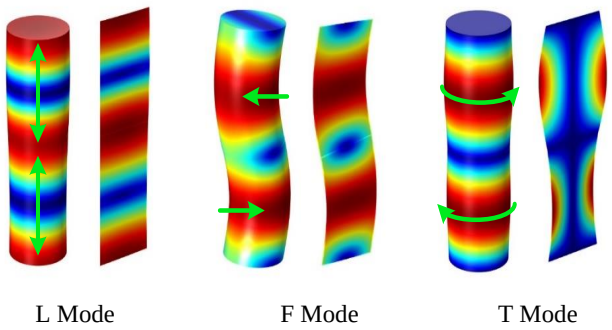


Figure 3.1: Surface and cross-sectional view of the simulated strain distribution and deformation of the three types of acoustic modes in a cylindrical rod. The movement of the fiber is indicated by green arrows

hollow structures shows very different guided acoustic wave properties and has the potential to be used for measuring pressure. Here, a detailed investigation has been conducted on acoustic waveguides with different materials and geometries.

### 3.1.1 Solid cylindrical waveguide

For convenience, the Christoffel equation that governs acoustic waves in isotropic material is repeated here from Chapter 2.

$$\mu\nabla^2\mathbf{u} + (\lambda + \mu)\nabla(\nabla \cdot \mathbf{u}) = \rho\omega^2\mathbf{u} \tag{3.1}$$

Due to its similarities to that for electromagnetic waves, the waveguide solution for acoustic waves are found using the same techniques as used for electromagnetic waves. By expanding divergence operation in cylindrical coordinates, and applying free-stress boundary conditions, characteristic equations can be obtained [75]. Three families of modes, longitudinal (L), torsional (T) and the flexural (F) modes, are obtained according to their vibration properties [76, 77, 78] and are illustrated in Figure 3.1. The L modes mainly vibrate along the cylinder axis, the T modes rotate along the axis, and the F modes are a combination vibration in the

axial, radial and rotational directions. Mathematically, each family of mode is a branch of solutions for Eqn. 3.1 with the transverse resonance principle. Transverse wave number $k_{tl}$ and $k_{ts}$, propagation constant $\beta$, angular frequency $\omega$ and acoustic velocity for longitudinal wave $V_l$ and for shear wave $V_s$ are related as

$$\begin{cases} k_{tl}^2 + \beta^2 = \left(\frac{\omega}{V_l}\right)^2 \\ k_{ts}^2 + \beta^2 = \left(\frac{\omega}{V_s}\right)^2 \end{cases} \tag{3.2}$$

With this relation, characteristic equation of T modes and L modes are simplified to Eqn.3.3 and Eqn.3.4, respectively. $J_i(x)$ is the $i$-th Bessel function of the first kind and $a$ is the cylinder radius. Due to the periodicity of Bessel functions, there are multiple solutions for $k_{ts}$ and $k_{tl}$. These corresponds to different orders of modes for each family. Characteristic equations for flexural modes are even more complicated and it is discussed in references [79].

$$k_{ts}aJ_0(k_{ts}a) = 2J_1(k_{ts}a) \tag{3.3}$$

$$\frac{2k_{tl}}{a}\left(k_{ts}^2+\beta^2\right)J_1(k_{tl}a)J_1(k_{ts}a) - \left(k_{ts}^2-\beta^2\right)^2 J_0(k_{tl}a)J_1(k_{ts}a) - 4\beta^2 k_{tl}k_{ts}J_1(k_{tl}a)J_1(k_{ts}a) = 0 \tag{3.4}$$

For each type of modes, larger transverse wave number, $k_{tl}$ or $k_{ts}$, results smaller propagation constant $\beta$, which means slower wave velocity. Therefore, the lowest order of modes has the largest velocity. Phase velocity ($v_p$) and group velocity ($v_g$) for each mode can be obtained from the dispersion relation through Eqn.3.5 [77].

$$v_p = \frac{\omega}{\beta}, v_g = \frac{d\omega}{d\beta} \tag{3.5}$$

It is worth noting that by defining the normalized parameters as $X = \beta a$ and $Y = \omega a/V_s$,

Eqn.3.3 and Eqn.3.4 could be formulated to mathematical relations involving only $X$ and $Y$. So the dispersion relations of each mode could be represented by the relation between $X$ and $Y$, and the only parameter that influences the relation is $V_s/V_l$ which corresponds to Poisson's constant $\sigma$. This transform has a significant benefit: the dispersion relation of acoustic waves on cylindrical waveguides could be represented by the same graph regardless of waveguide radius, as long as the waveguide are composed of the same material. At the same time, acoustic velocities are easily deduced from normalized parameters and Eqn.3.5 changes to

$$v_p = \frac{Y}{X} V_s, v_g = \frac{dY}{dX} V_s \tag{3.6}$$

As examples, both optical fibers and metal wires are discussed as follows.

**Optical fiber**

An optical fiber is a solid cylinder composed of three layers: core (pure silica or doped with germanium, D=9 $\sim$ 100$\mu m$), cladding (pure silica or doped with fluorine, D=125 $\sim$ 900$\mu m$) and coating (plastic). When the light travels inside the optical fiber, it is confined in the fiber core due to the refractive index difference between core and cladding and its energy flows along the fiber axis. However, this slight difference between core and cladding is negligible when it comes to acoustic waves. In order to employ the optical fiber as an effective acoustic waveguide, the coating has to be removed because of its high acoustic attenuation. Therefore, the optical fiber is simplified as a homogeneous fused silica rod. With density $\rho = 2.2\,\mathrm{g/cm^3}$, and shear velocity $V_s = 3.7\,\mathrm{km/s}$[80], dispersion relations for each acoustic mode on the SMF-28 optical fiber are solved in normalized parameters and displayed in Figure 3.2 (a). Different classes of mode are marked with different colors in the figure and the subscription numbers indicates the order of modes. This result is consistent with the published results

[81]. For the most widely used optical fiber, SMF-28 from Corning Inc., diameter $d = 125\,\mu\text{m}$ is used to calculate dispersion relation in direct physical parameters, shown in Figure 3.2 (b). It is obvious that under the cutoff frequency for $F_{12}$ mode ($\sim 17\,\text{MHz}$), only the three fundamental acoustic modes can exist on the optical fiber, $L_{01}$, $T_{01}$ and $F_{11}$. This is similar to the optical situation, even though optical wave is intrinsically a transverse wave and only one mode is allowed under a certain cutoff frequency.

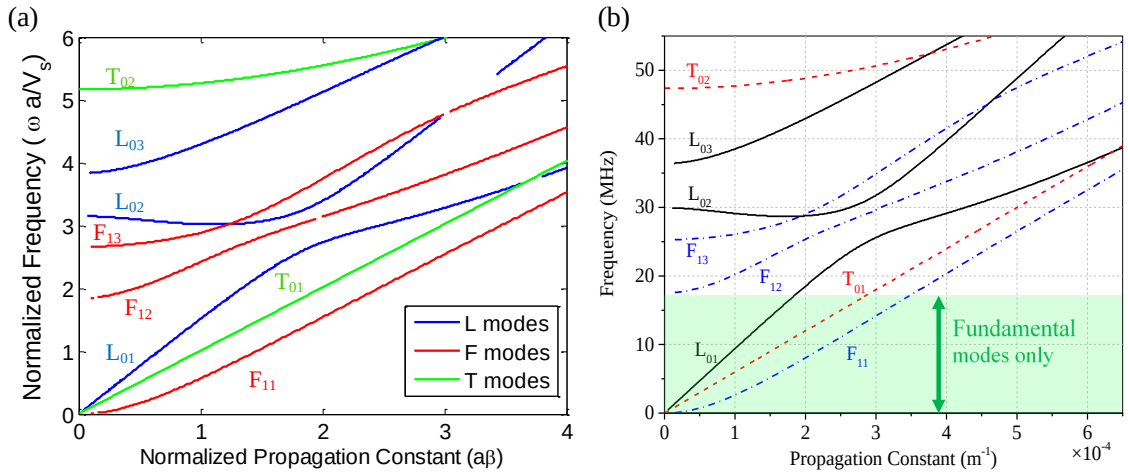


Figure 3.2: The dispersion relations for low-order acoustic modes on fused silica cylindrical waveguide (a) normalized parameters (b) with fiber diameter $125\mu m$. The green section shows only three fundamental modes exist.

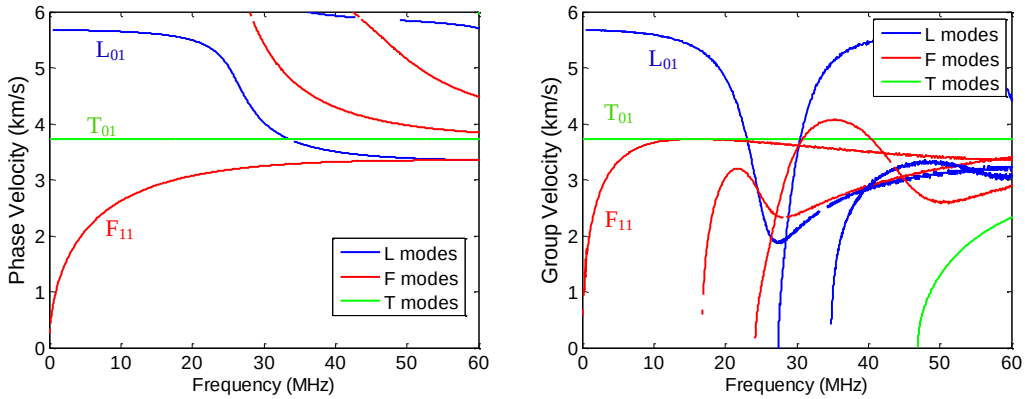


Figure 3.3: Phase velocity and group velocity of acoustic modes on Corning SMF-28.

The phase velocity and group velocity are calculated and shown in Figure 3.3. It is noticeable that in the low frequency range ($< 5\,\mathrm{MHz}$), $L_{01}$ mode has the largest group and phase velocities. $T_{01}$ is nondispersive so the velocities keeps constant over a large frequency range.$F_{11}$ mode is highly dispersive in low frequency range but becomes almost nondispersive in high frequency range. One more benefit indicated by the dispersion relation is that there is no cross point between the three fundamental modes in low frequency region, meaning no mode coupling happens among the fundamental modes during their propagation.

An experiment has been conducted to demonstrate multiple fundamental modes. Two PZTs with center frequency at 2.572MHz are used as an acoustic generator and an acoustic detector, respectively, shown in Figure 3.4 (a). An electrical pulse is generated by signal generator and is amplified to drive the PZT. Acoustic wave is coupled onto optical fiber waveguide ($0.76m$, D= $240\mu m$). The fiber end on the acoustic generation side is tilted on purpose to excite different acoustic modes. The acoustic waves propagate along the waveguide and are received by the detecting PZT. The received signals are shown in Figure 3.4 (b). By analyzing the signal with multiple reflections in consideration, two different group velocities are detected, $v_1 = 0.76m/389\mu s * 3 = 5.9km/s$, $v_2 = 0.76m/681\mu s * 3 = 3.3km/s$. Theoretical

group velocities are $v_L = 5.7km/s$, $v_T = 3.7km/s$ and $v_F = 3.3km/s$. So $v_1$ is corresponding to longitudinal wave and $v_2$ is corresponding to flexural wave. Torsional mode may not be effectively excited during this experiment.

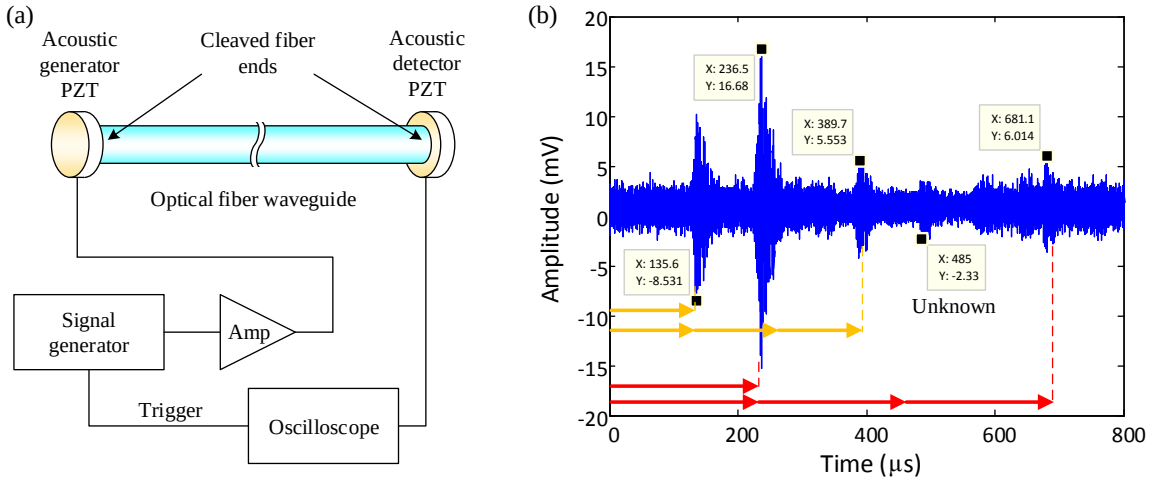


Figure 3.4: (a) Experimental setup to detect different modes of acoustic waves on an optical fiber. (b) The received signals via a 76cm long, D=240$\mu m$ optical fiber with 2.572MHz acoustic wave center frequency.

The acoustic signal with all three families of modes is not suitable for interference analysis. Fortunately, modes from each family can be selectively excited to achieve a single-mode operation. Only when the mode pattern matches with the excitation pattern, can the specific mode be dominant. This is the reason that torsional mode was not excited in the above experiment. It is also experimentally demonstrated that longitudinal mode can be selectively excited. Two PZT discs (2.4 MHz, Steiner & Martins, Inc.) are attached to both ends of a 85 cm long SMF-28 optical fiber. The PZT only vibrates perpendicular to the disc surface, matching the longitudinal mode supported by the waveguide. The received signal is proved to be purely longitudinal mode, shown in Figure 3.5 (a). The acoustic group velocity is measured to be 5.77 km/s as shown in Figure 3.5 (b). It is consistent with the theoretical

prediction from Figure 3.2 and the documented data [82]. Therefore, a specific mode can be selectively excited and maintained on the waveguide.

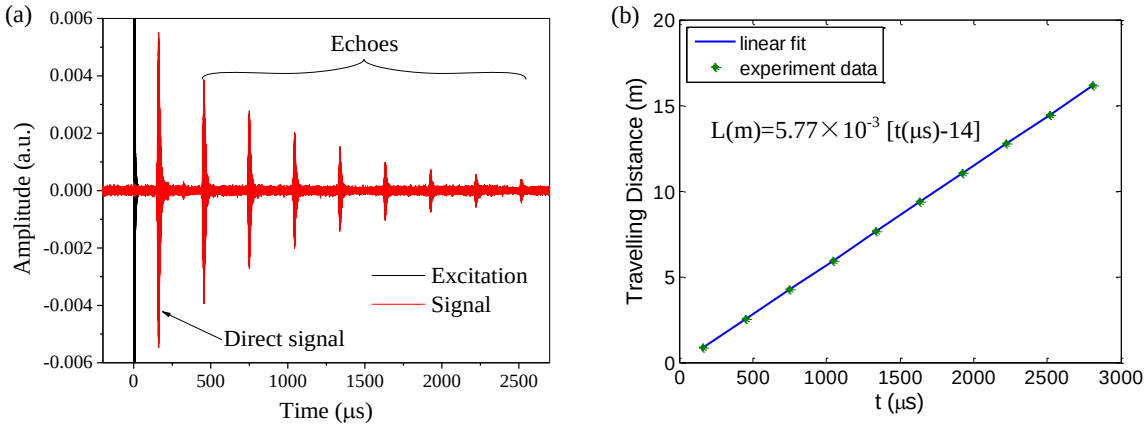


Figure 3.5: Experimental demonstration of single-mode ($L_{01}$) excitation in a $125\mu m$ diameter SMF-28 optical fiber. (a) Direct and multiple echoes from fiber end. (b) Linear fit indicates the velocity is $5.77km/s$

The acoustic attenuation on the fused silica is reported to be less than 0.01 dB/m at 1 MHz [83], and it is even much lower in crystals like sapphire [74]. Therefore, the low frequency acoustic wave (<3 MHz) based sensing span can easily stretch to tens of meters.

### Metal wire

Besides silica, many other elastic materials are capable of transmitting acoustic waves with low loss. Metal is of special interest because of it flexibility, high mechanical strength without coating, and ease for shape modification. Pelican Alloy 875 metal wire is selected for experiment due to its high melting point 1520 °C, making it feasible for high temperature applications. This alloy wire is composed of 72% iron, 22.5% chrome, and 5.5% aluminum. Instead of the transmission detection scheme used for optical fiber test, the reflection inter-

rogation scheme is used for this test. A single acoustic transducer is attached to one end of the wire and works as both transmitter and receiver. The metal wire is $2.7m$ in length and multiple bounces of acoustic waves from the end of metal wire is measured to calculate the acoustic velocity. The measurement results shown in Figure 3.6 indicate that the velocity is $5.5km/s$, which lies between the theoretical value for pure iron ($5.13km/s$), chrome ($5.94km/s$) and aluminum ($5.8km/s$).

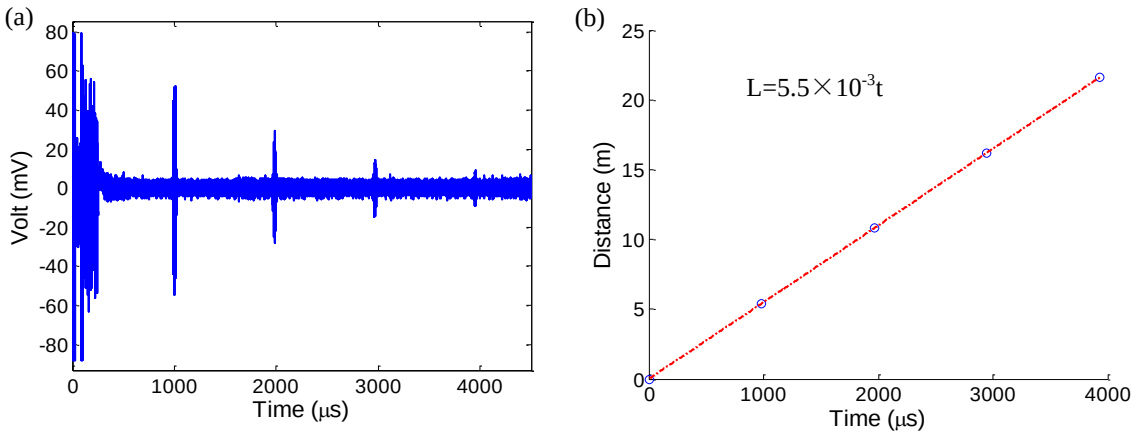


Figure 3.6: Measurement of acoustic velocity on a metal wire (OD= $0.4mm$) with reflection scheme. (a) Multiple echoes from wire end. (b) Linear fit indicates the velocity is $5.5km/s$

A bending test is also conducted on metal wire to explore any limitations to its application. The acoustic reflection from the end of wire is monitored when the middle section of wire is bent into different diameters. First, the signal is measured when wire is straight (bending diameter $> 100mm$). Then the signal is measured when bending diameter is $12mm$, $6mm$ and $4mm$, respectively. The signal intensity drops about 35% during the process, which is acceptable for sensing applications. So it is proved that even a relatively sharp bending ($4mm$) doesn't affect the functionality of metal wire based acoustic waveguide.

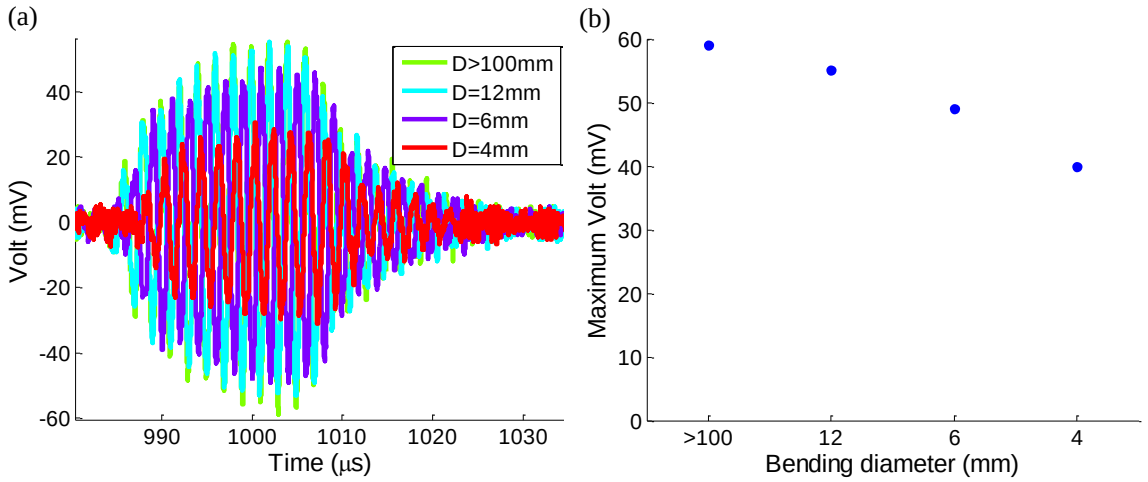


Figure 3.7: Bending test of acoustics on metal wire.

### 3.1.2 Hollow tube based waveguide

Although analytically solving Eqn. 3.1 could be very helpful to predict the acoustic wave behavior on a cylindrical waveguide as shown above, it becomes incapable when the cross section of the waveguide is more complex, like a hollow structure. Numerical simulations have emerged as a powerful substitution [84]. Finite element method (FEM), which is employed by most acoustic simulation software to solve Eqn. 3.1 , can be applied to such complex waveguide geometries. A hollow rectangular tube is analyzed with FEM as an example and the calculation results are shown in Figure 3.8.

Similar to cylinderical fiber, there are several different classes of vibration modes existing in a hollow rectangular tube. Longitudinal (L) modes vibrate along the Z axis while rotational (R) modes vibrate around the Z axis. These are similar to L and T modes on a cylindrical fiber. The F modes have two different directions for a rectangular waveguide, either along the longer side or along the shorter side of the rectangular cross section. Acoustic wave dispersion relation is calculated. A hollow fused silicate rectangular glass tube, with inner

width $a$=1 mm, inner height $b$=0.05 mm, wall thickness $t$=0.04 mm, is used as the simulation model. Four fundamental modes exist in the dispersion graph, $L_{01}$, $R_{01}$, $F_{11X}$ and $F_{11Y}$, respectively, compared to three fundamental modes shown in Figure 3.2. The phase velocity and the group velocity can also be obtained from the dispersion graph via Eqn. 3.5, with the knowledge that $L_{01}$ mode still has the largest velocities. $R_{01}$ mode is however dispersive for rectangular waveguide since the rotational symmetry vanishes. Two different F modes have slowest velocity and are highly dispersive over a large frequency range. Also, the crossing between the $R_{01}$ mode and $F_{11Y}$ mode indicates that the mode conversion could easily happen when the wave is around 80 kHz.

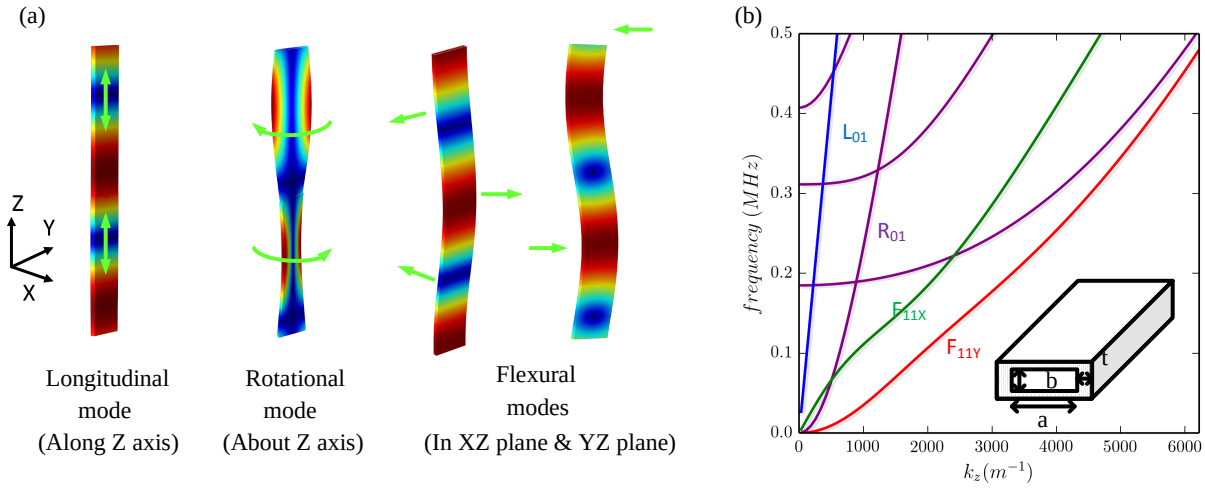


Figure 3.8: (a) Surface view of the simulated strain distribution and deformation of the three types of acoustic modes on a hollow rectangular tube. The displacement of the fiber is indicated by green arrows. (b) The dispersion relation for acoustic waves on a hollow rectangular waveguide. Inset: model geometry parameters as a=1.0mm, b=0.05mm, t=0.04mm.

## 3.2 Acoustic fiber Bragg grating

With thorough understanding of acoustic waves on waveguides, the concept of optical fiber Bragg gratings (FBGs) can now be transplanted to realize acoustic fiber Bragg gratings (AF-

BGs). Optical FBGs are one of the most fundamental components in optical communication and sensing systems as described in Chapter 2. The outstanding performance of optical FBG is due to the single mode operation condition. But under certain circumstances, the single mode condition cannot be satisfied, like sapphire fiber for high temperature applications [85]. Optical FBGs are also limited to very few materials, mainly silica. On the other hand, for an innovative AFBG, single mode operation condition can be easily satisfied on various types of fiber materials (silica, sapphire, metal, etc.). These advantages make AFBG outperform traditional optical FBGs in many applications. Even though the interaction between acoustic waves and a rod with periodic structures has been investigated by some scholars in the past few years [86, 87, 88], its Bragg grating nature has gone unnoticed.

As illustrated in Figure 3.9, when the incident wave propagates along the fiber waveguide, it is reflected at every notch. The notch is so narrow that it can be treated as a single reflection plane. The reflections at those notches interfere with each other and the net result is that only the wave with frequency satisfying the Bragg condition gets reflected. The first-order Bragg central frequency can be calculated by

$$f_B = \frac{v}{2\Lambda} \tag{3.7}$$

where $v$ is the acoustic velocity in the acoustic waveguide and $\Lambda$ is the period of the notches. Only waves with frequency in the vicinity of $f_B$ can be effectively reflected [19].

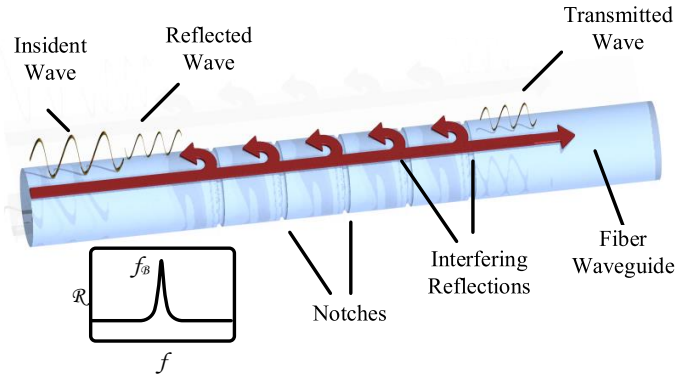


Figure 3.9: Illustration of AFBG concept. The incident wave is selectively reflected by the notches on the fiber waveguide.

## 3.3 Theoretical model for AFBG

### 3.3.1 Multi-reflection model

The most intuitive model for AFBG considers the interference between all the reflections from every reflector (notch). The reflection signal from the $i$th ($i = 1, 2...$) reflector is $s_i(t) = A_i e^{j[\omega(t-i\tau)-\beta z+\varphi_0]}$, where $A_i$ is the amplitude reflection by each reflector, $\omega$ is the wave angular frequency, $\tau$ is the time delay between neighboring notches and $\varphi_0$ describe the phase for the first reflection. With weak reflection assumption, i.e. $A_i \ll 1$, transmission loss is negligible so that $A_i = A_1$. For an AFBG with $N$ identical reflectors, the interference result is

$$S(t) = \sum_{i=1}^{N} A_i e^{j[\omega(t-i\tau)-\beta z+\varphi_0]} = A_1 \frac{1-e^{-j\omega N\tau}}{1-e^{-j\omega\tau}} e^{j(\omega t-\beta z+\varphi_0)} \tag{3.8}$$

The above formula indicates that interference only results in an amplitude modulation on the reflection signal from each notch. And when $\omega\tau = 2n\pi$, where $n = 1, 2, ...$, $S(t)$ reaches its maximum amplitude value $NA_1$. For the first order grating $n = 1$ and the relation $\tau = 2\Lambda/v$,

where $\Lambda$ is the pitch length between neighboring reflectors, the Bragg condition (Eqn.3.7) is arrived.

The spectrum of interference signal is calculated by taking Fourier transform of Eqn.3.8,

$$G(f) = A_1 e^{j(\varphi_0 - \beta z)} \frac{1 - e^{-j2\pi N f \tau}}{1 - e^{-j2\pi f \tau}} \tag{3.9}$$

With $A_1 = 1$, $|G(f)|$ is plotted in Figure 3.10 (a). The horizontal axis uses $f\tau$ so that $G(f)$ is in a normalized form. The peak wavelength location is

$$f_p = \frac{1}{\tau} = \frac{v}{2\Lambda} \tag{3.10}$$

which is the same as Bragg condition Eqn.3.7. It is obvious that larger number of reflectors leads to higher spectrum amplitude and narrower bandwidth. The peak reflection amplitude is approximated as linear relation to $N$, shown in Figure 3.10 (b). This approximation is valid when $N < 200$ and $NA_1 \ll 1$.

$$|G(f)|_{\max} = NA_1 \tag{3.11}$$

The mainlobe (ML) width, which is the frequency difference between first zero amplitude frequencies, is

$$BW_{\mathrm{ML}} = \frac{2}{N\tau} = \frac{2}{N} f_p \tag{3.12}$$

So the bandwidth is inversely proportional to $N$. The variation of acoustic velocity $v$ is linearly related to peak frequency $f_p$ so it can be measured accurately. This relation is very useful for sensing applications.

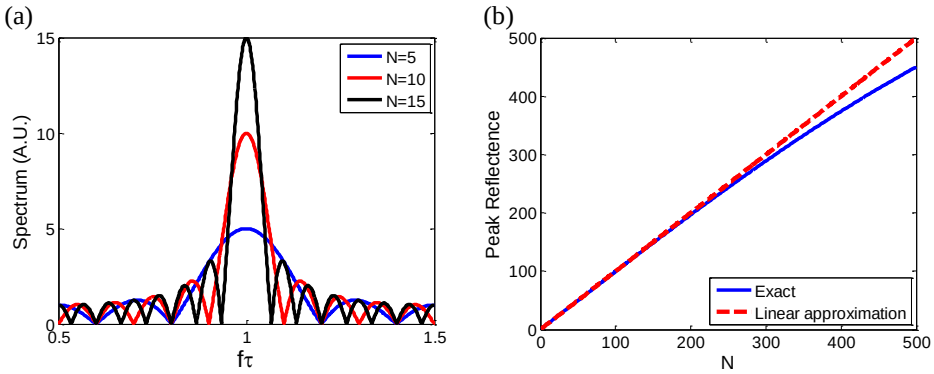


Figure 3.10: (a) The spectrum of AFBG with different number of reflectors $N$. (b) Peak reflections of spectrum with different $N$. The exact value and linear approximation are both demonstrated.

### 3.3.2 Transfer matrix model

The multi-reflection model assumes infinite narrow reflector. But in reality, the notches have a certain length and it could affect AFBG reflection properties. Transfer matrix method has been widely applied to the analysis of one-dimensional periodic structures and is supported by numerous experimental observations for the low frequency region acoustic signal [89, 90, 91, 92]. The general formula for AFBG is derived here. Furthermore, under narrow notch width condition (notch width is much less than pitch length, but has finite length), it is possible to derive analytical expressions for properties of reflection spectrum like reflection ratio, center frequency, bandwidth, phase delay, etc.

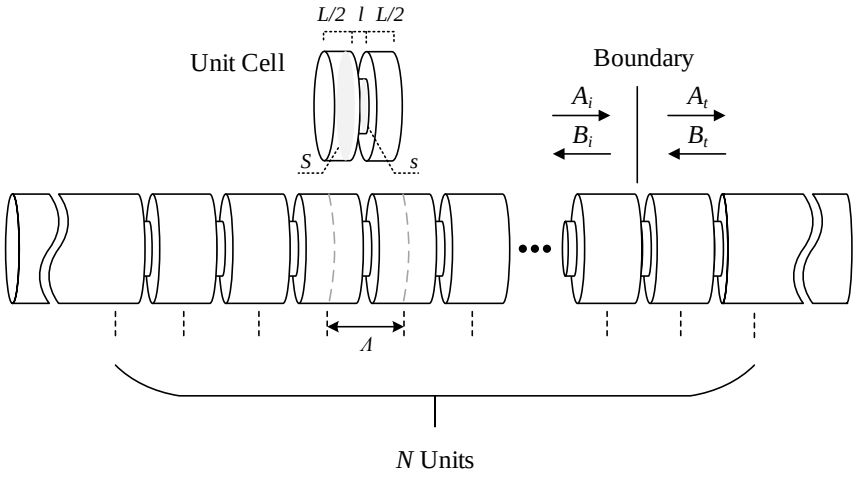


Figure 3.11: AFBG structure for transfer matrix analysis. Λ: unit cell length, $N$: number of units, $l$: notch width, $L$: length of original fiber in unit cell, $S$ and $s$: cross section area for original fiber and notch, respectively. $A_i, A_t, B_i, B_t$ stands for transmitted and reflected waves at a boundary.

An AFBG is analyzed with the following parameters: waveguide cross section area $S$, notch cross section area $s$, notch width $l$, undamaged waveguide width in each unit cell $L$, and total notches number $N$. The pitch length is thus $\Lambda = L + l$. The structure is illustrated in Figure 3.11. Following the notations in [89], the transfer matrix for a unit cell can be described as

$$T_i = P_2 D_2 P_1 D_1 P_2 \tag{3.13}$$

where $P_1$ and $P_2$ describe the wave propagation along the waveguide in the notch section and in the original fiber section, respectively. $k = 2\pi/\lambda = 2\pi f/v$ is the wave number.

$$P_1 = \frac{1}{2}\begin{bmatrix} e^{ikl} & 0 \\ 0 & e^{-ikl} \end{bmatrix}, \qquad P_2 = \frac{1}{2}\begin{bmatrix} e^{ikL/2} & 0 \\ 0 & e^{-ikL/2} \end{bmatrix} \tag{3.14}$$

$D_1$ and $D_2$ describe the wave disturbance by the notch boundaries. The relation between

transmitted and reflected waves $A_i, A_t, B_i, B_t$ could be obtained through boundary conditions, so $D_1$ and $D_2$ have the formula

$$D_1 = \frac{1}{2}\begin{bmatrix} 1+1/\gamma & 1-1/\gamma \\ 1-1/\gamma & 1+1/\gamma \end{bmatrix}, \quad D_2 = \frac{1}{2}\begin{bmatrix} 1+\gamma & 1-\gamma \\ 1-\gamma & 1+\gamma \end{bmatrix}, \tag{3.15}$$

where $\gamma = (s/S)^2$.

For the entire AFBG structure, transfer matrix can then be described as

$$M = \begin{bmatrix} M_{11} & M_{12} \\ M_{21} & M_{22} \end{bmatrix} = T_i^N \tag{3.16}$$

Since there would be no backward propagating wave beyond the end of the periodic structure, the amplitude reflection ratio $R$ for the entire periodic structure would be

$$R = -\frac{M_{21}}{M_{22}} \tag{3.17}$$

The transfer matrix for each unit cell of AFBG is assumed as

$$T_i = \begin{bmatrix} \alpha_1 & \alpha_2 \\ \alpha_3 & \alpha_4 \end{bmatrix} \tag{3.18}$$

With its expression in Eqn.3.13, each element of the matrix can be expressed by physical parameters of AFBG

$$\begin{cases} \alpha_1 = e^{ikL}[\cos(kL) + i\frac{1/\gamma+\gamma}{2}\sin(kl)] \\ \alpha_2 = i\frac{\gamma-1/\gamma}{2}\sin(kl) \\ \alpha_3 = -\alpha_2 \\ \alpha_4 = \alpha_1^* \end{cases} \tag{3.19}$$

According to properties of a $2 \times 2$ matrix, its N-th power is

$$T_i^N = \frac{\lambda_2 \lambda_1^N - \lambda_1 \lambda_2^N}{\lambda_2 - \lambda_1} I_2 + \frac{\lambda_2^N - \lambda_1^N}{\lambda_2 - \lambda_1} T_i \tag{3.20}$$

where $I_2$ is $2 \times 2$ identity matrix, and $\lambda_{1,2}$ are eigenvalues for $T_i$, i.e.

$$\lambda_{1,2} = \frac{1}{2}\left[(\alpha_1 + \alpha_4) \pm \sqrt{4\alpha_2\alpha_3 + (\alpha_1 - \alpha_4)^2}\right] \tag{3.21}$$

Substituting results from Eqn. (3.19), each item of Eqn. (3.21) becomes

$$\begin{cases} \alpha_1 + \alpha_4 = 2\cos kl \cos kL - (1/\gamma + \gamma)\sin kl \sin kL \\ \alpha_1 - \alpha_4 = 2i \cos kl \sin kL + i\,(1/\gamma + \gamma)\sin kl \cos kL \\ \alpha_2\alpha_3 = \left(\frac{\gamma - 1/\gamma}{2}\sin kl\right)^2 \end{cases} \tag{3.22}$$

With narrow pitch condition, i.e. $m = l/L < \%1$, the amplitude reflection ratio expression can be approximated as (see Appendix A for details),

$$R \approx m\pi(1+\delta)\frac{1/\gamma - \gamma}{2}\frac{\sin N\delta\pi}{\sin \delta\pi} e^{i\left\{\pi N\left[\left(\frac{1/\gamma+\gamma}{2}m+1\right)(1+\delta)-m\right]+\pi\left(\frac{1}{2}+N\right)\right\}} \tag{3.23}$$

where $\delta = f/f_B - 1$ is the frequency deviation from Bragg condition. To demonstrate the validation of this approximation, simulation has been performed under the condition $m = 1\%$, $\gamma = 0.64$, $N = 15$ and the results are shown in Figure 3.12. The discrepancy between the exact solution and the approximated solution is $< 4\%$ for amplitude and $< 2\%$ for phase terms within the main lobe frequency range.

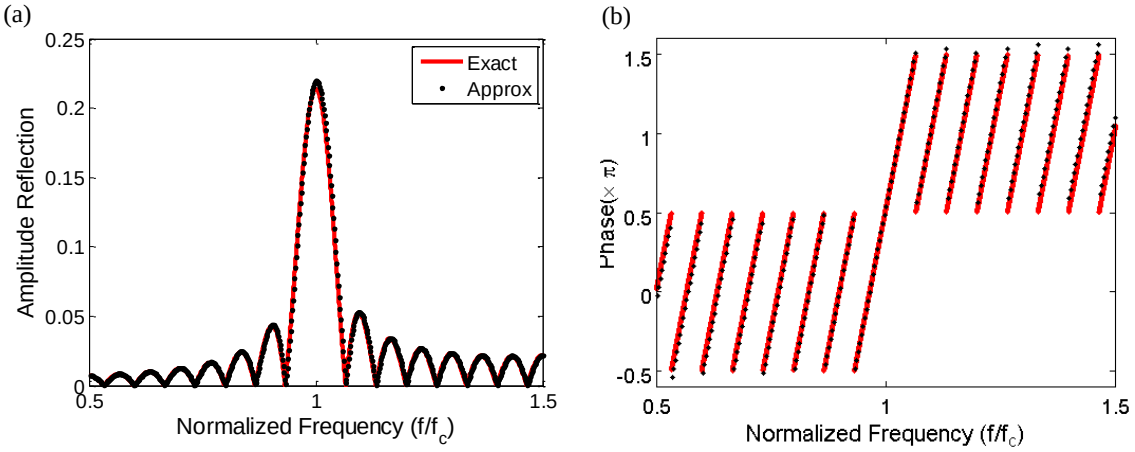


Figure 3.12: Simulation of an AFBG spectrum with transfer matrix model (a) spectrum amplitude (b) spectrum phase

Eqn. 3.23 indicates the peak frequency location and bandwidth of mainlobe are the same as Eqn. 3.10 and Eqn. 3.12, respectively. But by considering the notch width, transfer matrix gives more details about the reflection spectrum that multi-reflection model is incapable of. The peak amplitude reflection is

$$R_p = m\pi \frac{1/\gamma - \gamma}{2} N \tag{3.24}$$

By comparison with Eqn. 3.11, the effective reflection from each notch is obtained

$$A_1 = m\pi \frac{1/\gamma - \gamma}{2} \tag{3.25}$$

The phase term of Eqn. 3.23 is rewritten as

$$\phi = \pi N \left( \frac{1/\gamma + \gamma}{2} m + 1 \right) \frac{f}{f_B} + \pi(\frac{1}{2} + N - mN) \tag{3.26}$$

So $\phi$ is linearly related to wave frequency $f$ and it explains what is demonstrated in Figure

3.12. The slope of this relation is determined by Bragg frequency $f_B$, and thus provides an additional way for Bragg condition measurement besides the peak frequency location.

### 3.3.3 Optimization of parameters

Both multi-reflection model and transfer matrix model state that while $f_B$ of an AFBG is determined by the acoustic velocity on the waveguide and pitch length of the grating, the bandwidth and peak reflectivity of an AFBG is determined by the number of reflector elements within the effective length of the AFBG ($L_{\text{eff}}$). The effective length is determined by the smaller one of the acoustic pulse width and acoustic coherent length.

To achieve distributed sensing with multiplexed AFBGs, the reflectivity of each grating should be low enough to allow the interrogation pulse to reach the far end of the sensing fiber and suppress the high-order reflections within the AFBG. For the acoustic wave with frequency $f$, the acoustic signal reflected by the $i$th equivalent AFBG along the waveguide can be approximated as:

$$R_{\text{i}}(f) = (1 - R_{\text{eff}}(f))^{2(i-1)} R_{\text{eff}}(f) \tag{3.27}$$

where $R_{\text{eff}}(f)$ is the reflectivity of a single equivalent AFBG. Based on this model, the appropriate value of grating reflectivity can be calculated using the desired total number of multiplexed AFBGs. As plotted in Figure 3.13 (a), slight reduction of the single equivalent AFBG reflectivity ($R_{\text{eff}}$) can result in notable length extension of the entire sensor. By reducing $R_{\text{eff}}$ from -20dB to -23dB, the optimized grating number is extended from 50 to 100. From Eqn. 3.24, the dependence of $R_{\text{eff}}$ on notch parameters is simulated and shown in Figure 3.13 (b). For example, with $\gamma = 0.7$, $m = 0.01$ and $N = 10$, it is estimated that $R_{\text{eff}} \approx$-23dB. During the sensor design, the grating reflectivity will be optimized using this model for best overall signal quality.

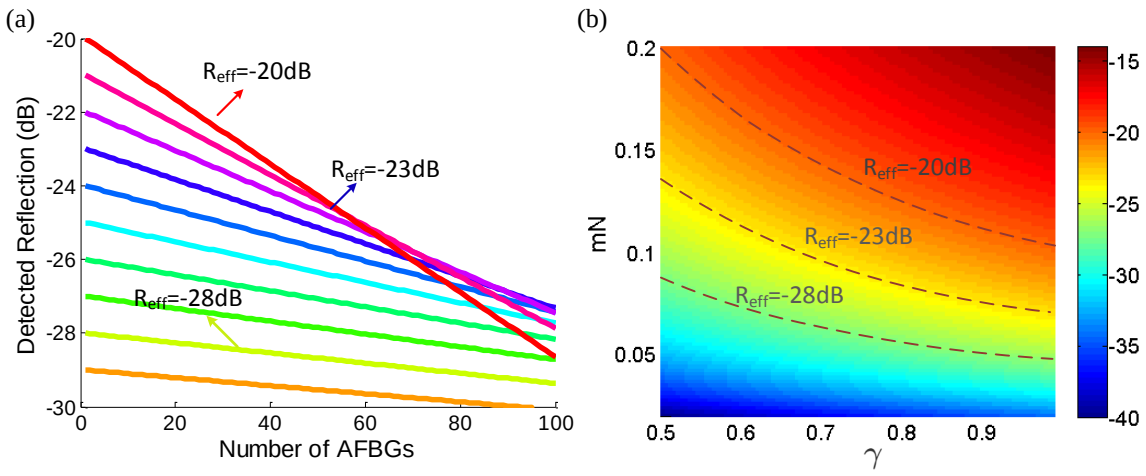


Figure 3.13: (a) Intensities of the acoustic waves reflected along continuous AFBGs with different reflectivities. $R_{\text{eff}}$: single equivalent AFBG reflectivity of the continuous AFBG. (b) Parameters influences on $R_{\text{eff}}$

## 3.4 Interrogation method

For a typical FBG interrogation system, there are two design schemes: 1) a broadband light source and a spectrometer with scanning detecting wavelengths. 2) A scanning wavelength light source and a photodetector. Similarly, an AFBG interrogation system could employ either of these schemes. For example, scanning the driving signal frequency for an acoustic transducer and detect the strength of reflection signals corresponding to each frequency. However, the scanning process is typically in minutes, and it significantly slows down the response speed of entire sensing system. Fortunately, the relatively low frequency (kHz∼MHz) of acoustic waves make it possible for time domain analysis and achieve much faster interrogation speed.

The fundamental principle of this fast interrogation method lies in the spectrum broadening effect due to limited time duration of a signal. An absolute single frequency signal must

spread over the entire time domain. Hence any real physical signal $s_r(t)$ has a range of frequency due to its finite time duration $a$. $s_r(t)$ could be treated as the multiplication result between an ideal infinite long signal $s_i(t)$ and a square window function $w(t)$, i.e.

$$s_r(t) = s_i(t) \times w(t) \tag{3.28}$$

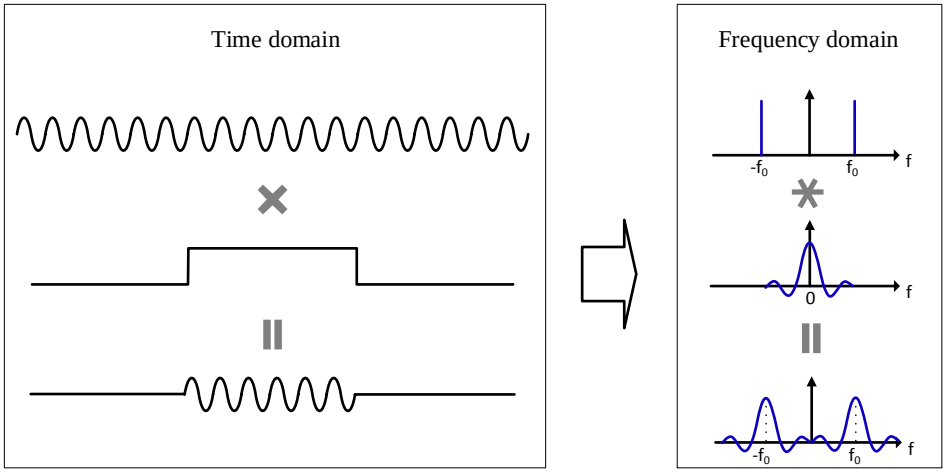


Figure 3.14: Signal with finite time duration has broadened spectrum.

The frequency characteristics of $s_r(t)$ could be obtained by taking the Fourier transform of Eqn. 3.28,

$$F[s_r(t)] = F[s_i(t) \times w(t)] = F[s_i(t)] * F[w(t)] \tag{3.29}$$

where $*$ denotes convolution operation. Since $Fw(t)$ is a sinc function with bandwidth $1.2/a$ (double side), the minimum bandwidth of $s_r(t)$ cannot be zero, even for a single frequency signal that bandwidth of $s_i(t)$ is infinitely small. This spectrum broadening effect is then used in AFBG demodulation algorithm.

For a N-cycle sinusoidal signal with frequency $f_0$, its time duration is $N/f_0$, so it is expressed

as

$$s(t) = A\cos(2\pi f_0 t)w(\frac{f_0}{N}t) \tag{3.30}$$

Then in positive spectrum domain

$$F\left[s(t)\right] = A\frac{N}{2f_0}sinc[\pi N\frac{f-f_0}{f_0}] \tag{3.31}$$

The center frequency is $f_0$ while the broadened bandwidth between the two zero amplitude points is $BW = 2f_0/N$.

From Eqn. 3.12, the bandwidth of a $N_a$-notch AFBG is $BW_a = 2f_p/N_a$. To effectively cover the entire AFBG spectrum, the spectrum of interrogation signal should be

$$BW > 5BW_a \tag{3.32}$$

If assuming the acoustic signal centers near the AFBG peak frequency, $f_0 \approx f_p$, the requirement on number of cycles for driving signal is

$$\frac{N_a}{N} > 5 \tag{3.33}$$

For example, for an AFBG with 15 notches, the interrogation signal should be no more than 3 cycles. So for sensing applications, as long as the shift of $f_p$ is less than BW, the spectrum of AFBG could still be accurately demodulated. Otherwise, $f_0$ could be shift to match the AFBG spectrum.

Another significant benefit of limited length of temporal interrogation signal is distributed measurement capability. As the few-cycle signal travels along the waveguide and interact with several AFBGs, reflection signals from different AFBGs arrive at detector with relative time delay. So that the received time domain signal could be segmented and the spectrum

properties for every AFBG could be resolved without any scanning process.

# Chapter 4

# Experimental demonstration of AFBG

The concept and theoretical analysis of AFBG have been described in previous chapters. In this chapter, AFBG structures are experimentally demonstrated for various sensing applications and their corresponding predictions from theoretical analysis are validated. AFBGs are fabricated by different methods, depending on its waveguide material. A femtosecond laser micromachining system is constructed to precisely introduce notches on silica optical fiber and press deformation by a plier is used to introduce notches on metal waveguides. AFBGs with different properties, not only in waveguide material, but also in pitch length, reflection ratio, etc. fabricated, characterized and compared to theoretical predictions. Furthermore, in addition to a single AFBG, multiplexed AFBGs are also investigated based on properties of reflection spectrum and transmission losses of an AFBG. Multiplexed AFBGs lead to the concept of a long, continuous AFBG, which has the potential for fully distributed sensing.

## 4.1 AFBG fabrication on thin waveguide

Single mode silica optical fiber (Corning SMF-28) and iron-chromium wire (Pelican Alloy 875, AWG 24) are chosen as the thin acoustic waveguides for AFBG demonstration. Silica optical fiber is chosen because of its highly uniform structural dimension, as well as the potential for photoacoustic interaction applications. Iron-chromium wire is chosen because of its flexibility and high temperature stability. Both waveguides are with extremely low price. Based on different material properties of silica and metal wire, different methods were used to fabricate AFBGs. Silica fiber geometry is commonly modified by a $CO_2$ laser or an ultrafast laser, the former changes fiber shape via thermal process while the later changes fiber shape via material removal. Ultrafast laser micromachining is used here due to its fine structure capability. For an iron-chromium wire, mechanical compressing method is used to generate periodic structures due to the large ductility and malleability of metals. The setups to fabricate AFBGs with tunable pitch length and reflection ratio have been constructed.

### 4.1.1 Femtosecond laser micromachining setup

Femtosecond laser has been employed for precise micromachining widely in recent years [93], from microfluidic channel creation [94] to phase mask repair [95]. It demonstrates much higher precision compared to conventional mechanical machining method or the micromachining system based on nanosecond lasers, taking advantage of the 'zero thermal effect' of femtosecond laser [96]. Starting with a femtosecond laser, an entire micromachining system was built to inscribe fine structures on both silica and sapphire materials.

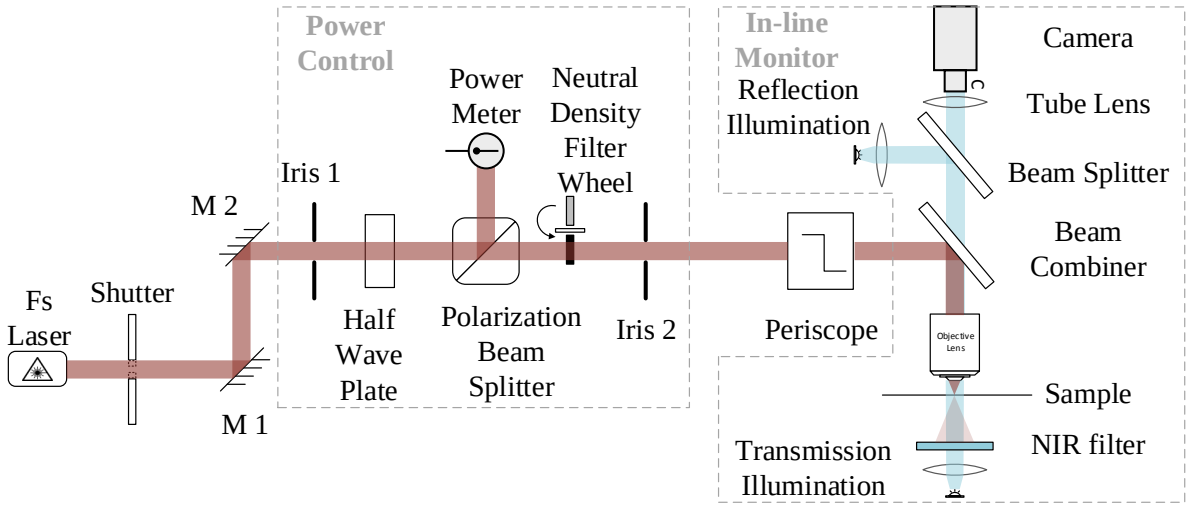


Figure 4.1: Schematics for the automated femtosecond laser micromachining system.

Figure 4.1 illustrates the schematics of the micromachining system. External shutter is used to control the pass or block of light beam with computer. The first two steering mirrors, functioning as a periscope, could alter the beam to an arbitrary 3D direction, aligning the beam to the rest of optical system. Two irises were placed in the optical path to fix the beam direction so that the power control components are well aligned. For the optical power control section, since the laser beam is linearly polarized, a combination of half wave plate (HWP) and a polarization beam splitter (PBS) could tune the laser power finely. The laser power is also monitored by the power meter simultaneously. A neutral density (ND) filter wheel is added to coarsely control the laser power. Another periscope formed by two mirrors pass the fs laser beam into in-line monitor section, where the fs laser beam share the light path with visible light for imaging purpose. A hot mirror works as a beam combiner because it reflects near infrared fs laser beam (780nm) while passes visible illumination light (400∼700 nm). The combined lights beams are focused by an objective lens onto the sample. The fs laser beam causes damages on the sample while visible light forms the image of the sample and damages, realizing in-line monitoring of the micromachining process. Both reflection and

transmission illumination are embedded into the system so that it works for both transparent and opaque samples for machining.

Besides the optical system described above, mechanical system to precisely move the fiber sample is equivalently important. A 3D translation stage, a piezo stage, a 1D translation stage and two rotation stages are included in the system to perform various types of movement of sample. In this particular setup, the following stages are used: Applied Scientific Instrument (ASI) 3D stage, Physiks Instrumente (PI) piezo stage, PI M126 stage, two Thorlabs rotation stages and Newport ESP300 controlled stages. Piezo stage could achieve nanometer accuracy while other stages give $0.1\mu m$ accuracy.

Software control is the brain for the entire system. Since all these stages are bought from different vendors, no commercial software is available to control all parts. A LabVIEW platform based program is developed to control the external shutter and all stages, and it has excellent flexibility to add more equipment. The behavior of all devices can be controlled through the buttons on GUI in the manual mode or direct command input in the script mode (shown in Figure 4.2).

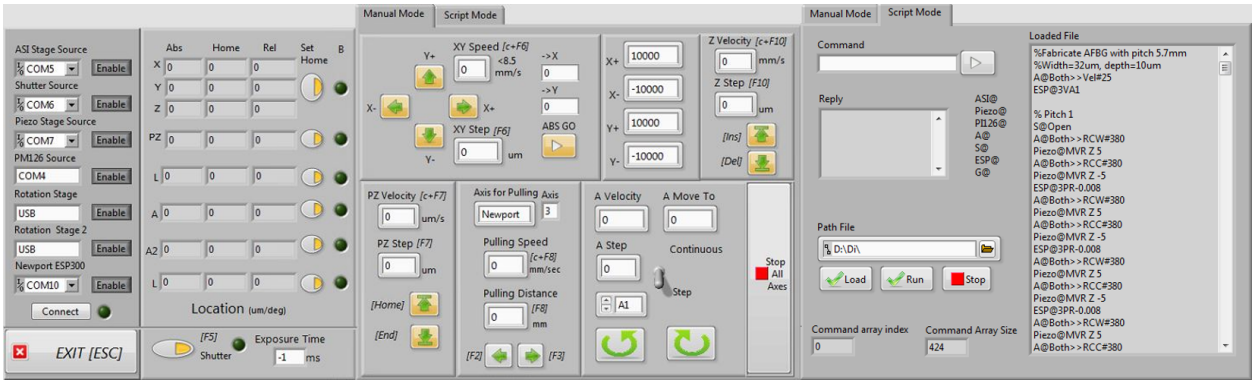


Figure 4.2: User interface for micromachining control software.

In order to achieve high extendability of the program so that more devices could be added into the system in the future, JKI string-based queued state machine structure is chosen for

the main VI. The flow chart in Figure 4.3 illustrates the program diagram, including the initialization, parallel check loop and the main loop. The initialization section ensures all the data and control appearance are in default status and takes the users input for what stages to enable. After the initialization, the check loop and main loop run parallel in response to the button input as well as to update the position and status of each stage. In the manual mode, the main loop stays in idle state if no input is generated. Otherwise, it enters into other states that execute a specific action according to each control button. In script mode, text based commands and script can be processed by the program and control stages and the shutter for consecutive actions. It resembles the function of CNC controlling software.

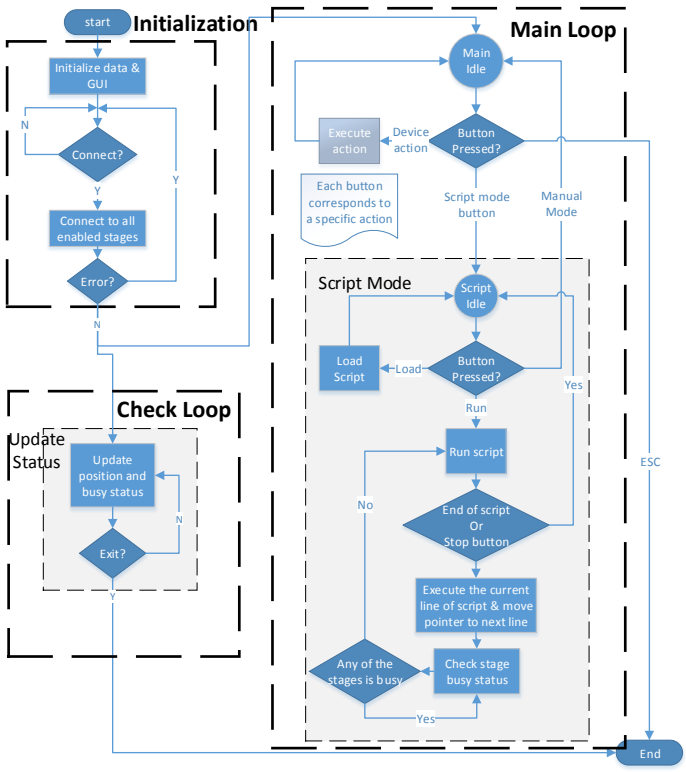


Figure 4.3: Program diagram for micromachining control.

Using the integrated software control, various microstructures are realized, and some ex-

amples are shown in Figure 4.1. For the subfigures, (a) Three letters inscribed on a glass slide. (b) Point-by-point FBG writing inside a single mode fuse silica optical fiber. (c) Through hole milling on a sapphire wafer with $250\mu m$ thickness. (d) Channel opening on a hollow core polymer fiber. These results demonstrate the capability of femstosecond laser micromachining setup for various materials, geometries and inside medium operation.

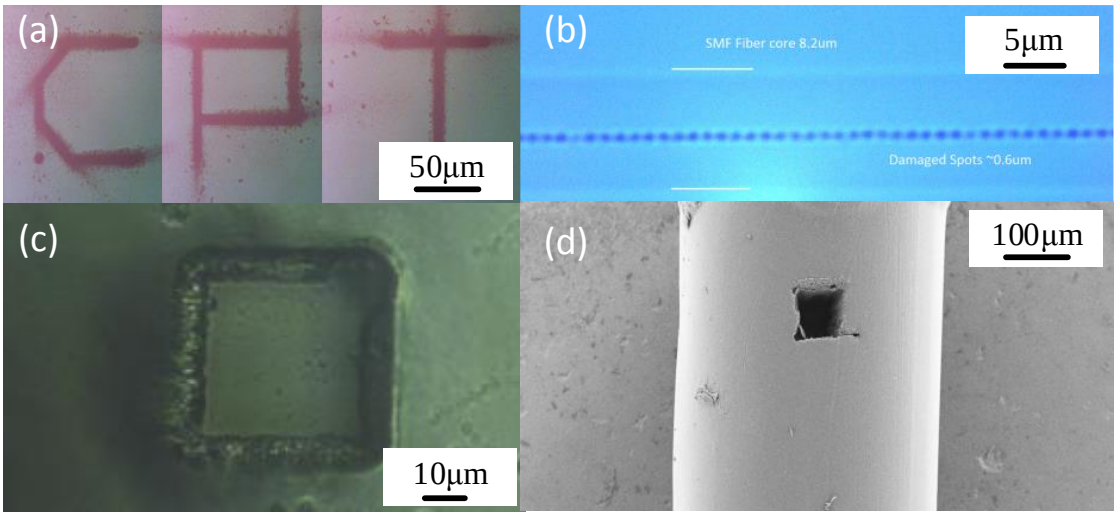


Figure 4.4: Various machining results with femtosecond laser micromaching system. (a) Three letters inscribed on a glass slide. (b) Point-by-point FBG writing on a single mode fuse silica optical fiber. (c) Through hole milling on a sapphire wafer with $250\mu m$ thickness. (d) Channel opening on a hollow core polymer fiber.

### 4.1.2 AFBG inscription on optical fiber

An AFBG was inscribed on an optical fiber by the above femtosecond laser micromachining system. In order to introduce effective perturbation of acoustic impedance, optical fiber surface is lathed with periodic notches, resembling the periodic structure in [89], but on much thinner waveguide. The most challenging task to achieve such highly accurate micro-

lathing result is to maintain the axial and radial position of fiber during rotation process. Several techniques are included to secure the fiber in place: 1) the optical fiber is inserted into two ceramic ferrules which have inner diameter $128\mu m$, slightly larger than the fiber diameter $125\mu m$. So the eccentricity of fiber is kept smaller than $3\mu m$ during rotation. Those two ferrules are fixed on a 3D stage with the focal point of the objective lens located in between as shown in Figure 4.5 (a). Since the fiber is strictly confined by two ferrules, its location could be precisely adjusted to desired position with the 3D stage. 2) Both ends of the optical fiber are fixed on rotation stages so that they could be rotated simultaneously. The rotation angle is thus well controlled. These two rotation stages are rigidly connected through a metal rod and one of the them is fixed on a 1D translation stage. So the axial movement of the fiber is also precisely controlled as shown in Figure 4.5 (b).

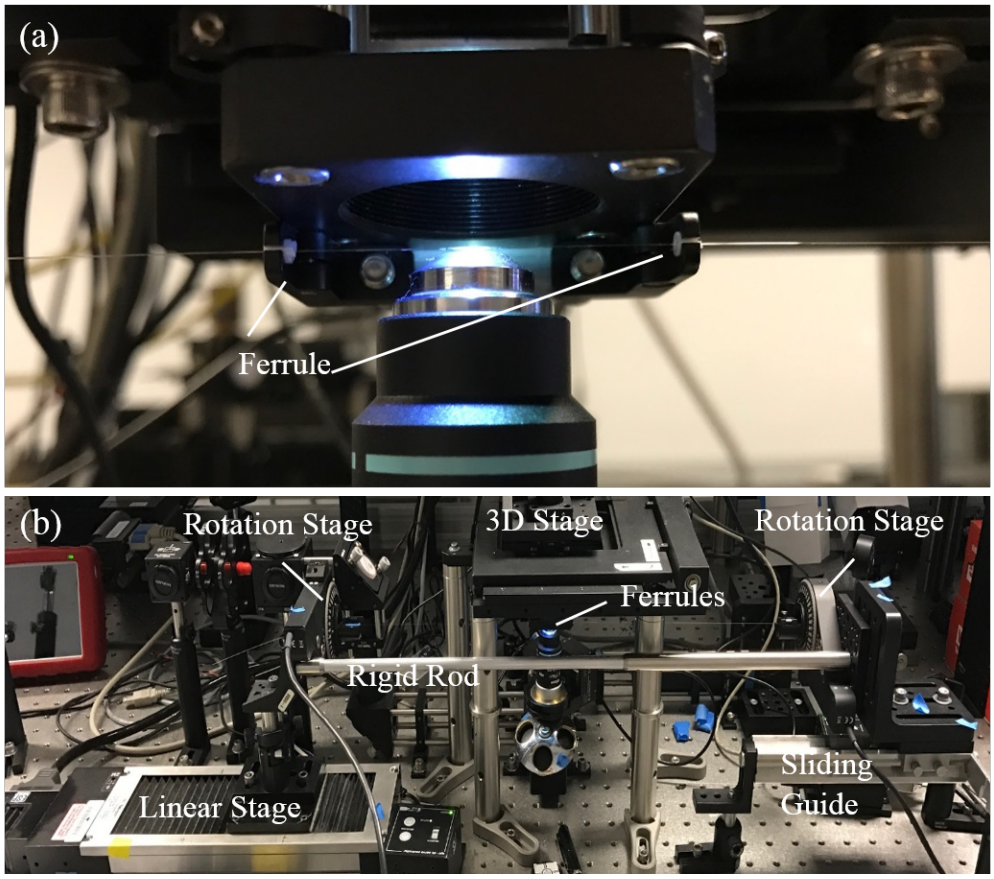


Figure 4.5: AFBG fabrication setup with femtosecond laser.

With successful demonstration of stable rotation process of the optical fiber, fs laser is then turned on to start machining. Average laser power is controlled to be 10mW with repetition rate of 5kHz (pulse energy is $2\mu J$). A 40X objective lens is used to focus the light beam to $5\mu m$ in diameter. The resulting damage spot is slightly smaller due to the Gaussian shape of laser beam and the multi-photon nature of blasting with fs pulse [97]. Fiber rotation velocity is limited by the rotation stage capability to $25^o/s$, i.e. 15 s/turn. With pitch length around 5.7mm, an effective notch width needs to be $> 10\mu m$ (0.2%). So the fiber is rotated several turns to increase the damage area for one notch structure. In this way, precisely cut samples are fabricated as shown in Figure 4.6.

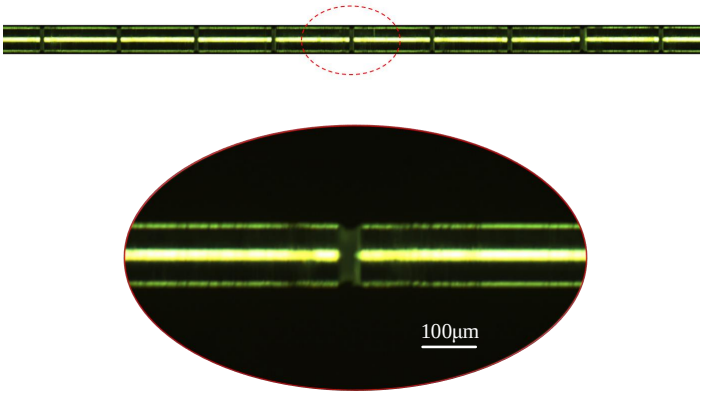


Figure 4.6: Machining result of an AFBG on optical fiber.

### 4.1.3 AFBG inscription on metal wire

One of the significant advantages of AFBG over optical FBG is that acoustic wave could travel for relatively long distance over almost all elastic materials, including metal. So an AFBG sample is fabricated on a metal wire for demonstration. Unlike hard and brittle silica, metals are much easier for shape modification without break. A mechanical compress method is used to realize fast fabrication process. As shown in Figure 4.7, a metal wire (Pelican Alloy 875, , Chromium: 21%, Aluminium: 5.5%, Iron: Balance) is dragged by a 1D translation stage on one end for precise movement and is tied to a weight on the other end to keep straight. The wire also passes between two sharp clamps of a plier and a dent on the wire is introduced by closing the plier. There is a predetermined round hole on the clamp so that the dent introduced by closing the plier is identical every time. Multiple dents are produced to form a periodic structure on the metal wire and the distance between those dents are controlled by a translation stage to match with acoustic velocity. An example of fabricated AFBG on a metal wire is shown in 4.8. Each dent takes only one second so this process is much faster than micromachining method for an optical fiber.

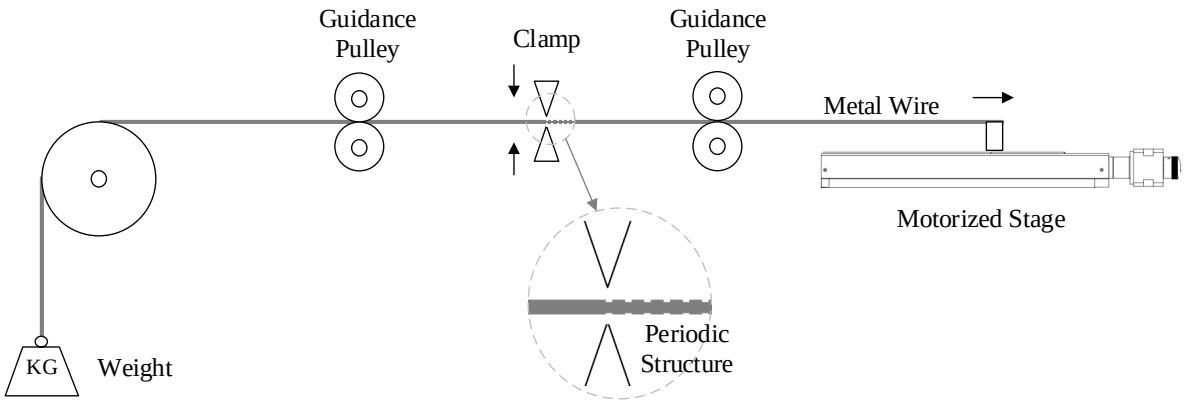


Figure 4.7: Machining setup for AFBG on a metal wire.

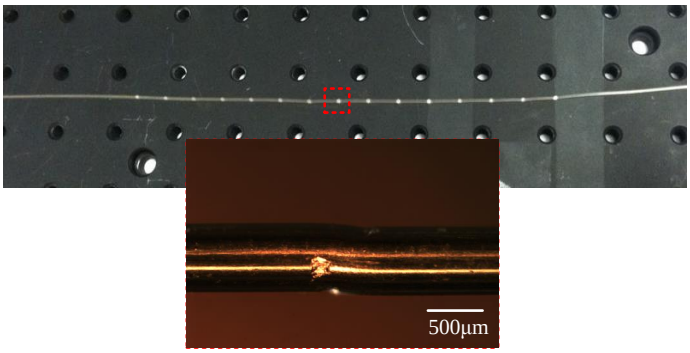


Figure 4.8: Machining result of an AFBG on a metal wire.

## 4.2 Interrogation system for AFBGs

An interrogation system is built to measure various AFBGs properties, like reflectance and resonance frequency. Only with accurate demodulation of these parameters can AFBG be used as reliable sensors. There are several requirements on the interrogation system to demonstrate the advantages of AFBG over its optical counterpart: 1) efficient acoustic/electrical signal conversion, 2) low price components, 3) fast interrogation capability, 4) distributed interrogation capability and 5) reflection detection scheme. This section describes

a system that satisfies all these requirements.

### 4.2.1 System design

The core of the interrogation system starts from efficient acoustic/electric energy conversion. Piezo element has been widely employed as efficient and economic devices for this purpose. But a single piezoelectric element has very narrow bandwidth for efficient energy conversion, which causes the driving signal to oscillate for a long period of time. So it prohibits the fast interrogation method described in Section 3.4. Fortunately, this narrow bandwidth property can be easily modified by adding backing material to damp the additional oscillation so to increase the bandwidth of piezoelectric element. The combination of a piezoelectric element and some proper backing material leads to different types of acoustic transducers. An acoustic transducer with center frequency matching that of AFBG and wide bandwidth covering the whole AFBG spectrum is chosen for the system.

Suitable electronics are required to drive the acoustic transducer as well as to process the received signal from the acoustic transducer. Voltage, frequency and impedance match are the fundamental considerations. A function generator and a power amplifier are combined to properly drive the acoustic transducer, which provides several pulse trains with enough bandwidth for fast AFBG interrogation. The returned signal is amplified by a preamplifier so that it can be detected effectively by an oscilloscope. Since the working frequency is $\sim$1MHz, all these electronics could be built with a low price microprocessor and its peripheral circuit.

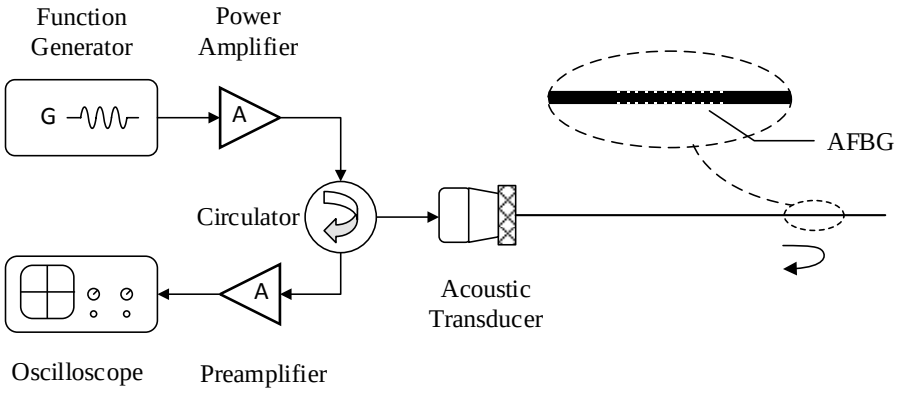


Figure 4.9: Interrogation system schematics for an AFBG.

The system schematics is illustrated in Figure 4.9. Obviously, to realize the reflection detection scheme, a circulator is indispensable. Generally, the circulator could be placed either in the acoustic part or in the electronics part. Because an acoustic waveguide needs tremendous modification to perform as a circulator and a dual-element transducer is much more expensive and inefficient compared to a standard one, an electrical circulator is a better choice for this system. With this circulator, the driving signal passes to the acoustic transducer, which generates corresponding acoustic waves. The acoustic wave is coupled onto waveguide and propagates until it is reflected by an AFBG. The reflected wave propagates along the waveguide and couples back to the transducer. This received signal is converted back into electrical form and passes through the circulator to preamplifier. After some pre-processing like noise filtering and signal amplification, it is recorded by an oscilloscope.

In the following subsections, each component is thoroughly analyzed so that a low-price and rugged interrogation system would be possible for future commercialization.

### 4.2.2 Details of components in the system

#### Electrical circulator

The circulator is a critical self-designed component in the system. The isolation requirement is high since the driving signal is about four orders of magnitude stronger in amplitude compared to the reflected signal. If isolation is insufficient, strong driving signal would leak to the preamplifier and possibly cause damage. Since the working frequency is around 500kHz and no commercial circulator could functions normally at such low frequency, a time-based fast switching circulator is designed and implemented.

Two switches are combined to perform as a circulator, taking advantage of the fact that the signals could be easily separated in time domain, shown in Figure 4.10. The first switch is a high power switch (HPS), allowing the driving signal (with high voltage and current) to pass at first and then cut the noise off. The second switch is a high speed switch (HSS), cutting off the strong driving voltage from preamplifier and later passing the weak reflection signal ($< 10mV$) to the preamplifier. Reed relays (Mouser 876-DIP12-1A72-12D) are chosen as the HPS because of its high power capability ($> 100V$ and $> 0.5A$), relatively fast response ($< 300\mu s$), and high isolation ($> 10^{12}\Omega$). A solid state switch (Digikey MAX14758 EUE+-ND) is chosen as the HSS because of its fast response ($< 50\mu s$), ultra-low noise and relatively high voltage capability ($\pm 35V$). Its power isolation is better than $-60dB$ at frequency $<$ 1MHz.

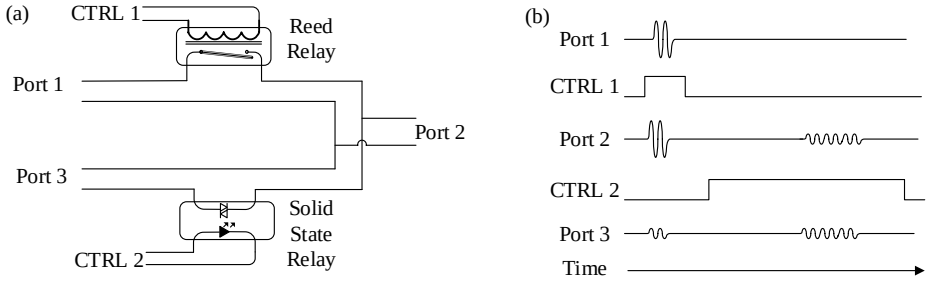


Figure 4.10: (a) Electronic circulator diagram. (b) Time sequence signals for electronic circulator

### Preamplifier design

A preamplifier is designed to best fit reflection signal properties, which includes a strong signal section leaked from driving signal and a weak signal section from AFBG reflection. The AFBG reflection is so low that an amplification of about 100X is necessary. Three stages of amplification are built with operation amplifiers (Model AD823ANZ, 17MHz Gain-bandwidth product). Each stage contributes a gain of 4.3. So total gain is around 80. Diagram is shown in Figure 4.11 (a). But the strong signal is also magnified and it causes waste of detection dynamic range of oscilloscope. So a saturation circuit is used to pass strong noise (leaked from driving signal) to ground while keeping the reflection signal untamed for detection. It should be noted that the input impedance of oscilloscope is set to 1MΩ to avoid signal distortion.

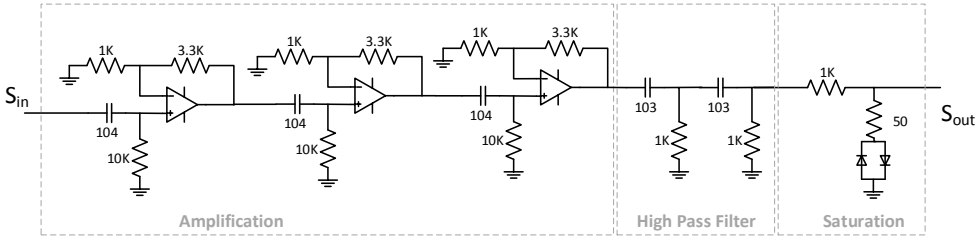


Figure 4.11: Preamplifier design.

### 4.2.3 System test result

The system is tested with no AFBG in place as shown in Figure 4.12. The leaked driving signal is obvious in the plot. In addition to this, a $\sim 300\mu s$ dead zone is caused by overshoot of the HSS. For this reason, a lead-in waveguide around $1.5m$ is included for future AFBG interrogations.

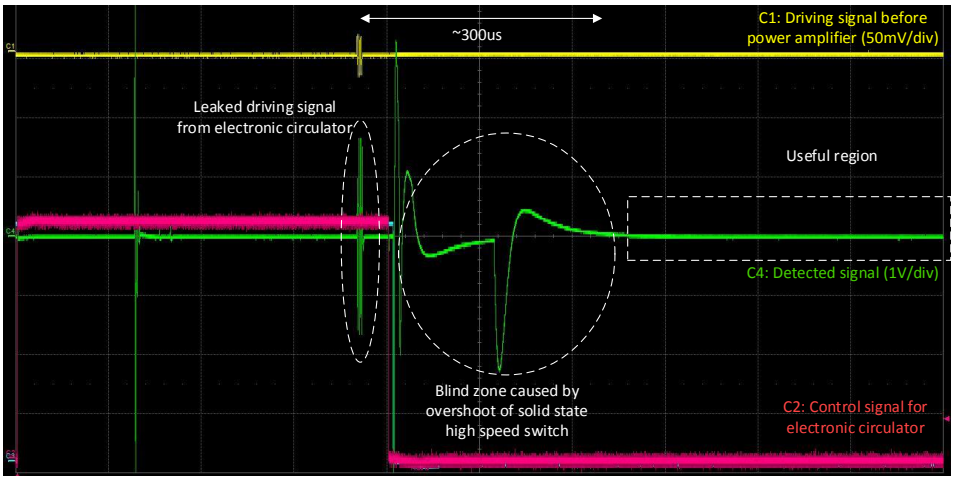


Figure 4.12: Interrogation system test result.

## 4.3 AFBG properties

With the above interrogation system, various AFBGs are characterized for their reflection spectrum properties, including intensity, resonance frequency, bandwidth, etc. AFBGs with $10 \sim 15$ notches on both optical fiber and on metal wires are first investigated. For both cases, physical structures of the notches are carefully measured to obtain parameters for simulation, either based on multi-reflection model or on transfer matrix model. Experimental results are compared to simulation results for detailed analysis. To demonstrate the remote sensing capability of AFBG, a lead-in waveguide over 10 meters is added between the acoustic

transducer and the AFBG. The degradation in signal quality is estimated. Furthermore, several discrete AFBGs are multiplexed together on the same waveguide. This proves the low transmission loss of AFBG structures and demonstrate its capability for quasi-distributed sensing. By reducing the distance between multiplexed AFBGs to zero, a long, continuous AFBG is fabricated and investigated. This continuous AFBG increases the spatial resolution not only to the length of AFBG compared to discrete multiplexing case. By eliminating the gap distance, it can accurately realize a spatial resolution to a fraction of AFBG length with special demodulation algorithm. These investigations of AFBG properties lay a solid foundation for sensing applications discussed in the next chapter.

### 4.3.1 AFBG on waveguide

#### AFBG on optical fiber

A sample of AFBG on a silica fiber (Corning SMF-28) is fabricated with femtosecond laser micromachining system. 15 notches are inscribed with 5.77mm pitch length. The notch structure is examined under microscope and it is shown in Figure 4.13. From the picture, it is measured that the fiber diameter is $125\mu m$, the notch section diameter is $116\mu m$ and the notch width is $30\mu m$. The notch is slightly tilted ($\sim 10\mu m$), but it is less than 0.1% of acoustic wavelength, so it is treated as perpendicular to fiber axis.

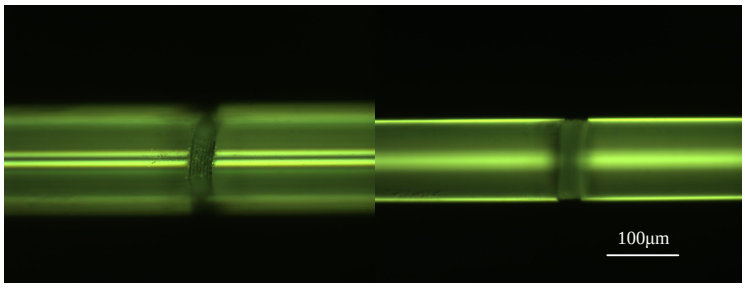


Figure 4.13: An AFBG sample on an optical fiber

Both ends of the optical fiber are cleaved and one end is glued to the acoustic transducer surface. So the acoustic wave is coupled from transducer to the optical fiber. The acoustic wave propagates along the optical fiber and is reflected by the AFBG structure and also by the fiber end, as shown in Figure 4.14 (a). The fast interrogation method describe in Section 3.4 is used for this demonstration. The signal from AFBG has an amplitude of about 2mV while the amplitude of end reflection is about 130mV. Considering that the AFBG reflection signal is expanded longer in time domain, the signal power ratio between reflections from AFBG and fiber end is $1.3 \times 10^{-3}$. Due to the large impedance mismatch between optical fiber and air, the reflectance on fiber end is approximately unity. Therefore, the reflectance of this AFBG is $1.3 \times 10^{-3}$.

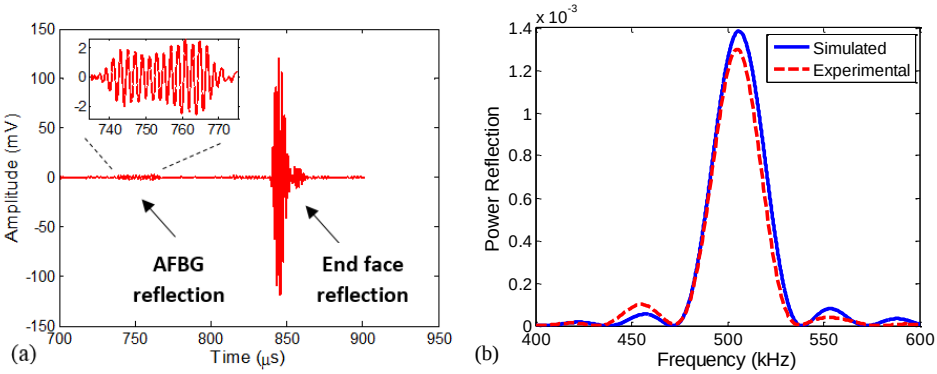


Figure 4.14: An AFBG sample on an optical fiber: (a) reflection signal in time domain; (b) experimental signal in spectrum domain, compared to theoretical data.

The reflection signal from AFBG is located at $730\mu s$. Accounting the acoustic velocity on an optical fiber 5.77km/s, the AFBG is $2.08m$ from the acoustic transducer, ignoring the time delay due to electronics ($< 10\mu s$). This is also the fundamental limit for the interrogation rate. If the reflection signal from fiber end is terminated, repetition rate of driving signal could be increased to 1kHz. With current signal strength, 100 consecutive scans are averaged to reduce system noise. So the effective interrogation rate for the AFBG is 10Hz. With

further enhancement of signal strength and shorter waveguide length, it could be increased over 1kHz.

The Fourier transform of the AFBG reflection signal is calculated to obtain power reflection spectrum, as shown in 4.14 (b). As a comparison, the simulation result based on notch structure dimension and transfer matrix method is also displayed. Their spectrum profiles are highly consistent. The reflectance, peak frequency location, bandwidth (two zeros points of mainlobe) from simulation prediction are $1.38 \times 10^{-3}$, 505.9kHz, 67.4kHz, respectively. And these values are $1.30 \times 10^{-3}$, 505.1kHz and 65.6kHz for experimental measurement. The discrepancy for these number are 5.8%, 1.6% and 2.7%, respectively. The 1.6% difference between theoretical peak frequency location and the experimental data is especially remarkable. These slight discrepancies mainly comes from the AFBG dimension error, especially the notch depth and width. But they are small enough to validate AFBG concept as well as prove the accuracy of theoretical model.

**AFBG on metal wire**

An AFBG inscribed on a metal wire (Pelican Alloy 875) is also tested. The pitch length is chosen to be 5.5mm according to acoustic wave velocity on metal so that its resonance frequency is at 500kHz. 15 notches are introduced and each notch deformation is intentionally increased to enhance SNR. The fabrication result is shown in Figure 4.15, which is obviously more severely deformed than that in Figure 4.8. The deformation is not a cylindrically symmetric notch and the notch width is about 10% of the pitch length, transfer matrix with narrow notch width approximation model is thus invalid here.

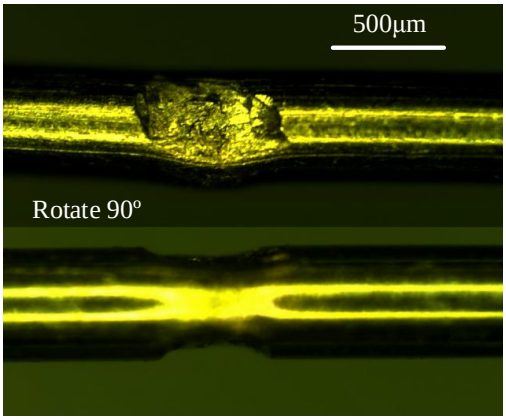


Figure 4.15: An AFBG notch on a metal wire.

The reflection signals in time domain and their spectra are shown in Figure 4.16. Subfigure (a) shows reflections from the AFBG as well as that from wire end face. Subfigure (b) demonstrates their spectra calculated through Fourier transform. Obviously, the power ratio between AFBG reflection and end face reflection is several orders higher than that in the optical fiber case. This is due to the severe deformation of metal for each AFBG notch. It also is worth noticing that there is significant insertion loss in AFBG here.

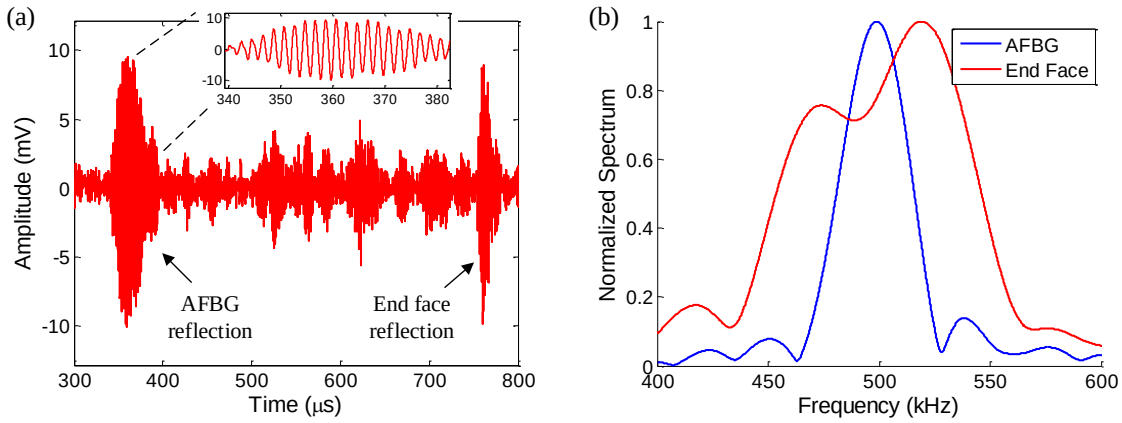


Figure 4.16: (a) Reflection signal from AFBG and from wire end face. (b) Spectra calculated through Fourier transform.

Furthermore, a frequency scanning method is used to investigate the properties of this AFBG. A 20-cycle sinusoidal pulse train is launched onto the waveguide. Due to the much longer duration in time domain, the bandwidth of this 20-cycle signal is much narrower than that of a 3-cycle signal used for fast interrogation method. The frequency is scanned over the interested region 350∼650kHz with a 2kHz step. Reflection signals at 450kHz, 500kHz and 550kHz are displayed in Figure 4.17 (a) as examples. At each frequency, the power of reflection signals from AFBG and from end face are calculated. The spectrum of reflections from AFBG and end face are shown in Figure 4.17 (b). By comparing Figure 4.17 with 4.16, it can been seen that the fast interrogation method and scanning frequency method are highly consistent, especially for AFBG spectrum measurement. Since the interrogation method takes about 3 minutes while the fast interrogation method only takes about 1ms, the benefit of using the later for signal demodulation is quite obvious.

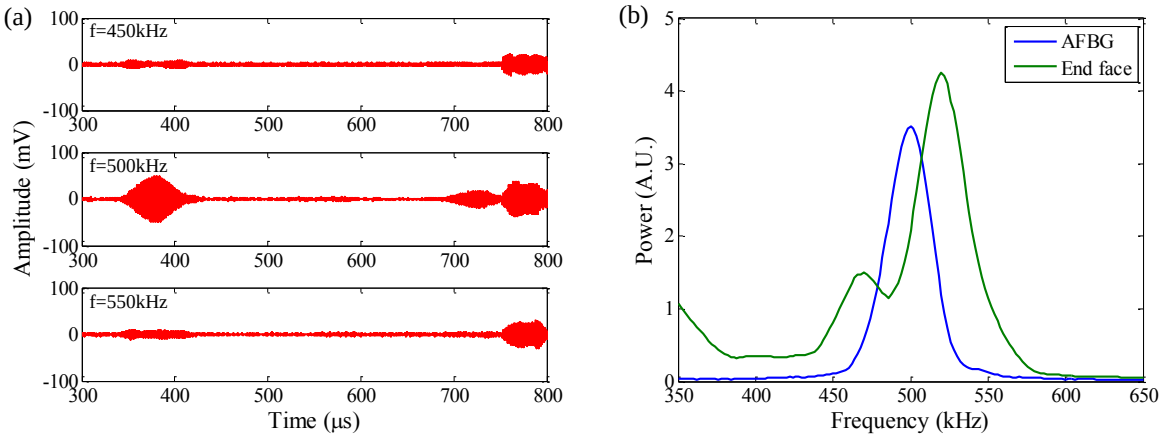


Figure 4.17: The AFBG spectrum measurement with scanning frequency method. (a) Reflection signals at different interrogation frequencies. (b) Spectra for AFBG and end face.

### 4.3.2 AFBG with long lead-in waveguide

One of the advantages of AFBG is that it allows electronics to be placed far away from the location to be sensed. To achieve that, a long lead-in section of waveguide between the AFBG and acoustic transducer is necessary. The theoretical attenuation in bulk fused silica is $< 0.01dB/m$ at 500kHz. Even though based on this number 10 meters of lead-in waveguide should not introduce more than $0.1dB$ attenuation, the current acoustic waveguide attenuation is more influenced by surface contact, since the acoustic energy is distributed onto the waveguide surface. Experiment has been conducted to estimate the overall attenuation introduced by the long lead-in waveguide, including the intrinsic material attenuation as well as the surface contact attenuation.

A 10m long SMF is de-coated and then glued to the acoustic transducer. It is freely laid out on a clean optical table, shown in Figure 4.18 (a). The optical fiber end is cleaved multiple times and the reflection signal is recorded. Then 9m of this fiber is removed and the reflection from the remaining 1m fiber are measured. Figure 4.18 (b) displays the results for short length waveguide ($t \approx 600\mu s$) and for long length waveguide ($t \approx 3300\mu s$). It is observed that there is a certain degree of variance between different measurement even with similar length of waveguide. But the average peak amplitude for $t \approx 600\mu s$ is 82mV while that for $t \approx 3300$ is 42mV. This indicates around 6dB power loss for $2700\mu s$ delay, or for 7.8m extra waveguide length. Thus the power loss is 0.77dB/m. This measured loss is much larger than the intrinsic material loss ($< 0.01dB/m$). So the improvement to reduce the surface contact loss is beneficial to increase the sensing distance for AFBG.

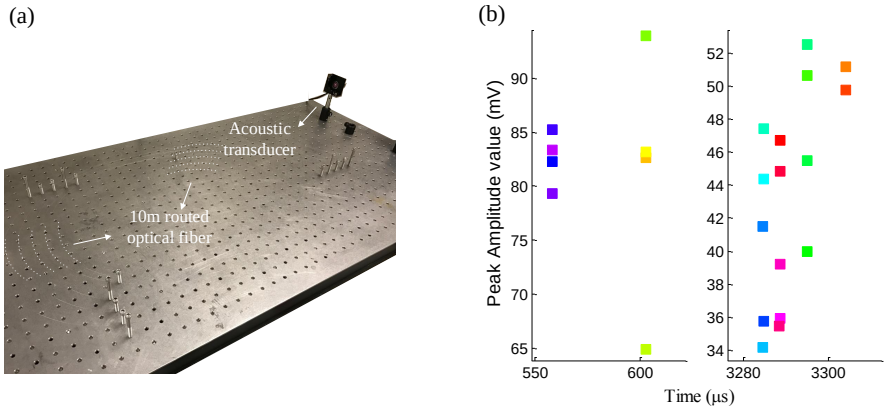


Figure 4.18: (a) Experiment setup for 10m optical fiber freely laid out on an optical table. (b) End reflection signal strength comparison between that for long and short waveguides.

An AFBG on a optical fiber is spliced to the end of the 10m lead-in waveguide. The reflection signal from the AFBG and its spectrum are displayed in Figure 4.19. The time domain signal is much weaker in amplitude compared to that in Figure 4.14. But fortunately, its spectrum profile is still well defined and AFBG is still suitable for sensing applications.

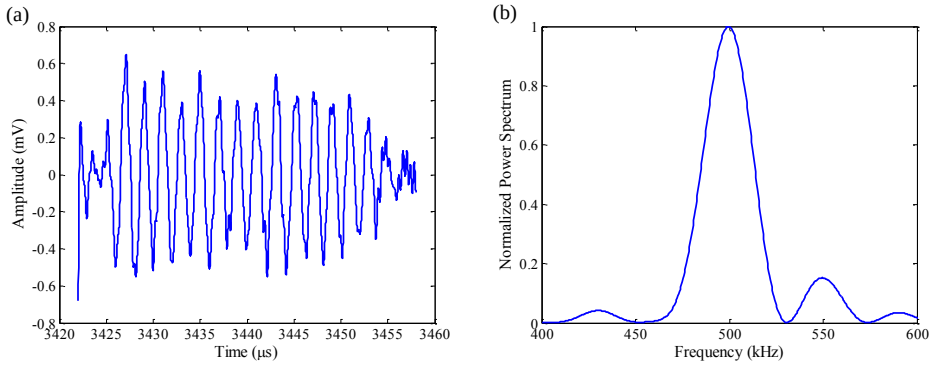


Figure 4.19: Time domain signal and spectrum for an AFBG on optical fiber with a 10m lead-in waveguide.

### 4.3.3 Multiplexed AFBG

Multiplexing capability of AFBG is investigated with three cascaded AFBGs on an optical fiber. These AFBGs are micromachined consecutively with same parameters, 15 notches and 5.7mm pitch length. The lead-in fiber is around 2m long and the distance between three AFBGs and the fiber end is $\sim 170mm$, $\sim 140mm$ and $\sim 320mm$.

The fast interrogation method is used for demodulation. A three-pulse sinusoidal signal is generated and coupled onto an optical fiber waveguide. Reflected signals are received and the results are presented in Figure 4.20. The four reflections start at $810\mu s, 870\mu s, 920\mu s$ and $1030\mu s$ are corresponding to three AFBGs and the fiber end, respectively. Considering the acoustic velocity 5.77km/s, the distance between them are 173mm, 144mm and 316mm, respectively. These are consistent with the physical distance and confirm the source of these reflections.

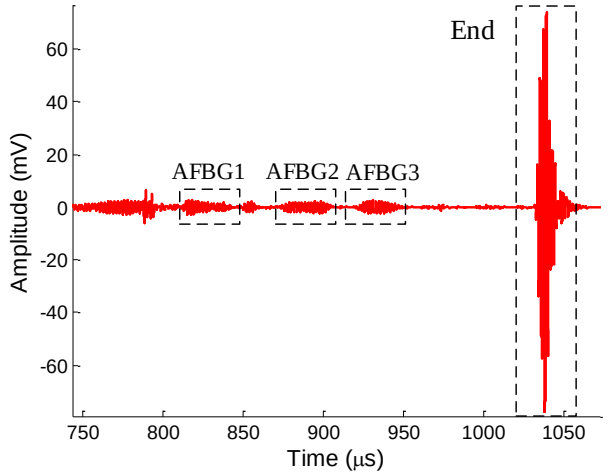


Figure 4.20: Reflection signal from multiplexed AFBGs and fiber end.

To characterize the properties of AFBG, the response from the end reflection is first analyzed.

Reflection signals from the fiber end shows different behaviors when the driving signal is centered at 500kHz and at 560kHz, shown in Figure 4.21 (a). When the driving signal is at 500kHz, there are two peaks, located at 490kHz and at 540kHz. In the meantime, when the driving signal is at 560kHz, only one peak shows up, located at ∼560kHz. From these behaviors, we could estimate the response peak of the transducer is located at around 540kHz.

Furthermore, reflection signals for each AFBG under driving signal centered at 500kHz and 560kHz are compared, shown in Figure 4.21 (b) (c) (d). Due to the short temporal length of signals, spectral resolution is limited to 1.6kHz. The peak frequency for each AFBG under 560kHz and 500kHz driving signal is 506.6kHz and 503.5kHz (AFBG 1), 506.6kHz and 505.1kHz (AFBG 2), 506.6kHz and 505.1kHz (AFBG 3). The variation is within spectral resolution, so driving signal with both 560kHz and 500kHz are valid. Since 500kHz driving signal results stronger signal intensity, it should be used for future interrogation system.

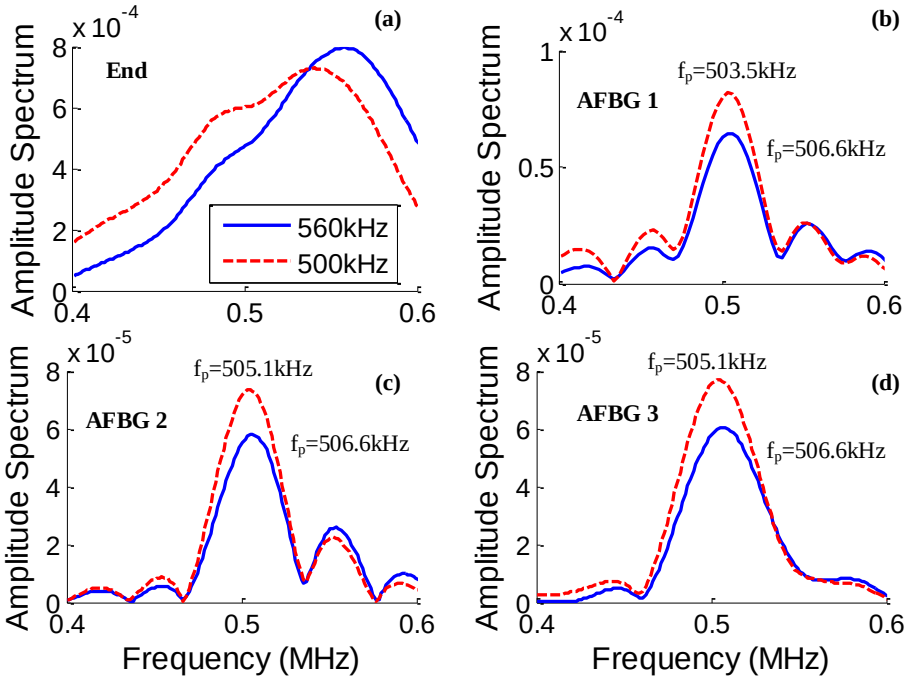


Figure 4.21: Reflection signal from multiplexed AFBGs and fiber end.

This multiplexed AFBG chain also demonstrate that the insertion loss of an AFBG is very low, from the signal amplitude comparison between AFBG 1 and AFBG 3. Therefore, it is possible to multiplex many more AFBGs to realized quasi-distributed sensing.

### 4.3.4 Long continuous AFBG

The above section shows AFBGs could be multiplexed to perform as a multiple-point sensor. More interestingly, if the distance gap between these individual AFBGs disappears, a long continuous AFBG is formed. The benefit of this long continuous AFBG not only lies in higher spatial resolution because larger number of AFBGs could be inserted within a certain length, but also in the flexibility to treat arbitrary section of reflectors as AFBG so that a fully distributed sensing capability is achieved.

When a pulse is transmitted along the long AFBG, it is continuously reflected, resulting a continuous oscillating reflection signal. Each section of the continuous signal corresponds to each short section of the long AFBG. So, any acoustic property change of this specific short section of AFBG could be resolved by analyzing the corresponding section of reflection signal.

An metal wire is inscribed with a long AFBG. The AFBG consists of around 200 pitches, with pitch length $5.5mm$ (resonance frequency $\sim$ 500kHz), so the entire AFBG is $\sim 1.1m$ long. The reflection signal from this AFBG is shown in Figure 4.22. The signal starts at $466\mu s$ and ends at $830\mu s$. This time duration of $364\mu s$ corresponds to waveguide of $1.0m$. Theoretically, The amplitude of reflection signal along the AFBG should be uniform (loss is sufficiently low) or monotonously decreasing (loss is relatively high). But in reality, due to the variation of reflectance from each notch and inevitable surface contact reflections, the amplitude of reflection signal varies.

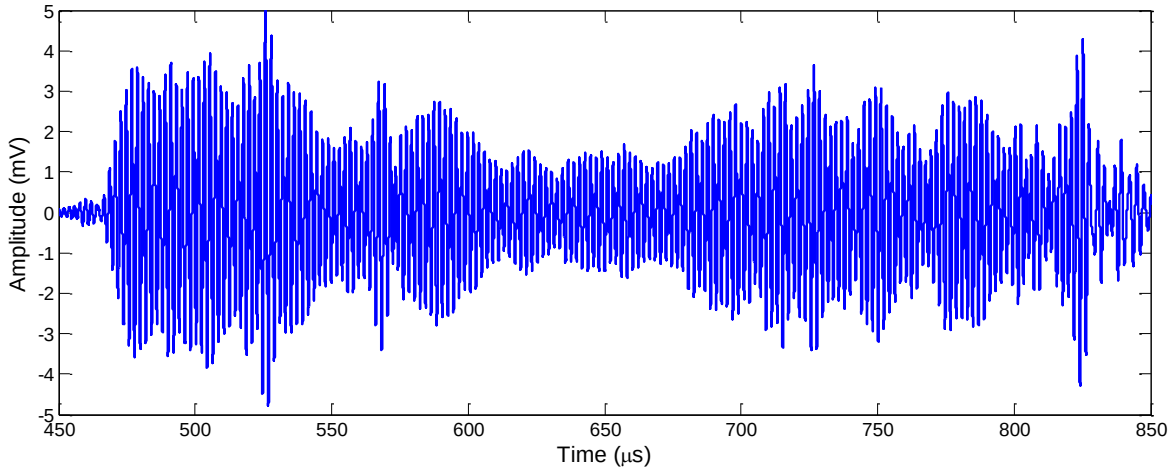


Figure 4.22: Reflection signal from a long continuous AFBG.

One way to demodulate the signal is to segment the long signal into several sections. For example, the total duration of $360\mu s$ is equally segmented into 12 sections, each representing

a short AFBG with 15 notches. The spectrum of each AFBG could be calculated from Fourier transform. So the long continuous AFBG acts like a multiplexing chain with 12 individual AFBGs without gap distance in between. However, this method does take advantage of the 'continuous' property of this AFBG and the spatial resolution is limited to the length of AFBG (∼80mm). Joint-time-frequency-analysis (JTFA) is proved to be a more efficient method for demodulation. In this method, a certain time duration is chosen as the window length, for example $30\mu s$, which also represents a short AFBG with 15 notches. Then the window is slided only a fraction of its length so this new AFBG has an overlap with previous one. In this way, spatial resolution could break the limit of AFBG length. The sliding amount is chosen as $\frac{1}{3}$ of window length here. The normalized spectrum distributed along the continuous AFBG is shown in Figure 4.23. The peak frequency for all section are in vicinity of the designed number (500kHz) which proves the validity of JTFA method. But there are also noises. One the obvious frequency shift is located at $520\mu s$. From the time domain signal, there is a strong reflection at this location, which is caused by surface contact. The reflection is so strong that the interference effect between neighboring reflection are not visible. So the spectrum is close to that of the driving signal (peak frequency at 460kHz) and it is not determined by AFBG property. Future research should be focused on ensuring more uniform reflection along the AFBG.

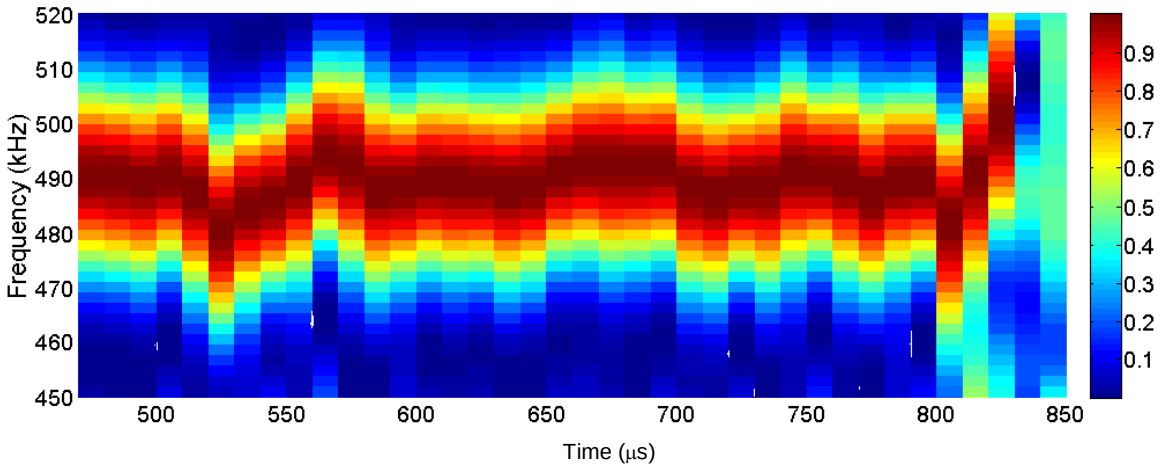


Figure 4.23: Spectrum of each sectional time signal along the long continuous AFBG.

# Chapter 5

# AFBG sensing applications

Similar to optical FBGs, AFBGs can be widely used for sensing purposes. The acoustic wave velocity on the waveguide is affected by many environmental parameters, like temperature, pressure, corrosion, strain, moving velocity of the waveguide, etc. [47, 98, 99]. Thus these environmental parameters can be accurately monitored by acoustic wave velocity. Current methods to measure acoustic wave velocity are exclusively based on measuring the time of flight $t$ (echo-pulse method) using relation $v = L/t$, where $L$ is the wave traveling distance and $v$ is the acoustic velocity. Since the time measurement system has intrinsic relative sensitivity $S_t = dt/t$, the relative sensitivity from this method is defined as

$$\frac{dv}{v} = -\frac{dt}{t} = S_t \tag{5.1}$$

Since the narrow pulse shape/intensity is easily influence by the environment, the typical relative sensitivity is about 1% [47].

With the introduction of AFBG, acoustic wave velocity can be much more accurately measured, because a frequency detection system has intrinsic relative sensitivity $S_f$ =

$df$/Bandwidth. Considering the Bragg condition $f_B = v/2\Lambda$ (Eqn. 3.7), and the main-lobe bandwidth $BW_{ML} = 2f_B/N$ (Eqn. 3.12), where $\Lambda$ is the pitch length and $N$ is the number of reflectors for an AFBG, the relative sensitivity is

$$\frac{dv}{v} = \frac{2}{N}\frac{df_B}{BW_{\mathrm{ML}}} = \frac{2}{N}S_f \tag{5.2}$$

For an AFBG with a typical value $N = 20$, its sensitivity of acoustic velocity measurement is thus one order higher than that of time-of-flight method, which makes AFBG method very promising for sensing application.

In the following sections, sensing example for temperature, pressure and corrosion are demonstrated and discussed. A discussion on distributed sensing capability of the AFBG is also included.

## 5.1 Temperature measurement

Both the elastic modulus $E$ and density $\rho$ of the waveguide material are affected by temperature. Consequently, according to the relation for longitudinal acoustic velocity in bulk material, $v = \sqrt{E/\rho}$ , the acoustic velocity is dependent on temperature [100]. The acoustic wave velocity dependence on temperature $dv/dT$ is estimated as 0.36 (m/s)/$^oC$ for silica [101]. The acoustic velocity is around 5.72km/s at room temperature, so for $1^oC$ temperature change, it causes relative velocity change $dv/v = 6.2 \times 10^{-5}$. With an acoustic wave center frequency of 500kHz, the frequency shift is around 31Hz/ °C.

Experiment has been conducted to investigate the temperature dependence of AFBG structure. A tube furnace (MTI GSL1500X) is employed to heat the AFBG fabricated on a silica fiber up to 700 °C. The reflection signal of the AFBG is recorded 100 times with a 100 °C

step and their spectrum are calculated. For every temperature measurement, a typical normalized spectrum is displayed in Figure 5.1 (a). The mean value and error bar of peak frequency locations for all spectra are shown in Figure 5.1 (b). A linear fit estimate the responsivity to be 24Hz/ °C.

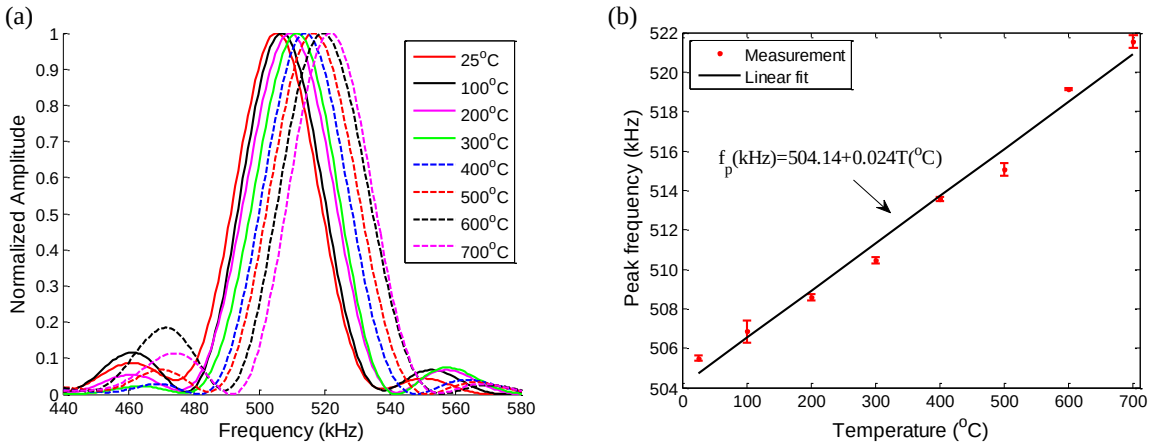


Figure 5.1: Experimental results of the temperature response of a silica AFBG at the temperatures from room temperature to 700 °C. (a) Temperature response of the AFBG reflection spectra. (b) Peak frequency shifts of AFBG spectrum with respect to temperature.

## 5.2 Pressure measurement

A solid acoustic waveguide is not much responsive to environmental pressure change, thus making it unsuitable for practical pressure measurement [102]. On the other hand, a hollow tube, especially a non-circular shaped one, changes its cross section much more easily under different pressure conditions. The cross section change of the waveguide consequently results in the variation of the guided acoustic velocity, which can be directly detected with AFBG. A waveguide with rectangular cross section is chosen as an example for simulation as illustrated in Figure 5.2. The longer side bends like a membrane under high pressure environment.

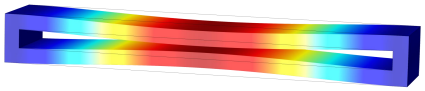

Figure 5.2: The cross section change of a rectangular waveguide under pressure.

As discussed in Section 3.1.2, FEM is employed to simulate the acoustic wave propagation on a hollow rectangular silica tube. The acoustic wave dispersion relations are calculated under different pressure conditions (1atm and 20atm), demonstrated in Figure 5.3. It is obvious that the fundamental flexural (F) modes are sensitive to pressure while the fundamental longitudinal (F) and rotational (R) modes stay the same under different pressure. The reason for different responses of different modes lies in their intrinsic behaviors. The flexural mode, which vibrates inside the cross section, is affected by the geometry and stress change of the cross section. On the other hand, the longitudinal mode is only affected by the axial stress change and should not be easily influenced by the waveguide cross section change. Therefore, the F modes are chosen for environmental pressure measurement.

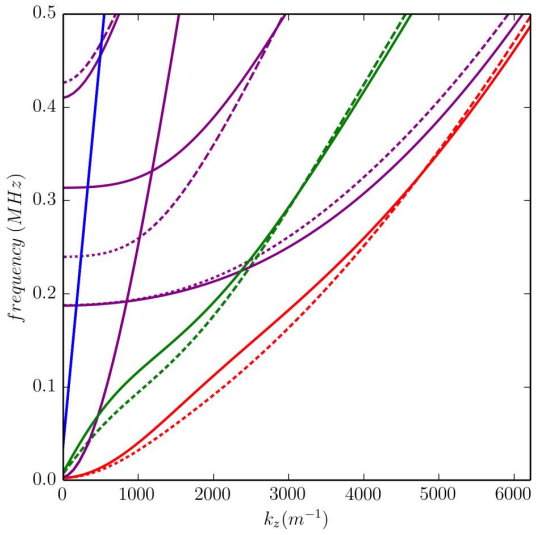


Figure 5.3: Dispersion relation under different pressure (solid line: 1atm; dash line: 20atm) for the lower-order acoustic modes. The solid and dash lines overlap for L and R modes. Fundamental F modes change under pressure.

The pressure sensing principle mentioned above is proved with experiments. A near-rectangular borosilicate glass tube, the cross section of which is shown in Figure 5.4 (a), is attached to the acoustic transducer to serve as the acoustic waveguide and is enclosed in a pressure controlling stainless steel tube. Both ends of the glass waveguide are sealed by torch so higher environment pressure deforms the geometry of waveguide cross. The acoustic wave is generated by the transducer and propagates along the rectangular glass tube until it is reflected by the tube end. Since no AFBG is inscribed on the waveguide yet, the time-of-flight is measured to investigate the acoustic velocity change.

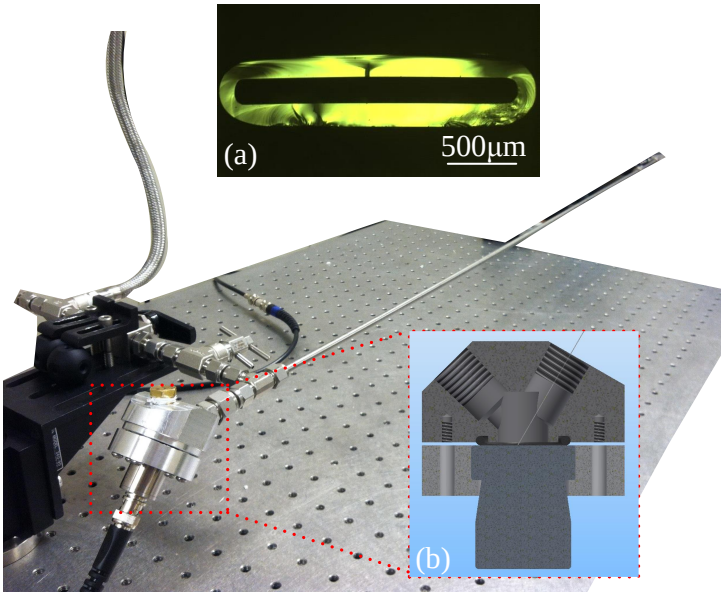


Figure 5.4: The experiment setup for acoustic velocity measurement under different pressure. Inset (a) the cross section of the borosilicate glass waveguide. Inset (b) structure of customized hermetic enclosure.

Both longitudinal and flexural modes are excited on the waveguide, shown in Figure 5.5 (a). As predicted by the simulation result, the L mode is immune to pressure change. But the F mode is sensitive to pressure. The inset picture demonstrates that there is obvious time delay between the reflected F mode signals under environment pressure 15Psi and 30Psi. This time delay is quantitatively resolved by correlation method and it is displayed in Figure 5.5 (b) for the pressure range $15 \sim 70$ psi. The responsivity is about $0.014\mu s$/psi. With the absolution time location at $1070\mu s$, the change in relative time delay is $d\tau/\tau = 1.3 \times 10^{-5}$, which is four times smaller than that for $1degc$. If an AFBG is inscribed, this would cause frequency shift about 6Hz/Psi. Also, the repeatability test of the waveguide is conducted. A three rounds test demonstrates an uncertainty of 1psi, which is the same as that of the reference pressure gauge used in the experiment. So this method is highly reliable.

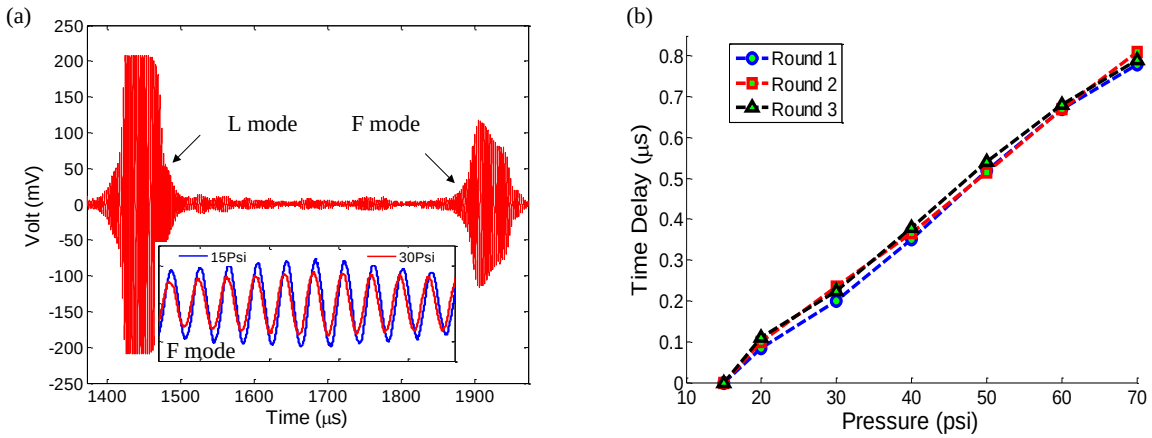


Figure 5.5: The reflection signals for L mode and for F mode in 15PSI and 30PSI environment, respectively. (b) Time delay for F mode reflection.The uncertainty is measured to be 1psi, which is the same for that of the gauge used as reference..

Taking advantage of the fact that the L mode is sensitive to temperature but not to pressure, simultaneous temperature and pressure sensing is achieved by using both L mode and F mode. The waveguide is inserted into a furnace so that its environmental temperature can be controlled along with surrounding pressure, shown in Figure 5.6 (a). Under different temperatures, the time delay of both F and L mode are recorded. Using the signal at 1atm and room temperature (25 °C) as reference, the delay in time-of-flight for F mode signal is displayed in Figure 5.6 (b). Clearly, at each temperature, the delay time is linearly related to pressure. Therefore, with the deduced temperature information through L mode signals, the pressure can be accurately extracted from F mode signals.

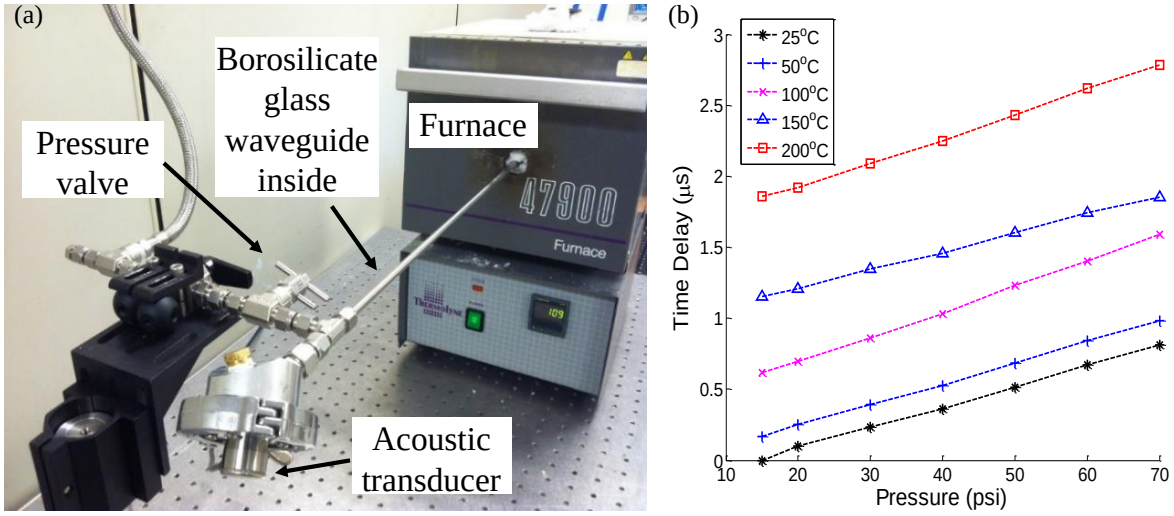


Figure 5.6: The experiment setup for simultaneous temperature and pressure measurement. (b) Time delay under different pressure and temperature for F mode signal.

The above experimental results prove the feasibility of employing the acoustic velocity change for accurate simultaneous temperature and pressure sensing. In the future, an AFBG could be inscribed on the hollow waveguide and frequency shift will provide higher sensing accuracy than time delay shown here.

## 5.3 Corrosion measurement

Corrosion measurement has been extremely important to many industrial fields, especially for structural health monitoring. In this section, the detection of corrosion with AFBG is investigated.

The diameter of the waveguide decreases during the corrosion process, which causes changes of acoustic velocity. This dependence of acoustic wave velocity on waveguide diameter is calculated based on waveguide theory as described in Section 3.1. A cylindrical waveguide

with fused silica material is used as an example for theoretical analysis. The results for both longitudinal (L) and flexural (F) mode are shown in Figure 5.7. It is observed that acoustic phase velocity for L mode almost keeps constant when the diameter of the waveguide changes in the range of $100 \sim 500\mu m$ while the acoustic phase velocity for F mode varies linearly with waveguide diameter in the same range. This theoretical analysis predicts that F mode based AFBG is very effective for corrosion sensing. Furthermore, since the L mode acoustic wave is sensitive to temperature but not to corrosion while F mode acoustic wave is sensitive to both parameters, it is possible to measure corrosion and temperature simultaneously if both modes are employed.

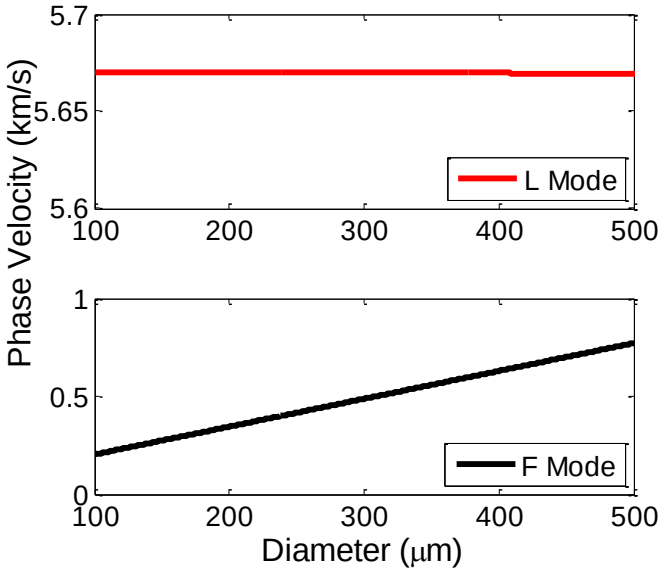


Figure 5.7: Phase velocity dependence on waveguide diameter for L mode and F mode acoustic waves.

The behavior of L mode acoustic wave based AFBG is confirmed with experiment. An AFBG structure is inscribed on a metal wire (Pelican Alloy 875, Chromium: 21%, Aluminium: 5.5%, Iron: Balance) with the mechanical compression method described in Section 4.1.3. One end

of the metal wire is polished to be flat and is glued to the surface of acoustic transducer. The AFBG is then immersed into 5% hydrochloric acid solution and the reflection signal is monitored in-line. Figure 5.8 demonstrates the experiment setup (subfigure (a)) and the demodulated peak frequency of the AFBG reflection spectrum (subfigure (b)) during the etching process. It is shown that the diameter of the metal wire decreases from $520\mu m$ to $455\mu m$ while the peak frequency location of AFBG reflection spectrum almost stays constant during the corrosion process. The experimental results is consistent with theoretical prediction. F mode acoustic wave based AFBG is to be investigated in the future.

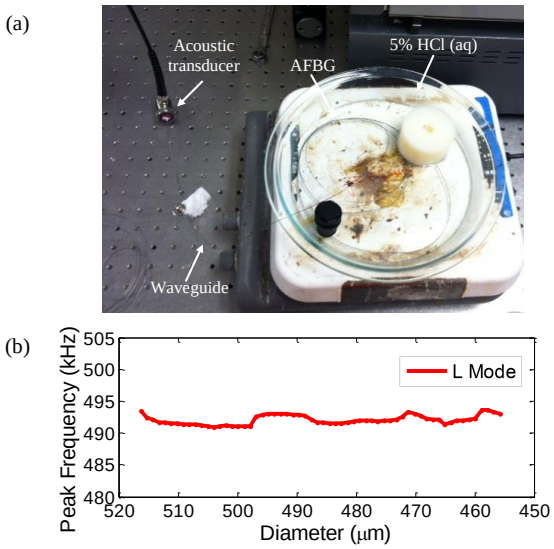


Figure 5.8: (a) The experiment setup for corrosion measurement. (b) The peak frequency location of the reflection spectrum of the AFBG stays almost constant when the diameter of waveguide decreases because of corrosion.

## 5.4 Distributed temperature measurement

A discussion on long continuous AFBG sample and its spectrum has been presented in Section 4.3.4. Here, it is demonstrated for distributed sensing applications. An AFBG

sample with 110 pitches and 5.5mm pitch length on a metal wire (Pelican Alloy 785) is fabricated. The length of the grating section is thus ∼600mm. The sample is inserted into a furnace together with a ceramic tube, which is used to hold the metal wire in place. The furnace provides a heated section of about 180mm in length and the rest of the long AFBG is kept close to room temperature as shown in Figure 5.9 (a).

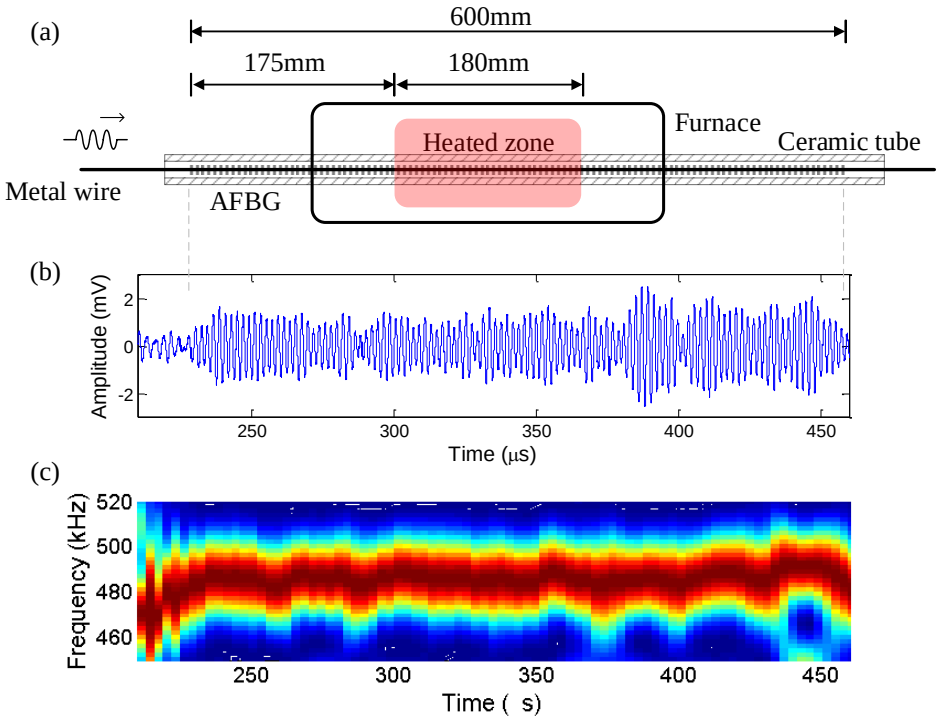


Figure 5.9: (a) Setup for distributed sensing with continuous AFBG. (b) Reflection signal from AFBG in time domain. (c) Spectrum distribution for each small section of AFBG.

The reflection signal from the AFBG is obtained through the 3-pulse fast interrogation method and is shown in Figure 5.9 (b). JTFA method with window size $30\mu s$ and overlap 90% is used to demodulate the spectrum distribution at each location. The result is shown in Figure 5.9 (c). Similar to the result in Section 4.3.4, there are some fluctuations for the peak frequency location for different sections of the long continuous AFBG. Further investigation is required to enhance SNR and reduce this fluctuation.

The furnace is turned on to heat one section of the long AFB from room temperature to 500 °C and the reflection signal is recorded at every 100 °C. By analyzing the spectrum distribution along the AFBG at each temperature, the peak frequency shift is calculated using the one at room temperature as reference. The result is shown in Figure 5.10. Clearly, the heated zone leads to much larger peak frequency shift compared to other sections and the frequency shift quantity is directly related to temperature. It is also noticeable that there is a false signal section. This is caused by some systematic electrical noise and can be removed with improvement of electronic components.

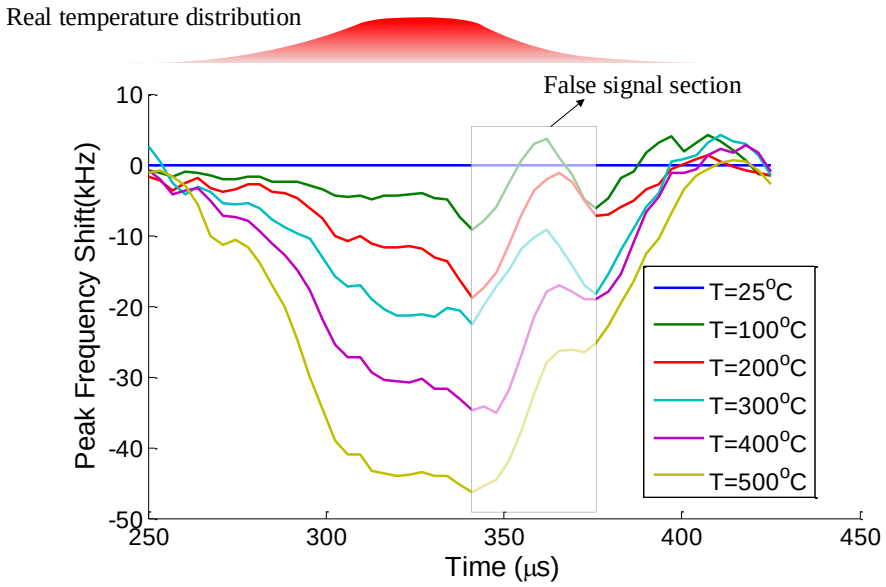


Figure 5.10: Distributed temperature sensing with a long continuous AFBG.

# Chapter 6

# Conclusion and future work

## 6.1 Conclusion

The fiber Bragg grating concept has been successfully transferred from optical field to acoustic field. Periodic structures on an acoustic waveguide generate multiple reflections that interfere with each other and result a narrow peak at the resonance or Bragg frequency in the acoustic wave reflection spectrum. This acoustic fiber Bragg grating concept is validated and demonstrated for various parameter measurements.

Acoustic waveguides with both solid cylindrical and hollow square cross section are thoroughly analyzed. Cylindrical waveguides like optical fibers and metal wires support three fundamental modes below a cut-off frequency, which is inversely proportional to waveguide diameter. For a square hollow waveguide, like a square tube, four fundamental modes are supported. With an appropriate excitation method, any fundamental mode can be selectively excited. Single mode operation leads to high SNR for a single parameter sensing while multimode operation may offer simultaneous multi-parameter sensing.

AFBG samples on optical fibers and metal wires have been demonstrated. AFBG on an optical fiber was fabricated with a femtosecond laser micromachining setup with accuracy of $1\mu m$. Periodic circumferential trenches were machined with excellent uniformity. The measured peak frequency location is at 505.9 kHz, only $\sim 1\%$ away from theoretical value calculated by a transfer matrix method. AFBG on a metal wire was fabricated with mechanical compression method, and the measured peak frequency location is 498.9 kHz, which is 1.1 kHz away from theoretical prediction by multi-reflection method. Even though the AFBG on a metal wire is slightly less accurate than that on an optical fiber, its fabrication was 100 times faster. So a much longer AFBG ($\sim$ 1.2 m) was obtained on metal wire and the length was only limited by the translation stage used in fabrication.

AFBGs are demonstrated to be effective for sensing multiple parameters. A fast interrogation method based on Fourier transform was utilized to demodulate the reflection spectrum from an AFBG. Compared to traditional frequency scanning method, this technique reduced the system response time from 3 min. to 1 ms. The location of the peak frequency in an AFBG reflection spectrum was shown to be linearly varying with temperature in the range 25 °C to 700 °C. The upper limit of this measurable temperature range was determined by the material used for fabricating AFBG. By switching to other waveguides like a sapphire fiber, a much higher temperature can be achieved. The measurement from corrosion monitoring also showed the relation between etched extent of waveguide and AFBG peak reflection frequency location. Pressure variations from 15 psi to 75 psi in the AFBG surrounding environment also introduces linear acoustic velocity change for a square tube waveguide. In this case, the sensing resolution and repeatability was estimated to be <1 psi. With the employment of both the fundamental longitudinal mode and one fundamental flexural mode, simultaneous measurement of temperature and pressure was also realized. A 0.6 m long AFBG was used to demonstrate distributed sensing ability through measurement of

surrounding temperature. The variance of temperture as well as its location can be directly demodulated through the reflection signal spectrum from each reflector in the AFBG.

## 6.2 Future work

Even though AFBG has been demonstrated to be an effective method for acoustic velocity measurement, a few improvements need to be made before applying this technology to industrial environment.

Firstly, the low coupling efficiency between the acoustic transducer and the acoustic waveguide requires improvement. The commercial acoustic transducer usually has an active region of $0.5\sim1''$ in diameter as they are designed for bulk wave detection. However, the waveguide in our application has a diameter less than 1 mm. This ten times reduction in diameter causes more than 99% of the energy generated by the transducer not being captured by the waveguide. Miniature PZT deposited on the tip of the waveguide can effectively solve this dimension mismatch problem and hence deserves significant investigation.

Secondly, the current waveguide geometry does not confine the acoustic energy in the center part of the waveguide. Consequently, the signal is sensitive to surface contacts. Experiment with long lead-in fiber indicates that majority of waveguide attenuation comes from surface contact. By adding another layer of material with appropriate acoustic impedance to the current waveguide should make the structure immune to unwanted environmental disturbances.

Finally, even though the low frequency acoustic waves show lower attenuation in the waveguide and also reduce the overall cost, they also limit the spatial resolution that can be achieved by this sensing principle. In the current design, acoustic waves of frequency less

than 1 MHz correspond to a spatial resolution of a few centimeters on most solid waveguide. Since the spatial resolution improves linearly with the frequency and the attenuation increases linearly with the square of frequency, it would be beneficial to optimize the frequency for different sensing applications.

# Appendix A

# AFBG transfer matrix model approximation

Considering dimension relations $l/L = m$, $l + L = \Lambda$, $1 + \delta = \frac{k\Lambda}{\pi}$ and constrains $|\delta| < 0.1$ and $m < 0.01$, the trigonometric expressions are transformed with approximations

$$\begin{cases} \cos kl = \cos \frac{m(1+\delta)}{1+m}\pi \approx \cos m(1+\delta)\pi \approx 1 \\ \cos kL = \cos\left[1 + \frac{\delta - m}{1+m}\right]\pi \approx -\cos(\delta - m)\pi \\ \sin kl \approx \sin m(1+\delta)\pi \approx m\pi(1+\delta) \\ \sin kL \approx -\sin(\delta - m)\pi \approx -\sin \delta\pi \end{cases} \tag{A.1}$$

It is important to notice that the $\alpha_2\alpha_3 \approx 0$, which significantly simplifies the expression for $\lambda_{1,2}$.

$$\begin{cases} \lambda_1 = \alpha_1 \\ \lambda_2 = \alpha_4 \end{cases} \tag{A.2}$$

From Eqn.(3.20) and Eqn.(A.2), both $M_{21}$ and $M_{22}$ can be obtained

$$\begin{cases} M_{21} = \frac{\alpha_4^N - \alpha_1^N}{\alpha_4 - \alpha_1}\alpha_3 \\ M_{22} = \alpha_4^N \end{cases} \tag{A.3}$$

Therefore, the reflection coefficient Eqn.3.17 is simplified to

$$R = -\frac{\alpha_3}{\alpha_4 - \alpha_1}\left[1 - \left(\frac{\alpha_1}{\alpha_4}\right)^N\right] \tag{A.4}$$

The phase term of $\alpha_1$ is critical for the second term of $R$ since $\alpha_4 = \alpha_1^*$

$$\theta(\alpha_1) = kL + \arctan\left(\frac{1/\gamma + \gamma}{2}\tan kl\right) \tag{A.5}$$

With the constrains $kl = m(1+\delta)\pi \ll \pi$ and $\frac{1/\gamma+\gamma}{2} \approx 1$, we have $\frac{1/\gamma+\gamma}{2}\tan kl \approx \tan\frac{1/\gamma+\gamma}{2}kl$. So,

$$\theta(\alpha_1) \approx kL + \frac{1/\gamma+\gamma}{2}kl \approx \pi\left[1 + \delta - m + \frac{1/\gamma+\gamma}{2}m(1+\delta)\right] \tag{A.6}$$

Furthermore,

$$\begin{aligned} 1 - \left(\tfrac{\alpha_1}{\alpha_4}\right)^N &= 1 - e^{i2N\theta(\alpha_1)} \\ &= 2\sin(N\theta(\alpha_1))e^{i[N\theta(\alpha_1)-\pi/2]} \end{aligned} \tag{A.7}$$

The first term of $R$ can also be obtained as

$$\frac{\alpha_3}{\alpha_4 - \alpha_1} \approx \frac{\frac{1/\gamma-\gamma}{2}m\pi(1+\delta)}{2\sin\delta\pi + (1/\gamma+\gamma)\,m\pi(1+\delta)\cos(\delta - m)\,\pi} \tag{A.8}$$

Finally, we obtained the approximated result of reflection coefficient

$$R \approx m\pi(1+\delta)\frac{1/\gamma-\gamma}{2}\frac{\sin N\delta\pi}{\sin\delta\pi}e^{i\left\{\pi N\left[\left(\frac{1/\gamma+\gamma}{2}m+1\right)(1+\delta)-m\right]+\pi\left(\frac{1}{2}+N\right)\right\}} \tag{A.9}$$

# Bibliography


[1] F Lexer, Christoph K Hitzenberger, AF Fercher, and M Kulhavy. Wavelength-tuning interferometry of intraocular distances. *Applied Optics*, 36(25):6548–6553, 1997.

[2] Kazuo Hotate. Brillouin scattering accompanied by acoustic grating in an optical fiber and applications in fiber distributed sensing. In *21st International Conference on Optical Fibre Sensors (OFS21)*, pages 775307–775307. International Society for Optics and Photonics, 2011.

[3] Stephen J Mihailov. Fiber bragg grating sensors for harsh environments. *Sensors*, 12(2):1898–1918, 2012.

[4] William Henry Bragg and William Lawrence Bragg. The reflection of x-rays by crystals. *Proceedings of the Royal Society of London. Series A, Containing Papers of a Mathematical and Physical Character*, 88(605):428–438, 1913.

[5] Nico F Declercq and Cindy SA Dekeyser. Acoustic diffraction effects at the hellenistic amphitheater of epidaurus: Seat rows responsible for the marvelous acoustics. *The Journal of the Acoustical Society of America*, 121(4):2011–2022, 2007.

[6] D Nicholas and CR Hill. Acoustic bragg diffraction from human tissues. *Nature*, 257(5524):305–306, 1975.

[7] CH Hodges and J Woodhouse. Vibration isolation from irregularity in a nearly periodic structure: theory and measurements. *The Journal of the Acoustical Society of America*, 74(3):894–905, 1983.

[8] Ken-ya Hashimoto and Ken-Ya Hashimoto. *Surface acoustic wave devices in telecommunications*. Springer, 2000.

[9] John F Heanue, Matthew C Bashaw, and Lambertus Hesselink. Volume holographic storage and retrieval of digital data. *SCIENCE-NEW YORK THEN WASHINGTON-*, pages 749–749, 1994.

[10] Igor M Koba. High-resolution spatial light modulator for 3-dimensional holographic display, November 16 2004. US Patent 6,819,469.

[11] Peter Bernhard Hirsch. *Electron microscopy of thin crystals*. Plenum Press, 1967.

[12] HM Rietveld. Line profiles of neutron powder-diffraction peaks for structure refinement. *Acta Crystallographica*, 22(1):151–152, 1967.

[13] Kenneth O Hill and Gerald Meltz. Fiber bragg grating technology fundamentals and overview. *Journal of lightwave technology*, 15(8):1263–1276, 1997.

[14] Y Liu, E Tangdiongga, Z Li, Shaoxian Zhang, Huug de Waardt, GD Khoe, and HJS Dorren. Error-free all-optical wavelength conversion at 160 gb/s using a semiconductor optical amplifier and an optical bandpass filter. *Journal of Lightwave Technology*, 24(1):230, 2006.

[15] Christine Spiegelberg, Jihong Geng, Yongdan Hu, Yushi Kaneda, Shibin Jiang, and N Peyghambarian. Low-noise narrow-linewidth fiber laser at 1550 nm (june 2003). *Journal of Lightwave Technology*, 22(1):57–62, 2004.

[16] Mousumi Majumder, Tarun Kumar Gangopadhyay, Ashim Kumar Chakraborty, Kamal Dasgupta, and Dipak Kumar Bhattacharya. Fibre bragg gratings in structural health monitoringpresent status and applications. *Sensors and Actuators A: Physical*, 147(1):150–164, 2008.

[17] W Jin, Y Zhou, PKC Chan, and HG Xu. A fibre-optic grating sensor for the study of flow-induced vibrations. *Sensors and Actuators A: Physical*, 79(1):36–45, 2000.

[18] G Gagliardi, M Salza, P Ferraro, P De Natale, A Di Maio, S Carlino, G De Natale, and E Boschi. Design and test of a laser-based optical-fiber bragg-grating accelerometer for seismic applications. *Measurement Science and Technology*, 19(8):085306, 2008.

[19] Turan Erdogan. Fiber grating spectra. *Lightwave Technology, Journal of*, 15(8):1277–1294, 1997.

[20] KO Hill, B Malo, F Bilodeau, DC Johnson, and J Albert. Bragg gratings fabricated in monomode photosensitive optical fiber by uv exposure through a phase mask. *Applied Physics Letters*, 62(10):1035–1037, 1993.

[21] G Meltz, W W Morey, and WH Glenn. Formation of bragg gratings in optical fibers by a transverse holographic method. *Optics letters*, 14(15):823–825, 1989.

[22] PE Dyer, RJ Farley, and R Giedl. Analysis and application of a 01 order talbot interferometer for 193 nm laser grating formation. *Optics Communications*, 129(1-2):98–108, 1996.

[23] B Malo, KO Hill, F Bilodeau, DC Johnson, and J Albert. Point-by-point fabrication of micro-bragg gratings in photosensitive fibre using single excimer pulse refractive index modification techniques. *Electronics Letters*, 29(18):1668–1669, 1993.

[24] Ams Martinez, Mykhaylo Dubov, Igor Khrushchev, and Ian Bennion. Direct writing of fibre bragg gratings by femtosecond laser. *Electronics Letters*, 40(19):1170–1172, 2004.

[25] Michael Fokine. Formation of thermally stable chemical composition gratings in optical fibers. *JOSA B*, 19(8):1759–1765, 2002.

[26] Amós Martinez, IY Khrushchev, and Ian Bennion. Thermal properties of fibre bragg gratings inscribed point-by-point by infrared femtosecond laser. *Electronics letters*, 41(4):176–178, 2005.

[27] Alan D Kersey, TA Berkoff, and WW Morey. Multiplexed fiber bragg grating strain-sensor system with a fiber fabryperot wavelength filter. *Optics letters*, 18(16):1370–1372, 1993.

[28] Yunmiao Wang, Jianmin Gong, Bo Dong, Dorothy Y Wang, Tyler J Shillig, and Anbo Wang. A large serial time-division multiplexed fiber bragg grating sensor network. *Journal of Lightwave Technology*, 30(17):2751–2756, 2012.

[29] Philip J Henderson, David J Webb, David A Jackson, LS Zhang, and Ian Bennion. Highly-multiplexed grating-sensors for temperature-referenced quasi-static measurements of strain in concrete bridges. Spie-Int Soc Optical Engineering, 1999.

[30] KP Koo, AB Tveten, and ST Vohra. Dense wavelength division multiplexing of fibre bragg grating sensors using cdma. *Electronics Letters*, 35(2):165–167, 1999.

[31] Alan D Kersey, Michael A Davis, Heather J Patrick, Michel LeBlanc, KP Koo, CG Askins, MA Putnam, and E Joseph Friebele. Fiber grating sensors. *Journal of lightwave technology*, 15(8):1442–1463, 1997.

[32] Tsutomu Yamate and Oliver C Mullins. Permanent optical sensor downhole fluid analysis systems, August 20 2002. US Patent 6,437,326.

[33] Reinhardt Willsch, Wolfgang Ecke, and Hartmut Bartelt. Optical fiber grating sensor networks and their application in electric power facilities, aerospace and geotechnical engineering. In *Optical Fiber Sensors Conference Technical Digest, 2002. Ofs 2002, 15th*, pages 49–54. IEEE.

[34] Juan C Juarez, Eric W Maier, Kyoo Nam Choi, and Henry F Taylor. Distributed fiber-optic intrusion sensor system. *Journal of lightwave technology*, 23(6):2081–2087, 2005.

[35] Alberto Fernandez Fernandez, Andrei I Gusarov, Serge Bodart, Koen Lammens, Francis Berghmans, Marc Decre, Patrice Me, Michel Blondel, and Alain Delchambre. Temperature monitoring of nuclear reactor cores with multiplexed fiber bragg grating sensors. *Optical Engineering*, 41(6):1246–1254, 2002.

[36] JS Leng, RA Barnes, A Hameed, D Winter, J Tetlow, GC Mays, and GF Fernando. Structural nde of concrete structures using protected efpi and fbg sensors. *Sensors and Actuators A: Physical*, 126(2):340–347, 2006.

[37] Bertram Alexander Auld. *Acoustic fields and waves in solids.* , 1973.

[38] Bill Drafts. Acoustic wave technology sensors. *IEEE Transactions on Microwave Theory and Techniques*, 49(4):795–802, 2001.

[39] O Ikata, T Miyashita, T Matsuda, T Nishihara, and Y Satoh. Development of low-loss band-pass filters using saw resonators for portable telephones. In *Ultrasonics Symposium, 1992. Proceedings., IEEE 1992*, pages 111–115. IEEE, 1992.

[40] Kerstin Länge, Bastian E Rapp, and Michael Rapp. Surface acoustic wave biosensors: a review. *Analytical and bioanalytical chemistry*, 391(5):1509–1519, 2008.

[41] Thomas M Reeder and Donald E Cullen. Surface-acoustic-wave pressure and temperature sensors. *Proceedings of the IEEE*, 64(5):754–756, 1976.

[42] G Scholl, F Schmidt, T Ostertag, L Reindl, H Scherr, and U Wolff. Wireless passive saw sensor systems for industrial and domestic applications. In *Frequency Control Symposium, 1998. Proceedings of the 1998 IEEE International*, pages 595–601. IEEE, 1998.

[43] Alfred Pohl, G Ostermayer, L Reindl, and F Seifert. Monitoring the tire pressure at cars using passive saw sensors. In *Ultrasonics Symposium, 1997. Proceedings., 1997 IEEE*, volume 1, pages 471–474. IEEE, 1997.

[44] MG Schweyer, JA Hilton, JE Munson, JC Andle, JM Hammond, and RM Lec. A novel monolithic piezoelectric sensor. In *Frequency Control Symposium, 1997., Proceedings of the 1997 IEEE International*, pages 32–40. IEEE, 1997.

[45] Jeanne Hossenlopp, Lizhong Jiang, Richard Cernosek, and Fabien Josse. Characterization of epoxy resin (su-8) film using thickness-shear mode (tsm) resonator under various conditions. *Journal of Polymer Science Part B: Polymer Physics*, 42(12):2373–2384, 2004.

[46] MG Schweyer, JC Andle, DJ McAllister, LA French, and JF Vetelino. An acoustic plate mode sensor for aqueous mercury. In *Ultrasonics Symposium, 1996. Proceedings., 1996 IEEE*, volume 1, pages 355–358. IEEE, 1996.

[47] N Gopalsami and AC Raptis. Acoustic velocity and attenuation measurements in

thin rods with application to temperature profiling in coal gasification systems. *IEEE transactions on sonics and ultrasonics*, 31(1):32–39, 1984.

[48] Ward Johnson and GA Alers. Force measurement using vibrational spectroscopy. *Review of scientific instruments*, 68(1):102–108, 1997.

[49] CK Jen, JEB Oliveira, JCH Yu, JD Dai, and JF Bussiere. Analysis of thin rod flexural acoustic wave gravimetric sensors. *Applied physics letters*, 56(22):2183–2185, 1990.

[50] Paul CH Li and Michael Thompson. Mass sensitivity of the thin-rod acoustic wave sensor operated in flexural and extensional modes. *Analytical chemistry*, 68(15):2590–2597, 1996.

[51] Chester L Shepard, Brion J Burghard, Mark Friesel, B Percy Hildebrand, Xang Moua, Aaron Diaz, Carl W Enderlin, et al. Measurements of density and viscosity of one-and two-phase fluids with torsional waveguides. *Ultrasonics, Ferroelectrics, and Frequency Control, IEEE Transactions on*, 46(3):536–548, 1999.

[52] Parthasarathy Shakkottai and Shakkottai P Venkateshan. System for temperature profile measurement in large furnances and kilns and method therefor, August 9 1988. US Patent 4,762,425.

[53] Xiaoyi Bao and Liang Chen. Recent progress in distributed fiber optic sensors. *Sensors*, 12(7):8601–8639, 2012.

[54] M_K Barnoski, M_D Rourke, SM Jensen, and RT Melville. Optical time domain reflectometer. *Applied optics*, 16(9):2375–2379, 1977.

[55] Gordon Oscroft. Intrinsic fibre optic sensors. In *Fibre Optics' 87*, pages 207–213. International Society for Optics and Photonics, 1987.

[56] Juan C Juarez, Eric W Maier, Kyoo Nam Choi, and Henry F Taylor. Distributed fiber-optic intrusion sensor system. *Journal of lightwave technology*, 23(6):2081, 2005.

[57] RI MacDonald. Frequency domain optical reflectometer. *Applied Optics*, 20(10):1840–1844, 1981.

[58] Wf Eickhoff and Rf Ulrich. Optical frequency domain reflectometry in single-mode fiber. *Applied Physics Letters*, 39(9):693–695, 1981.

[59] Stephen T Kreger, Dawn K Gifford, Mark E Froggatt, Alex K Sang, Roger G Duncan, Matthew S Wolfe, and Brian J Soller. High-resolution extended distance distributed fiber-optic sensing using rayleigh backscatter. In *The 14th International Symposium on: Smart Structures and Materials & Nondestructive Evaluation and Health Monitoring*, pages 65301R–65301R. International Society for Optics and Photonics, 2007.

[60] JP Dakin, DJ Pratt, GW Bibby, and JN Ross. Distributed optical fibre raman temperature sensor using a semiconductor light source and detector. *Electronics Letters*, 21(13):569–570, 1985.

[61] AH Hartog, AP Leach, and MP Gold. Distributed temperature sensing in solid-core fibres. *Electronics letters*, 21(23):1061–1062, 1985.

[62] George A Brown, Arthur Hartog, et al. Optical fiber sensors in upstream oil & gas. *Journal of petroleum technology*, 54(11):63–65, 2002.

[63] Alan Rogers. Distributed optical-fibre sensing. *Measurement Science and Technology*, 10(8):R75–R99, 1999.

[64] Michael G Tanner, Shellee D Dyer, Burm Baek, Robert H Hadfield, and Sae Woo Nam. High-resolution single-mode fiber-optic distributed raman sensor for absolute

temperature measurement using superconducting nanowire single-photon detectorsa). *Applied Physics Letters*, 99(20):201110, 2011.

[65] A FERNANDEZ FEMANDEZ, P Rodeghiero, B Brichard, F Berghmans, AH Hartog, P Hughes, K Williams, and AP Leach. Radiation-tolerant raman distributed temperature monitoring system for large nuclear infrastructures. *IEEE transactions on nuclear science*, 52(6):2689–2694, 2005.

[66] Kwang Suh and Chung Lee. Auto-correction method for differential attenuation in a fiber-optic distributed-temperature sensor. *Optics letters*, 33(16):1845–1847, 2008.

[67] Dusun Hwang, Dong-Jin Yoon, Il-Bum Kwon, Dae-Cheol Seo, and Youngjoo Chung. Novel auto-correction method in a fiber-optic distributed-temperature sensor using reflected anti-stokes raman scattering. *Optics express*, 18(10):9747–9754, 2010.

[68] Kaoru Shimizu, Tsuneo Horiguchi, Yahei Koyamada, and Toshio Kurashima. Coherent self-heterodyne detection of spontaneously brillouin-scattered light waves in a single-mode fiber. *Optics letters*, 18(3):185–187, 1993.

[69] Toshio Kurashima, Tsuneo Horiguchi, and Mitsuhiro Tateda. Distributed-temperature sensing using stimulated brillouin scattering in optical silica fibers. *Optics Letters*, 15(18):1038–1040, 1990.

[70] Xiaoyi Bao, David J Webb, and David A Jackson. 22-km distributed temperature sensor using brillouin gain in an optical fiber. *Optics letters*, 18(7):552–554, 1993.

[71] Dieter Garus, Torsten Gogolla, Katerina Krebber, and Frank Schliep. Brillouin optical-fiber frequency-domain analysis for distributed temperature and strain measurements. *Journal of lightwave technology*, 15(4):654–662, 1997.

[72] Romeo Bernini, Aldo Minardo, and Luigi Zeni. Distributed sensing at centimeter-scale spatial resolution by bofda: measurements and signal processing. *Photonics Journal, IEEE*, 4(1):48–56, 2012.

[73] Yongkang Dong, Liang Chen, and Xiaoyi Bao. Extending the sensing range of brillouin optical time-domain analysis combining frequency-division multiplexing and in-line edfas. *Journal of Lightwave Technology*, 30(8):1161–1167, 2012.

[74] Hao Zhang, Wei Pang, Hongyu Yu, and Eun Sok Kim. High-tone bulk acoustic resonators on sapphire, crystal quartz, fused silica, and silicon substrates. *Journal of applied physics*, 99(12):124911, 2006.

[75] Bertram Alexander Auld. *Acoustic fields and waves in solids*. Robert E. Krieger Publishing Company, 1990.

[76] Dennison Bancroft. The velocity of longitudinal waves in cylindrical bars. *Physical Review*, 59(7):588, 1941.

[77] George Elbert Hudson. Dispersion of elastic waves in solid circular cylinders. *Physical Review*, 63(1-2):46, 1943.

[78] H Norman Abramson. Flexural waves in elastic beams of circular cross section. *The Journal of the Acoustical Society of America*, 29(1):42–46, 1957.

[79] Bertram Alexander Auld. *Acoustic fields and waves in solids*. , 1973.

[80] Bertram Alexander Auld. *Acoustic fields and waves in solids*, volume 2. RE Krieger, 1990.

[81] Morio Onoe, HD McNiven, and RD Mindlin. Dispersion of axially symmetric waves in elastic rods. *Journal of Applied Mechanics*, 29(4):729–734, 1962.

[82] P Andreatch Jr and HJ McSkimin. Pressure dependence of ultrasonic wave velocities and elastic stiffness moduli for a tio2sio2 glass (corning 7971). *Journal of Applied Physics*, 47(4):1299–1301, 1976.

[83] DB Fraser, JT Krause, and AH Meitzler. Physical limitations on the performance of vitreous silica in highfrequency ultrasonic and acoustooptical devices. *Applied Physics Letters*, 11(10):308–310, 1967.

[84] Lonny L Thompson. A review of finite-element methods for time-harmonic acoustics. *J. Acoust. Soc. Am*, 119(3):1315–1330, 2006.

[85] Dan Grobnic, Stephen J Mihailov, Christopher W Smelser, and Huimin Ding. Sapphire fiber bragg grating sensor made using femtosecond laser radiation for ultrahigh temperature applications. *Photonics Technology Letters, IEEE*, 16(11):2505–2507, 2004.

[86] A Morales, J Flores, L Gutirrez, and RA Mndez-Snchez. Compressional and torsional wave amplitudes in rods with periodic structures. *The Journal of the Acoustical Society of America*, 112(5):1961–1967, 2002.

[87] A Daz-de Anda, A Pimentel, J Flores, A Morales, L Gutirrez, and RA Mndez-Snchez. Locally periodic timoshenko rod: Experiment and theory. *The Journal of the Acoustical Society of America*, 117(5):2814–2819, 2005.

[88] YQ Guo and DN Fang. Analysis and interpretation of longitudinal waves in periodic multiphase rods using the method of reverberation-ray matrix combined with the floquet-bloch theorem. *Journal of Vibration and Acoustics*, 136(1):011006, 2014.

[89] A Morales, J Flores, L Gutirrez, and RA Mndez-Snchez. Compressional and torsional wave amplitudes in rods with periodic structures. *The Journal of the Acoustical Society of America*, 112(5):1961–1967, 2002.

[90] B Ravindra. Love-theoretical analysis of periodic system of rods. *The Journal of the Acoustical Society of America*, 106(2):1183–1186, 1999.

[91] Dong Li and Haym Benaroya. Waves, normal modes and frequencies in periodic and near-periodic rods. part ii. *Wave Motion*, 20(4):339–358, 1994.

[92] David J Griffiths and Carl A Steinke. Waves in locally periodic media. *American Journal of Physics*, 69(2):137–154, 2001.

[93] Loren Cerami, Eric Mazur, Stefan Nolte, and Chris B Schaffer. *Femtosecond laser micromachining*, pages 287–321. Springer, 2013.

[94] Tyson N Kim, Kyle Campbell, Alex Groisman, David Kleinfeld, and Chris B Schaffer. Femtosecond laser-drilled capillary integrated into a microfluidic device. *Applied Physics Letters*, 86(20):201106, 2005.

[95] Jaegu Kim and Suckjoo Na. Metal thin film ablation with femtosecond pulsed laser. *Optics And Laser Technology*, 39(7):1443–1448, 2007.

[96] BN Chichkov, C Momma, S Nolte, F Von Alvensleben, and A Tnnermann. Femtosecond, picosecond and nanosecond laser ablation of solids. *Applied Physics A*, 63(2):109–115, 1996.

[97] D von der Linde and H Schler. Breakdown threshold and plasma formation in femtosecond lasersolid interaction. *JOSA B*, 13(1):216–222, 1996.

[98] Donald E Cullen. Surface acoustic wave (saw) pressure sensor structure, 1984.

[99] Benjamin L Ervin and Henrique Reis. Longitudinal guided waves for monitoring corrosion in reinforced mortar. *Measurement Science and Technology*, 19(5):055702, 2008.

[100] AEH Love. *The mathematical theory of elasticity*. Cambridge University Press, 1927.

[101] John M Ide. The velocity of sound in rocks and glasses as a function of temperature. *The Journal of Geology*, pages 689–716, 1937.

[102] Francis Birch and RUSSELL R LAW. Measurement of compressibility at high pressures and high temperatures. *Geological Society of America Bulletin*, 46(8):1219–1250, 1935.